Particle Size Dependence on the Luminescence Spectra of Eu^{3+}:Y_2O_3 and Eu^{3+}:CaO

Diane Keith Williams

Dissertation submitted to the Faculty of the
Virginia Polytechnic Institute and State University in
partial fulfillment of the requirements for the degree of

Doctor of Philosophy
in
Chemistry

Brian Tissue, Chair
Mark Anderson
Karen Brewer
John Dillard
Gary Long

Defended on
November 11, 2002

Blacksburg, Virginia

Keywords: Nanocrystals, Laser Spectroscopy, Dopant Distribution, Eu^{3+}:Y_2O_3, Eu^{3+}:CaO

Particle Size Dependence on the Luminescence Spectra of Eu^{3+}:Y_2O_3 and Eu^{3+}:CaO

Diane Keith Williams

(Abstract)

Since the Eu^{3+} ion can occupy different cation sites in a host material, it can serve as a useful probe of nanocrystalline structures to gain more insight into the structural changes that can occur when the particle size is reduced from the bulk to nanometer regime. The use of laser spectroscopy to probe two nanocrystalline structures, Eu^{3+}:Y_2O_3 and Eu^{3+}:CaO, was investigated. The nanocrystalline structures were prepared by the laser-vaporization-gas-phase condensation of the bulk oxides. The particle size distribution and dominant particle diameters of the nanocrystals were determined by transmission electron microscopy.

The particle size dependency results of Eu^{3+}:Y_2O_3 revealed three distinct phases: (1) the sharp lines of the monoclinic Y_2O_3 were dominant in the larger particles; (2) the C_2 site of the cubic phase, which appears in the smaller particles; and (3) the amorphous phase that increases in intensity as the particle size decreases. The observation of distinct spectral lines from the monoclinic phase confirms the presence of a crystalline phase for all of particle sizes studied.

The site-selective results of various concentrations of 13-nm Eu^{3+}:CaO showed that the laser-vaporization-gas-phase condensation method of preparation produced two europium-containing phases at most concentrations: cubic CaO and monoclinic Eu_2O_3. Results showed that the monoclinic Eu_2O_3 phase could be reduced by 95% by annealing at 800 ^{0}C for 30 minutes without particle growth.

Since the Eu^{3+} ion and the Y^{3+} ion are isovalent, the substitution of a Eu^{3+} ion into Y_2O_3 is considered a trivial case of extrinsic disorder since the impurity is neutral relative to a perfect crystal[1]. As a result, it is not necessary to have any other defects present in the crystals to maintain charge neutrality. With Eu^{3+}:CaO, the dopant and host cation charges are different and therefore the dopant distribution can be investigated by site-selective spectroscopy.

Since the experimental dopant distribution results for nanocrystalline Eu^{3+}:CaO were inconclusive, a model to predict the theoretical change in the dopant distribution in Eu^{3+}:CaO as a function of particle size was developed. The model predicts that the defect chemistry is affected when the particle size is approximately 50 nm and smaller.

References

(1) Smyth, D. M. *The Defect Chemistry of Metal Oxides*; Oxford University Press: New York, 2000.

Acknowledgements

I wish to express my love and appreciation to my family for their love, unwavering support and patience. I thank my father, Jack Keith, for being my earliest science teacher, and my mother, Margaret Jones Keith, for teaching me to appreciate literature and music. I am grateful to my husband, Brian Clay Williams, for his tremendous moral support. Thank you to my sons, Ryan, Cole, and Keith Williams, for tolerating my absence and distraction while I have been a student. Having all of you in my life is my greatest achievement.

Professionally, many people have contributed to my graduate education and I offer my sincere gratitude to each one for their unique contribution: Professors Mark Anderson, Sandy Boatman, Karen Brewer, Ray Dessy, Daniel Derringer, John Dillard, Bansi Kalra, Gary Long, Harold McNair, Larry Taylor, Brian Tissue, Ketan Trivedi, Jimmy Viers, and J. P. Wightman.

List of Figures

List of Tables

Notes on Abbreviations, Units and Notations

Abbreviations:

DNC: Doped Nanocrystals
ICP-AES: Inductively-Coupled-Plasma-Atomic-Emission-Spectroscopy
RSD: Relative Standard Deviation
TEM: Transmission Electron Microscopy
XPS: X-ray Photoelectron Spectroscopy
XRD: X-ray Diffraction

Structural Units: The units of length that are commonly used in discussions of nanocrystalline materials are the Angstrom (1 A = 10^{-10} m), the nanometer (1 nm = 10^{-9} m) and the micron (1 μm = 10^{-6} m).

Defect Notation: In the literature, the Kroger-Vink notation is the standard notation used to define defects in solids. The features of the Kroger-Vink can be described as follows[1]:

The main symbol: The defect species, which may be an ion, indicated by the atomic symbol for the species, or a vacant lattice site, denoted by V[1].

The subscript: Indicates the lattice or interstitial site occupied by the defect[1].

The superscript: Indicates the difference in charge at the defect site relative to the charge at that site in the perfect crystal. A dot is used for an extra positive charge, and a slash is used to denote an extra negative charge[1].

Example for the systems discussed in the following chapters:

Cation vacancy in CaO	$\mathbf{V''_{Ca}}$
Anion vacancy in CaO	$\mathbf{V^{\bullet\bullet}_{O}}$
Eu^{3+} substituted for Ca^{2+} in CaO	$\mathbf{Eu^{\bullet}_{Ca}}$

References

(1) Smyth, D. M. *The Defect Chemistry of Metal Oxides*; Oxford University Press: New York, 2000.

Table of Contents

Chapter 1. Introduction

1. A. Statement of Research Goals

The focus in this study of nanocrystalline materials is the use of the Eu^{3+} ion to probe the structures of two nanocrystalline systems. Recent studies of nanocrystalline ceramics have shown that tremendous changes in properties can be achieved compared to analogous materials with micrometer-scale structure. Relevant structural features include particle size distribution, shape, phase, and distribution of dopants. Since the particle size of these materials is between molecular and bulk, nanocrystals have hybrid properties that are not well understood. Gaining a deeper understanding into the structural changes that can occur when the particle size is reduced may be helpful for developing specific applications using nanocrystalline materials.

The size-dependent optical spectroscopy of nanocrystalline ceramics reveals structural changes, which are of interest for fundamental and applied research. Nanocrystalline Eu^{3+}:Y_2O_3 was studied by Bihari, Eilers, and Tissue and they found that the 23-nm crystals formed not in the usual cubic phase but in the monoclinic phase[1]. Similar results can be found in the literature[2]. For example, bulk Er_2O_3 exists in two hexagonal phases, but the nanocrystalline form of Er_2O_3 exhibits phases that are not present in the bulk material; monoclinic and face-centered cubic[2].

The results reported by Bihari, Eilers, and Tissue led to the interest in studying the luminescence spectra of smaller particles of Eu^{3+}:Y_2O_3 to see if further structural changes would occur. The results, which are presented in Chapter 3 in detail, showed that indeed structural changes occur as the particle size is systematically reduced. The structural

changes in nanocrystalline Eu^{3+}:Y_2O_3 stimulated an interest in studying a system in which the dopant ion has a different charge than the host ion. Since the Eu^{3+} ion and the Y^{3+} ion are isovalent, the substitution of an Eu^{3+} ion into the Y_2O_3 lattice is considered to be a trivial case of extrinsic ionic disorder since the impurity center is neutral relative to a perfect crystal. As a result, it is not necessary to have any other defects to maintain charge neutrality[3].

When a dopant ion and host ion have a different valency, defects are created to maintain charge neutrality. An investigation of the dopant distribution in nanocrystalline Eu^{3+}: CaO was chosen since the site-selective laser spectroscopic results of the bulk material were published and therefore provided background for investigating how reduction to the nanometer regime would affect the luminescence spectra and ultimately the dopant distribution in the nanocrystalline materials. Since nanocrystalline materials have a larger surface-to-volume ratio compared to bulk materials, it was speculated that the dopant distribution in the nanocrystalline materials would differ from the bulk material. Although many technologically important materials contain dopants, the issue of dopant distribution in nanocrystalline materials was not addressed in the literature as of 1998[4]. A recent paper by Zhang and Liu [5] explores the defect chemistry (dopant distribution) on the performance of gas sensors based on nanocrystalline Cu-doped SnO_2. They found that the substitution of Sn by Cu increases the concentration of oxygen vacancies and decreases the concentration of free electrons. The result of reducing the particle size to the nanometer range was a dramatic improvement in both sensitivity and speed of response in the sensors.

It has been suggested that the large number of grain boundaries in nanocrystalline materials may provide fast diffusion pathways for ionic defects, resulting in enhanced ionic conductivity[6]. Maier[7] has demonstrated that molecular beam epitaxy can be used to produce thin films of CaF_2 and BaF_2. These materials have an ionic conductivity that is 1000 times greater than bulk BaF_2 crystals. Maier attributes the increase to the defects from fluoride ion vacancies on the layer surfaces that arise when fluoride ions are redistributed by depositing CaF_2 and BaF_2 layers together.

In tracer diffusion studies on nanocrystalline monoclinic zirconium oxide, oxygen diffusivity in grain boundaries increased by 3-4 orders of magnitude compared to bulk zirconia[8]. These promising results suggest that the role of defect chemistry will be of major importance in understanding more clearly how the increased surface-to-volume ratio affects the structure and therefore the properties of nanocrystals.

1. B. Current Consensus on the Structure of Nanocrystalline Ceramics

1. B. 1. Preparation Methods

There are a variety of both chemical and physical methods for producing nanocrystalline ceramics. These include sol-gel synthesis [9,10], laser-vaporization, gas-phase condensation [11], plasma processing [12], mechanochemical synthesis [13], copolymer micelles [14], combustion synthesis [15,16], and sputtering techniques [17]. Regardless of the method of preparation, two primary goals are usually associated with nanocrystalline preparation: (1) small diameters (< 100 nm) and (2) narrow particle size distribution. Small diameters are preferred because above 100 nm, the properties tend to approach those of bulk materials. Narrow particle distributions are preferred for potential application purposes[18].

The evaporation-condensation process involves the condensation of metal or metal oxide vapors on a cold finger to form nanocrystalline metal oxides. Scandan and coworkers reported the preparation of nanocrystalline Y_2O_3 by evaporating yttrium metal from a resistively-heated tungsten crucible in helium[19]. Yttrium nanoparticles were condensed onto a cold finger, which was filled with liquid nitrogen. To achieve oxidation of the nanoparticles, helium was slowly replaced by oxygen. The oxidized nanoparticles were then transferred to a furnace and heated at 200 ^{0}C under pure oxygen to complete the oxidation process. The average particle size was 7 nm. The X-ray diffraction results showed that the nanoparticles were in the monoclinic phase and they attributed the formation of the monoclinic phase to the Gibbs-Thompson effect.

In 1992, Gunther and Kumpmann[20] reported the preparation of nanocrystalline Y_2O_3 using an electron beam as the source to evaporate the bulk material. Bulk Y_2O_3 was placed onto a water-cooled stage in a chamber filled with helium (1 mb). The sample was bombarded with a 45 kV electron beam and the resulting nanocrystals were 4-6 nm.

The laser vaporization of solids in an inert gas reactor was reported in 1982 [11]. The sample is locally heated, which results in vaporization. The vapor is cooled by collisions with inert gas molecules and the resulting supersaturation results in nanoparticle formation. Eilers and Tissue[21] used a continuous CO_2 laser as the source to evaporate bulk metal oxides of ZnO, Y_2O_3, and ZrO_2 to produce nanocrystals with a reproducible particle distribution. In their experiments, a pressed and sintered pellet of bulk material was placed on a rotating stage in a vacuum chamber. A cold finger was placed approximately 2 cm above the pellet for collection of the nanocrystals. They found that the average particle diameters obtained varied with the pressure of the nitrogen gas in the

chamber. For Y_2O_3, the average particle diameter was 4 nm for deposition in 1 Torr N_2 and 18 nm in 400 Torr N_2.

Nanocrystalline Y_2O_3 has been prepared by the homogeneous precipitation method by Sordelet and Akinc[22]. The yttrium stock solution was prepared with yttrium dissolved in a stoichiometric amount of nitric acid and diluted. Heating the aqueous solution with trichloroacetic acid produced the solid. In normal precipitation reactions, aqueous solutions are combined to produce precipitates of insoluble compounds by exceeding solubility limits. During the mixing process, large concentration gradients produce a broad distribution of particle sizes. The homogeneous method used by Sordelet and Akinc involved the gradual introduction of the precipitant which resulted in spherical particles with a diameter less than 0.1 μm. A particle size distribution was not provided.

The sol-gel method is a second example of a controlled precipitation reaction in which the particles do not precipitate but are dispersed in solution as colloids. Several reports of the sol-gel method to prepare nanocrystalline ceramics have been published. Guizard[23] and co-workers prepared Y_2O_3 nanocrystals and later, Bhargava and co-workers prepared Tb-doped Y_2O_3 nanocrystals by the sol-gel method. Bhargava and co-workers reported a particle size distribution of 25-55 angstroms, as determined by Transmission Electron Microscopy (TEM).

Combustion synthesis has been used to produce many nanocrystalline ceramics[15,24-26]. The combustion synthesis process utilizes metal salts and organic fuels. When properly controlled, high temperatures are generated by the exothermic redox reactions between the decomposition of the salts and the fuel. As a result of fast heating and cooling, there is little growth of crystals, which produces the nanoceramics. Shea, McKittrick, and

Lopez[15] reported that the average particle size of their nanoceramics (Cr^{3+}:$Y_3Al_5O_{12}$ and Eu^{3+}:Y_2O_3) prepared by the combustion method was dependent on the organic fuel used in the combustion. They reported particle sizes of 34, 54, and 41 nm for particles made by combustion with carbohydrazide, urea, and glycine, respectively. Particle size distributions were not reported. Fagherazzi and Polizzi[16] prepared nano-sized powders of Y_2O_3, $Y_{1.8}Er_{0.2}O_3$, and $Y_{1.8}Nd_{0.2}O_3$ by combustion synthesis and reported average particle sizes in the 20-30-nm range. Capobianco and co-workers[26] reported that the combustion synthesis of nanocrystalline Er^{3+}:Y_2O_3 resulted in the cubic phase with average particle diameters of 4-20 nm.

Monoclinic ytrrium oxide nanoparticles were prepared by Vogt by taking the bulk material and vaporizing it in the flame of an argon plasma. Upon quenching in hydrogen, the Y_2O_3 nanoparticles had a mean diameter of 21 nm [12].

In 2000, a homogeneous precipitation method was developed to control the particle size of nanocrystalline Eu:Y_2O_3 using ethylenediaminetetraacetic acid (EDTA)[27]. The influence of the EDTA on the morphology was evaluated using SEM micrographs. When the amount of EDTA was less than 0.4 g, monosized spherical particles were formed (300 nm). When the amount of EDTA was in the range of 0.5 g to 1.0 g, the morphology deviated from near-perfect spheres to irregular-shaped spheres with diameters up to 240 nm. With increasing amounts of EDTA (1.0 to 7.0 g), the particles became steadily smaller and non-spherical (reaching 20 nm at 7.0 g of EDTA). When the mass of EDTA was greater than 9.0 g no precipitate was observed. The authors argue that this method allows for control of the particle size from 20-300 nm. Although the data for the EDTA were presented in grams, it is actually the concentration of EDTA that is

relevant since the EDTA was added to aqueous solutions containing yttrium nitrate and europium nitrate at the beginning of each experiment. When the concentration of EDTA was large, no precipitation was observed. Presumably a large concentration of EDTA (which acts as a chelating agent) coordinates all of the metal cations, thereby preventing the CO_3^{2-} and OH^- ligands from forming yttrium hydroxycarbonate. Yttrium hydroxycarbonate is the material that is annealed to produce yttrium oxide[28].

There are advantages and disadvantages with all of the methods discussed and they can be placed into two categories: (1) methods that involve the formation of nanoparticles from the bulk starting material and (2) methods that involve the formation of nanoparticles from molecules. One potential problem that arises when nanoparticles are prepared from molecules (precipitation methods) is the removal of solvent from the final product. There is no solvent issue when nanoparticles are made from the bulk starting material. One limitation of the laser-vaporization-gas-phase condensation and sputtering methods is that only small amounts of nanomaterials can be made per unit time.

The atom clusters that comprise nanophase materials are frequently aggregated. The degree and nature of aggregation can vary from essentially none, to open arrays, to hard agglomeration [29]. According to Siegel, the difficulties that are encountered with the hard agglomerates are avoided in the gas-phase condensation method of preparing nanocrystals. The sample densities resulting from gas-condensed clusters at room temperature have ranged up to 97% for nanophase metals and up to 85% of theoretical for nanophase oxide ceramics [29].

For structural studies of nanocrystalline materials, it is crucial to realize that different methods used to prepare nanomaterials result in different particle sizes and distributions.

Particle size distributions are important since many characteristics of nanomaterials are linked to particle size.

1. B. 2. Structural Studies

The structures of nanocrystalline ceramics have been investigated by a number of methods, the most common being transmission electron microscopy and powder X-ray diffraction. The morphology, the average particle diameter, and the particle size distributions can be established using TEM. In addition, TEM studies can provide grain growth information when nanocrystals are annealed. Powder X-ray diffraction is used to detect phase transformations and the X-ray diffraction line widths can provide an independent measure of particle size. The particle diameter can be calculated from the width of the lines in the XRD pattern, the Scherrer formula[30] can be used:

$$d = 0.9 \lambda / B \cos \theta_B$$

where: d = average particle diameter (nm)
λ = X-ray wavelength (0.1542 nm)
B = width of diffraction peak at half maximum
θ_B = angle of incidence of the X-ray beam at the maximum of the diffraction peak

The XRD measurements do not provide information on the particle size distribution. Powder XRD measurements have been used to model the structure of nanocrystals since it is possible to obtain fits of XRD patterns by assuming bulk lattice parameters; however, the information that can be obtained is limited with respect to aperiodic parts of the nanocrystal[31].

High resolution electron microscopy studies of nanocrystalline ceramics indicate that the atomic structures of grain boundaries consist of both ordered and disordered

regions[32]. Li and co-workers reported that the atomic structures of the disordered regions at the grain boundaries are modified very slowly towards more ordered structure under electron beam irradiation. Additionally, they reported that the nature of dislocation defects is similar to those normally observed in bulk polycrystals.

Many spectroscopic methods have been used to study nanocrystalline ceramics including Mössbauer, laser-induced luminescence[33], Raman spectroscopy[34], infrared absorption[35], positron annihilation[36], and X-ray photoelectron spectroscopy[35].

A recent structural determination study on titanium-oxide nanoparticles was performed using X-ray absorption spectroscopy (XAS)[37]. In XAS, the cross section of an absorbing atom depends on the scattering of the photoelectron wave from the neighboring atoms, which provides information about the local structure surrounding the absorber[37]. The data demonstrate that defects and surface states affect the X-ray absorption spectra.

Little information about the surface structure of nanocrystals is available. In 1999, Alivisatos and co-workers published their observations on the size dependent structural disorder by X-ray absorption near-edge spectroscopy (XANES) in InAs and CdSe nanocrystals[31]. Where EXAFS mainly probes the arrangement of neighboring atoms with respect to the absorbing atom, the XANES spectrum is sensitive to the relative arrangement of multiple atoms due to the increased contribution of multiple-scattering effects[31]. According to Alivisatos and co-workers, one can extract more complex information from XANES spectra, such as bond angles. Alivisatos and co-workers believe that the observed broadening in the XANES spectra of the nanomaterials is due to atomic displacements at the surface. Since the structures of nanocrystals have an

important impact on their behavior, learning more about defects in nanostructured materials will be crucial to better understand these materials.

Raman spectroscopy has been recognized as an important structural probe for nanocrystalline materials and has been used recently to study nanocrystalline GaN with an average particle diameter of 50 nm[38]. The photoluminescence spectrum of the nanocrystalline material showed a broad weak emission around 2.2 eV, which was attributed to the presence of a surface mode that is characteristic of phonons in nanocrystallites rather than a general defect-related band. These results suggest that the surfaces of nanocrystals affect the luminescence behavior of these materials.

1. B. 3. Phase Transformations

The optical spectra of nanocrystalline materials are different for different phases[39]. Therefore, this study of the particle size dependence on the luminescence spectra of Eu^{3+}:Y_2O_3 and Eu^{3+}:CaO includes phase information. It is known from the literature that metal oxide nanocrystals can undergo phase transformations[40,41].

The agglomeration and phase transformation behavior of nanophase iron oxide with a mean particle diameter of 3 nm was published in 1993[40]. The analytical techniques used in the study involved TEM, Mossbauer spectroscopy, and thermogravimetric analysis (TGA). The authors reported that initially the 3-nm oxide appeared amorphous but after annealing at 250 ^{0}C for 24 hours, the sample exhibited hexagonal symmetry. The phase information was obtained from an electron diffraction spot pattern. TEM studies performed on the annealed sample revealed that a small fraction of the larger particles (larger than the reported mean) were 15-nm after annealing. The authors reported, however, that a "considerable percentage" of 3-nm particles remained after the annealing.

In 2000, high-pressure structural transformation of CdSe nanocrystals was reported[42]. CdSe crystallites with an average size of 45 angstroms were loaded into a diamond anvil cell with a diffraction slit and X-ray diffraction patterns were collected with image plates. The pressure was changed in 0.5-1 GPa steps that were spaced about one hour apart. The nanocrystals start as wurtzite with a shape corresponding to either a cylinder or an ellipse. Under pressure, the nanocrystals converted to a slab-shaped rock-salt structure. In summary, their results showed that nanocrystals can undergo phase transformations under specific conditions, which allows for some control over the morphology of nanophase materials.

1. B 4. Structure-Dependent Properties of Nanocrystalline Ceramics

Since the atomic structure of nanocrystalline ceramics differs from structures of bulk materials, the structure-dependent properties are expected to be different from the properties of the bulk[41,43]. In the following sections, existing observations on the structure-dependent properties are presented.

1. B. 4. 1. Thermal Properties

One early study of a change in physical properties as a function of particle size was reported in 1992 by Goldstein, Echer, and Alivisatos [44]. The semiconductor nanocrystals had a lower melting temperature compared to that for bulk material. In 1995, Tolbert and Alivisatos reported a lower effective Debye temperature of their nanocrystalline semiconductors [45].

Sintering is a process in which interparticle pores are eliminated by atomic diffusion and is used in the manufacturing of industrial ceramics. A sintering study of bulk and nanocrystalline yttrium-doped zirconia was published by Bourell and Kaysser[10] to

compare the densification in the materials. Densification of the nanocrystalline ceramic was initiated at 800 K for the 40-nm particle and 1100 K for the 1100-nm particle. Full density was obtained at approximately 1500 K, several hundred degrees below the sintering range for the bulk ceramic. In the nanocrystalline sample, the grain size diameter was 80 nm after sintering at 1570 K. which correlated with the grain-growth kinetics in the bulk. Bourell and Kaysser concluded that nanocrystalline yttrium-doped zirconia may be successfully sintered below 1600 K with minimal grain growth.

1. B. 4. 2. Mechanical Properties

Ceramics are hard, brittle, and difficult to machine. However, with a reduction in particle size, nanocrystalline ceramics exhibit superplasticity. Superplasticity is the ability of a plastic to deform to unusually large elongations without damage to mechanical properties. An early study of low-temperature plastic deformation of nanocrystalline CaF_2 and TiO_2 was performed by Karch, Birringer, and Gleiter in 1987[46]. According to the authors of the study, nanocrystalline ceramics are expected to exhibit enhanced plastic deformation due to enhanced diffusional creep for two reasons: (1) reduced particle size which enhances the creep rate and (2) enhanced boundary diffusivity which increases the creep rate.

Later studies on zirconia, which is a hard brittle ceramic in the bulk, showed that the nanocrystalline ceramic can deform up to 300 % of its original length[47]. The superplastic behavior can be described by the following equation[47]:

$d\varepsilon/dt = A\,\sigma^n\,d^{-p}\exp(-Q/RT)$ where A = material dependent factor, σ = applied stress, n = stress exponent, d = mean grain size, p = grain size exponent, Q = activation energy for creeping, R = gas constant, T = temperature and $d\varepsilon/dt$ = strain rate. According to Siegel

et al, as a result of this superplastic phenomenon, nanocrystalline ceramics are expected to greatly affect the aerospace industry as well as others. Since superplasticity is generally defined as the ability to deform without damage to mechanical properties, materials that have superplastic abilities may be used for airplane parts, automobile parts, and other applications that require materials that are strong yet flexible.

Hardness and strength of conventional materials are a function of grain size[48]. The Hall-Petch equation expresses the grain-size dependence of material hardness. Shang, Cammarata, and Weihs used the equation to obtain the relationship between material hardness and particle size. The form of the equation used to derive the plot was: $\sigma_y = \sigma_o + kd^{-1/2}$ where σ_o is frictional stress, d is grain size, k is Hall-Petch slope and σ_y is yield stress.

The experimental results of hardness measurements of nanocrystalline ceramics must be carefully reviewed because most nanocrystalline materials that have a positive Hall-Petch slope have been annealed. Thermally treating nanophase samples may result in changes in structure such as densification, stress relief, phase transformations, or grain-boundary structure, all of which may lead to a negative Hall-Petch slope[29]. A few cases of negative Hall-Petch behavior have been reported for as-prepared nanocrystalline materials[49]. Therefore, strength and hardness of nanocrystalline ceramics is unique and not well understood.

1. B. 4. 3. Magnetic Properties

Magnetic properties of nanophase ceramics are sensitive to particle size and shape[50]. A recent annealing study of Fe_2O_3 nanoparticles was performed to determine the magnetic size effects and phase transformations that occur with the reduced particle

diameter[51]. It is well-established in the literature that the growth of nanocrystalline metal oxides may result in phase transformations. The magnetic size-effect study revealed that nanophases of γ-Fe_2O_3 with various average particle sizes can be obtained by annealing Fe_2O_3 nanoparticles in vacuum at temperatures of 240-450 ^{0}C and times of 2-6 hours[51]. The growth of the γ-Fe_2O_3 nanocrystallites proceeded via the formation of an intermediate Fe_3O_4 phase. The γ-Fe_2O_3 nanocrystallites with an average size of less than 12 nm showed magnetic characteristics that differed strongly from the bulk γ-Fe_2O_3 phase. Annealing of γ-Fe_2O_3 nanoparticles in air resulted in a direct transformation into the α-Fe_2O_3 nanophase.

1. B. 4. 4. Chemical Properties

The discovery in 1993 of catalytic activity in metal oxide nanocrystals has resulted in a branch of research that is focused on nanocrystalline materials as catalysts [52]. In 1993, Labeau and co-workers investigated the sensitivity of a nanocrystalline Pt-doped SnO_2 gas sensor [53]. Their results indicated that the nanoparticles gave increased sensitivity. They reasoned that the nanoparticles probably act as a catalyst for the adsorption of CO and ethanol molecules, which leads to a lower energy of activation for surface reactions.

Due to the increase in surface area with reduced particle size, nanocrystalline ceramics (MgO, CaO, and Al_2O_3) have been studied for their applicability as adsorbents for air purification[54] Compared to high-surface-area activated carbon, the nanocrystalline ceramics exhibited higher capacities and the ability to adsorb organic compounds.

1. B. 4. 5. Conductivity

It has been suggested that the large number of grain boundaries in nanocrystalline materials may provide fast diffusion pathways for ionic defects, resulting in enhanced ionic conductivity[6]. The results in the literature regarding this issue are controversial.

It is well-known that grain boundary diffusion in ceramics is often orders of magnitude greater than corresponding diffusion through the grains[55]. This concept was illustrated in 1989 in diffusion studies on NiO in which the grain boundary diffusivity of oxygen at 1300 ^{0}C was approximately six orders of magnitude higher than in the lattice[55]. According to Tuller[55], grain boundaries appear to possess two key characteristics necessary for enhanced ionic diffusion: high defect densities and high mobilities. Tuller[55] argues that there are surprisingly few cases in which the source of enhanced diffusion at grain boundaries has been well established.

In the last several years, a number of nanocrystalline ceramics have been prepared as nanostructures and the transport properties have been published[8]. A recent study[56] on the local and overall ionic conductivity in nanocrystalline CaF_2 revealed that nanocrystalline CaF_2 shows a significantly higher overall conductivity than the micro-crystalline material. The authors believe that the higher overall conductivity in the nanocrystals is due to the large fraction of interface regions in nanocrystalline materials[56]. Since the reduction of the particle size to the nanometer regime results in a greater surface area, there is a larger fraction of interface regions. A greater fraction of interface regions in nanocrystalline materials would also be expected to affect the luminescence spectra in nanocrystalline materials.

Cerium oxide is a well-known oxygen conductor and the effect on grain size on the electrical conductivity has been investigated[8]. The nanocrystalline samples exhibited electronic conductivity under conditions where the bulk samples showed impurity-controlled ionic conductivity. The electronic conductivity was larger than the intrinsic electronic conductivity of pure single crystalline cerium oxide and increased with decreasing grain size.

1. B. 4. 6. Optical Properties

When electrons are confined in a small domain, such as a nanoparticle, the system is commonly referred to as quantum confinement[43]. Quantum confinement changes the overlap of the wave functions of the activator (impurity) atoms with those of host atoms. As a result, there are more efficient interactions between the activator and host atoms[41]. Brus suggested in 1983 that quantum confinement effects could be used effectively in semiconductor nanoparticles [57]. In the literature, quantum-confined semiconductors are typically referred to as quantum dots[43]. Quantum dots can be used to produce light emitters of different colors by "tuning" using particle-size effects instead of synthesizing compound semiconductors [58]. In 1994, Colvins, Schlamp, and Alivisatos reported that the color of emission could be varied from red to yellow by changing the particle size of CdSe nanocrystals [59]. They assembled CdSe nanoparticles on the surface of an electroluminescent polymer and observed emission of green light from the polymer and red light from the nanoparticle layer. This "tunability" was achieved as a function of the applied voltage.

Although quantum dot applications seem attractive, the processes for producing quantum dots are technologically demanding, according to Kruis, Fissan, and

Peled [58]. They argue that there should be good control of particle size and shape, as well as stability against degradation. Therefore, studying the structural changes that occur when nanocrystals are produced is crucial for engineering purposes.

In 1997, Goldburt, Kulkarni, Bhargava, Taylor, and Libera published a paper on the variation of luminescent efficiency with the size of doped nanocrystalline Tb:Y_2O_3 phosphors [60]. They reported that the decrease in the particle size of the doped nanocrystalline phosphor resulted in increased photoluminescent efficiency. The decrease in particle sizes results in the overlap of exciton wave functions with those of the activator (impurity). The increased overlap enhances the energy transfer rate from the excitons to the impurities and as a result, the non-radiative decay rate is reduced and therefore the photoluminescent efficiency is increased[61].

Presently several applications of doped nanocrystalline materials are being developed for displays, ultra-fast sensors, and lasers [62]. According to Bhargava, doped nanocrystalline materials (DNC), such as Eu^{3+}: Y_2O_3, can be excited at much lower voltages (≈ 1 kV) than the bulk materials. As a result, DNC phosphors are ideal candidates for flat panel display applications since the maximum voltage that can be applied in flat panel display devices (≈ 1 kV) is smaller than normal display devices (≈ 5 kV)[62].

In summary, numerous investigations have dealt with the properties of nanocrystalline ceramics as a function of structure and will undoubtedly continue since future applications of nanostructured ceramics depend on the structure-property relationship. One method of probing the structure of nanocrystalline ceramics is to use laser-induced

lanthanide luminescence, since the technique is more sensitive to subtle phase changes than powder X-ray diffraction[4].

1. C. Overview of Lanthanide Luminescence as a Probe of Nanocrystalline Structure

The lanthanides have a well-documented history in studies of luminescence primarily for the fact that the f-f transitions produce narrow lines. Since the 4f electrons of the lanthanides are shielded from perturbations with the lattice by the outer 5s and 5p electrons, the 4f orbitals retain their hydrogenic character, resulting in sharp transitions between the 4f levels. A thorough review of the early spectroscopic work of lanthanides is provided by Dieke [63]. Current work on lanthanide luminescence is diverse in scope due to both fundamental interest and potential applications.

In addition to the technologically important applications, lanthanides serve as a probe of their local chemical environment. As mentioned in the foregoing paragraph, the 4f transitions are sharp and the 4f orbitals are sensitive to their local crystal field. Consequently, the J-multiplet levels are split and the splitting pattern is dependent on the strength of the crystal field and local site symmetry. Therefore, the luminescent spectra consist of lines that are characteristic of the local chemical environment.

A study of the optical spectroscopy of lanthanide ions in bulk materials has contributed to a better understanding of the crystallinity, structure, phase distributions and defect chemistry in these materials. These types of measurements have been demonstrated previously in a variety of bulk materials. Several pertinent examples include degree of disorder [64], defect aggregation kinetics [65] and defect equilibrium [66].

A specific lanthanide ion of interest is Eu^{3+}, which has been studied in several different hosts, but most commonly in Y_2O_3 due to its use as a commercially viable red phosphor. Eu^{3+}:Y_2O_3 has been used commercially for cathode ray tube displays, scintillators, and other display technologies due to high radiant efficiency and temperature stability[67].

The preparation of Eu_2O_3 and Y_2O_3 to produce the doped material is achieved by first dissolving the desired molar concentrations of the oxides in hot nitric acid, followed by treatment with oxalic acid. Further treatment, which is described in detail elsewhere, [68] results in the cubic phase. Excitation and emission spectra of cubic Eu^{3+}:Y_2O_3 can be found in the literature [69]. Line emission is normally observed from the $^5D_2$, $^5D_1$, and $^5D_0$ levels to the ^7F_J ground levels. The dominant emission is from the $^5D_0$ excited state at 611 nm with a lifetime of approximately 1 ms [68]. Two cation sites are available in the host for Eu^{3+} occupation: a C_2 site and C_{3i} site [68].

1. D. Thesis Summary

Since the Eu^{3+} ion can occupy different cation sites in a host material, it can serve as a useful probe of nanocrystalline materials to gain more insight into the structural changes that can occur when the particle size is reduced from the bulk to nanometer regime. In chapter 2, the use of the Eu^{3+} ion to probe the structure of bulk monoclinic yttrium oxide is discussed. The luminescence spectra of bulk monoclinic Eu^{3+}:Y_2O_3 had not been published prior to this study and therefore the results that were obtained provided a baseline to study nanocrystalline Eu^{3+}:Y_2O_3.

In chapter 3, a particle size study on the luminescence spectra of nanocrystalline Eu^{3+}:Y_2O_3 is presented. The results show that the systematic reduction of the particle

size results in phase changes. In nanocrystalline Eu^{3+}:Y_2O_3, the dopant cation and host cation have the same charge and as a result, there is no defect chemistry to consider.

In chapter 4, the preparation, characterization, and broadband excitation spectra of nanocrystalline Eu^{3+}:CaO are presented. Calcium oxide is an interesting material to study because all of the important sites that a dopant ion can occupy can be characterized using laser spectroscopic techniques[70]. Nanocrystalline Eu^{3+}:CaO has not been reported in the literature; therefore, the work presented in chapter 4 is the first report of this material.

In chapter 5, an initial survey of site-selective spectroscopy of nanocrystalline Eu^{3+}:CaO is presented. The site-selective data reveal whether the europium ions are occupying the cubic site or the orthorhombic site within the host lattice. As a result, the cubic/orthorhombic ratio can be investigated as a function of dopant concentration. First, a concentration study as a result of doping is presented. Following the concentration study, the phase distribution is investigated. The results from the phase distribution study led to an annealing study since the phase distribution study revealed the formation of a secondary phase; monoclinic Eu_2O_3. The purpose of the annealing study was to see what effect annealing would have on the metastable secondary phase.

Since the site-selective spectroscopy data would be used to determine the dopant distribution in the nanocrystals, the reliability of the measurements had to be tested. Experiments in which the effect of scan rate and annealing on the spectroscopic measurements are presented. The experiments revealed that scan rate and annealing did have an effect on the variation in the cubic/orthorhombic ratio. The site-selective laser spectroscopy could be used to determine the cubic/orthorhombic ratio in the single-phase

non-annealed samples if the intensity of the lines in site A are compared to the B site line. Therefore, the cubic/orthorhombic ratio is investigated as a function of dopant concentration in the single-phase non-annealed samples. These preliminary measurements suggest that the dopant distribution (defect chemistry) in a nanocrystalline system is different from that of bulk. Additionally, a prediction of the particle size at which the defect chemistry will be affected is presented.

In chapter 6, a summary of conclusions regarding the particle size dependence on the luminescence spectra of Eu^{3+}:Y_2O_3 and Eu^{3+}:CaO is presented.

Chapter 2. Fluorescence Spectroscopy of Bulk Monoclinic 0.1 mol % Eu^{3+}:Y_2O_3.

2. A. Review of the Eu^{3+} ion in Monoclinic Structures

Eu_2O_3 through Dy_2O_3 in the lanthanide series can form in the monoclinic structure at high temperature or high pressure [71-73], but Y_2O_3 and lanthanide sesquioxides with an ionic radius smaller than that of Dy_2O_3 require both high temperature and high pressure[71]. The monoclinic phase of these sesquioxides has a space group C2/m and the lattice possesses three crystallographically distinct cation sites, each having point group symmetry C_s [74,75]. All three cation sites are 7-fold coordinated and are represented in Figure 2-1. The coordination of two cation sites (Ln I and Ln II) can be described by six oxygens at the apexes of a trigonal prism with a seventh oxygen lying along the normal to a face. The coordination of the third site (Ln III) is described as a distorted octahedron with a seventh oxygen at a long distance [71,74,75]. Formation of nanocrystalline Y_2O_3 in the monoclinic phase under ambient conditions has been attributed to an additional hydrostatic pressure component, resulting from the Gibbs-Thomson effect [76]. Optical spectroscopy studies of bulk monoclinic lanthanide sesquioxides have been limited to Eu_2O_3 [73,77] and Eu^{3+}:Gd_2O_3 [75,78].

Preparing nanocrystalline Y_2O_3 by gas-phase condensation results in the formation of the monoclinic crystal structure [1,21,76] rather than the usual cubic structure [72]. Optical studies of 23-nm monoclinic Eu^{3+}:Y_2O_3 were performed by Bihari, Eilers, and Tissue[1]and as a result of their findings, a spectroscopic study of bulk monoclinic Eu^{3+}:Y_2O_3 was initiated since the luminescence of bulk monoclinic Eu^{3+}:Y_2O_3 was not available in the literature. Since one goal was to study how systematically reducing the particle size would affect the luminescence spectra of nanocrystalline Eu^{3+}:Y_2O_3, obtaining the

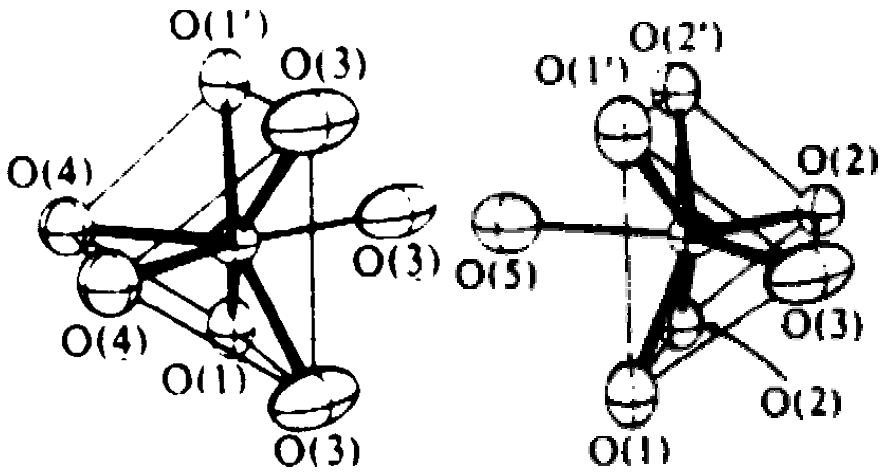

Site A (Ln I) Site B (Ln II)

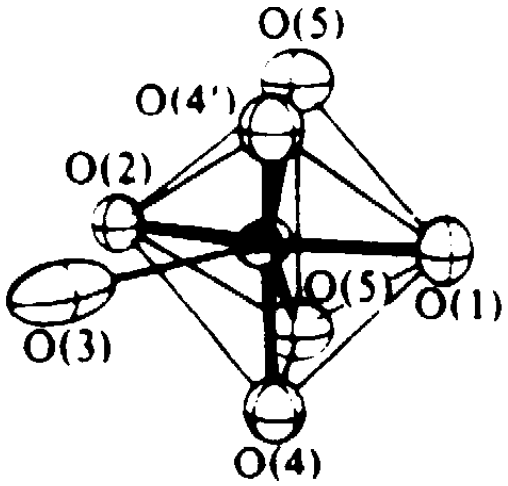

Site C (Ln III)

Figure 2-1. The monoclinic phase of Y_2O_3 has a space group C2/m and the lattice possesses three crystallographically distinct cation sites, each having point group symmetry C_s [74,75]. All three cation sites are 7-fold coordinated and are defined in the literature[71,74,75] as sites A, B, and C.

luminescence spectra of the bulk monoclinic system was crucial for comparative purposes.

Figure 2-2 shows a partial energy level diagram of the Eu^{3+} ion in a solid host. Each energy level shown in Figure 2-2 can be split into 2J + 1 sublevels, and this fine structure is sensitive to the local crystalline field surrounding the Eu^{3+} ion. Therefore, distinct spectra arise from the Eu^{3+} ions in different crystallographic cation sites. The spectra in this thesis follow the site A, B, and C labeling notation, as in the literature [75,77].

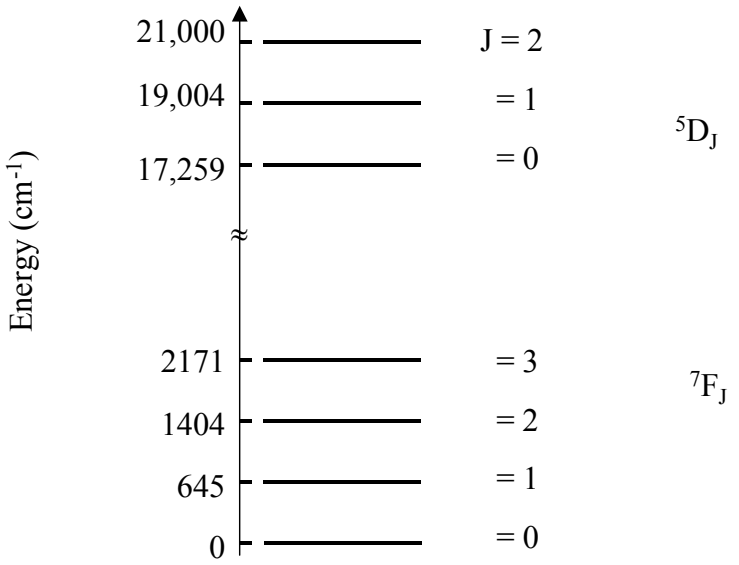

Figure 2-2. Partial energy level diagram of the Eu^{3+} ion in solids. Each level can be split into 2J + 1 sublevels.

2. B. Experimental

The bulk monoclinic 0.1% Eu^{3+}:Y_2O_3 sample was prepared by Dr. James McHale at the Princeton Materials Institute at Princeton University, Princeton, New Jersey. The sample was prepared by dissolving 0.1085 g $Y(NO_3)_3 \bullet 6H_2O$ (Johnson Matthey, 99.9%) and 1.6 x 10^{-5} mol Eu_2O_3 (Aldrich, 99.95+%) in 100 mL of distilled H_2O and 1 mL of ≈70% HNO_3(aq). A hydrous oxide gel precipitated from this solution by adding NH_4OH. The gel was filtered and the precipitate was washed several times with distilled H_2O and then calcined at 1000 ^{0}C for 24 h to produce Eu^{3+}:Y_2O_3 with the cubic structure. This material was transformed to the monoclinic structure by application of high pressure and high temperature. Approximately 50 mg of the cubic Eu^{3+}:Y_2O_3 was loaded into a 10 mm segment of 3 mm i.d. Pt tubing, which was then welded closed on both ends. The tubing was loaded into a Quick Press piston cylinder apparatus (Depths of the Earth Co.) and heated from 30 to 1100 ^{0}C while the pressure was slowly increased to 25 kbar. The pressure medium was pyrophyllite. The sample was maintained at 25 kbar and 1100 ^{0}C for 1 hr and then was quenched to room temperature in approximately 1 min. The pressure was released slowly and the sample was extracted from the Pt capsule. The resulting material was identified as monoclinic Eu^{3+}:Y_2O_3 from the powder X-ray diffraction pattern.

For optical spectroscopy, the materials were placed into a depression on a copper sample holder, which was mounted on the cold head of a closed-cycle refrigerator (Cryomech GB 15). A schematic of the experimental components are shown in Figure 2-3. All of the spectra were recorded at a sample temperature of 13 K ± 2K. All spectra and decay transients were recorded using a pulsed Nd^{3+}:YAG-pumped dye laser with

Coumarin 540A dye as the excitation source. Broad-band excitation spectra were recorded by scanning the laser and monitoring fluorescence with a 0.25-m monochromator with a bandpass of 6 nm and a photomultiplier tube (Hammamatsu P-28). Fluorescence spectra were recorded by tuning the laser to an excitation line and scanning a 1-m monochromator (Spex 1000M) that was equipped with a cooled GaAs photomultiplier tube (Hammamatsu R-636). The photomultiplier signals were processed with a boxcar averager (Stanford SR250) and stored using an analog-to-digital data-acquisition board (National Instruments Lab-PC+) and LabView computer program. Fluorescence transients were recorded with a 350-MHz digital oscilloscope (Tektronix TDS460) after typically averaging 200 laser shots. The schematic is shown below:

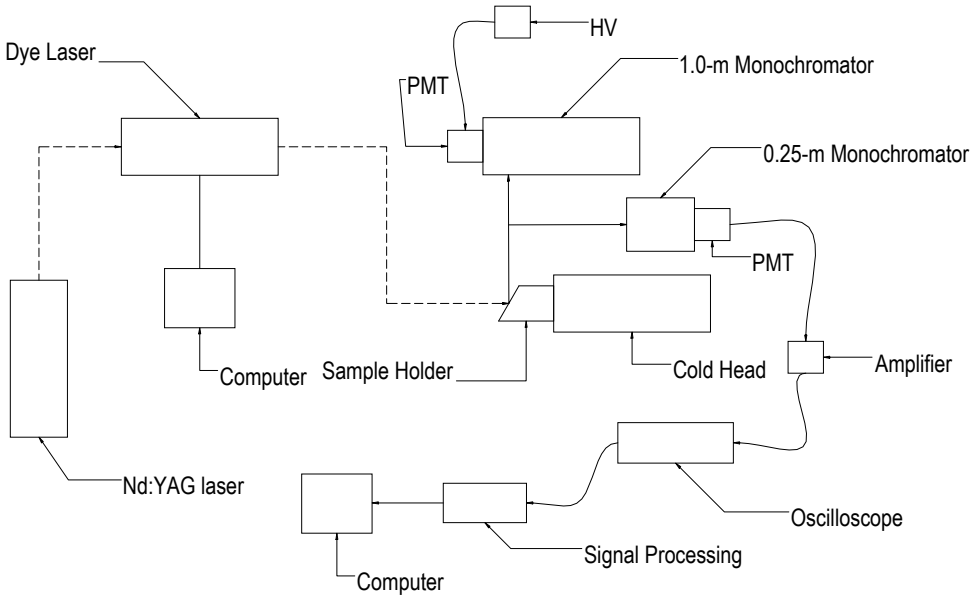

Figure 2-3. Schematic of the laser spectroscopic instrumental arrangement used for obtaining excitation, fluorescence, and transients spectra. (AutoCAD drawing by Ryan Williams, student, Dept. of Computer Engineering, Virginia Tech, Blacksburg, Virginia, January 2002).

2. C. Results and Discussion

2. C. 1. Characterization Results

Figure 2-4 shows the powder X-ray diffraction pattern of the bulk monoclinic 0.1 mol % Eu^{3+}:Y_2O_3 sample, as recorded by Jim McHale at the Princeton Materials Institute at Princeton University, Princeton, New Jersey. The line positions match the published diffraction pattern for monoclinic Y_2O_3, [12] with the exception of three small unassigned reflections at $2\theta = 41.5$, 52.7, and 56.2^0.

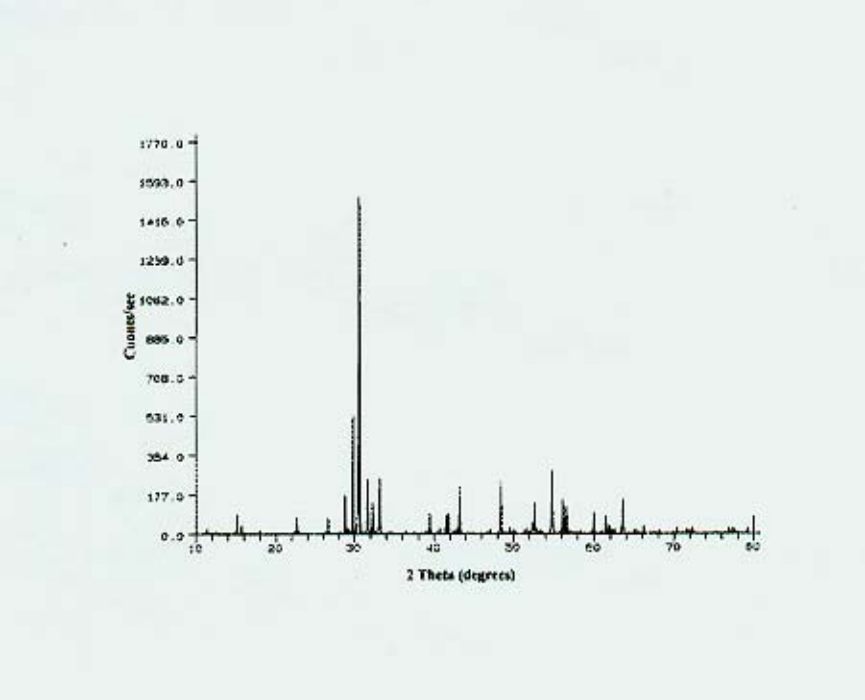

Figure 2-4. XRD pattern of bulk monoclinic 0.1 mol % Eu^{3+}:Y_2O_3, as recorded by Jim McHale at the Princeton Materials Institute at Princeton University, Princeton, New Jersey.

2. C. 2. Laser Spectroscopy Results

Figure 2-5 shows the $^7F_0 \rightarrow {}^5D_0$ excitation spectrum of bulk monoclinic Eu^{3+}:Y_2O_3. There are three sharp lines at 579.4, 582.7, and 582.9 nm, corresponding to sites A, B, and C, respectively. The use of the low resolution monochromator for recording the excitation spectra, as described in the preceding experimental section, prevents selective monitoring of only portions of the fluorescence lines and provides a measure of the inhomogeneous broadening in the excitation spectra.

Figure 2-6 shows the $^7F_0 \rightarrow {}^5D_1$ excitation spectrum of the bulk monoclinic 0.1 mol % Eu^{3+}:Y_2O_3. The excitation lines at 526.09 and 527.31 nm correspond to transitions associated with site A; the lines at 528.2, 528.5, and 529.2 nm correspond to site B; and the lines at 528.6, 528.7, and 528.8 nm correspond to site C. Site assignments were made by recording the fluorescence spectrum for each line in the excitation spectrum. This was achieved by tuning the dye laser to resonance successively with each line and scanning the 1-m monochromator. Each site had a distinct fluorescence spectrum, which allowed the individual sites to be distinguished.

Figure 2-7 shows the luminescence spectra of bulk monoclinic 0.1% Eu^{3+}:Y_2O_3 when exciting a $^5D_1$ level for sites A, B, and C. The lines clustered near 590 nm are due to $^5D_1 \rightarrow {}^7F_3$ and $^5D_1 \rightarrow {}^7F_{0,1}$ transitions, and the lines clustered near 620 nm are due to $^5D_1 \rightarrow {}^7F_4$ and $^5D_0 \rightarrow {}^7F_2$ transitions. The lines originating from $^5D_1$ and $^5D_0$ can be distinguished by their different temporal behavior.

Exciting site A resulted in emission lines of weak intensity for the $^5D_1$ transitions at 587.5, 589.0, and 593.9 nm. Site B excitation produced sharp emission lines at 586.7,

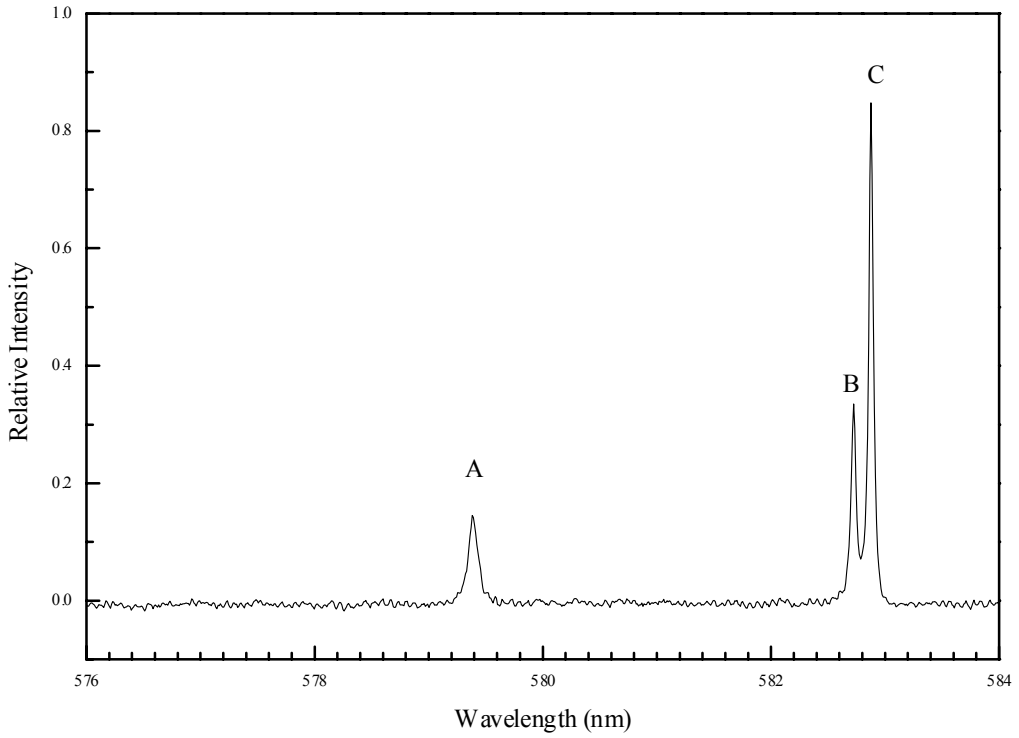

Figure 2-5. $^7F_0 \rightarrow {}^5D_0$ excitation spectrum of bulk monoclinic 0.1 mol % Eu^{3+}: Y_2O_3. The wavelength monitored was 624 nm.

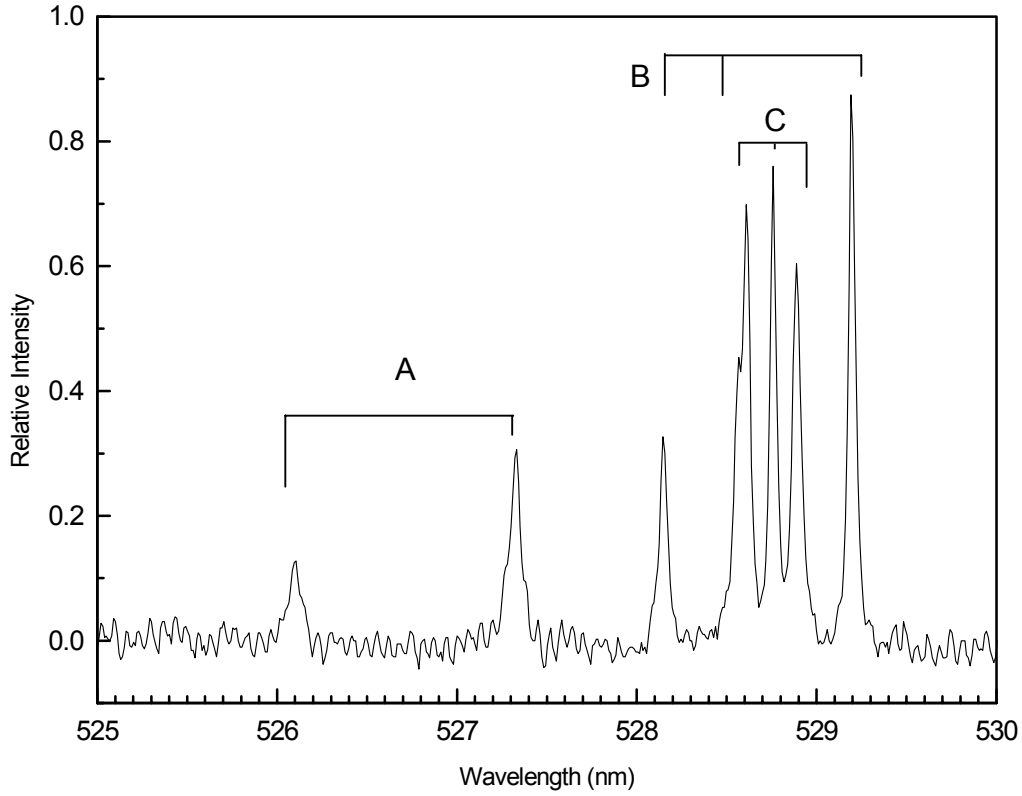

Figure 2-6. $^7F_0 \rightarrow {}^5D_1$ excitation spectrum of bulk monoclinic 0.1 mol % Eu^{3+}:Y_2O_3. The wavelength monitored was 624 nm.

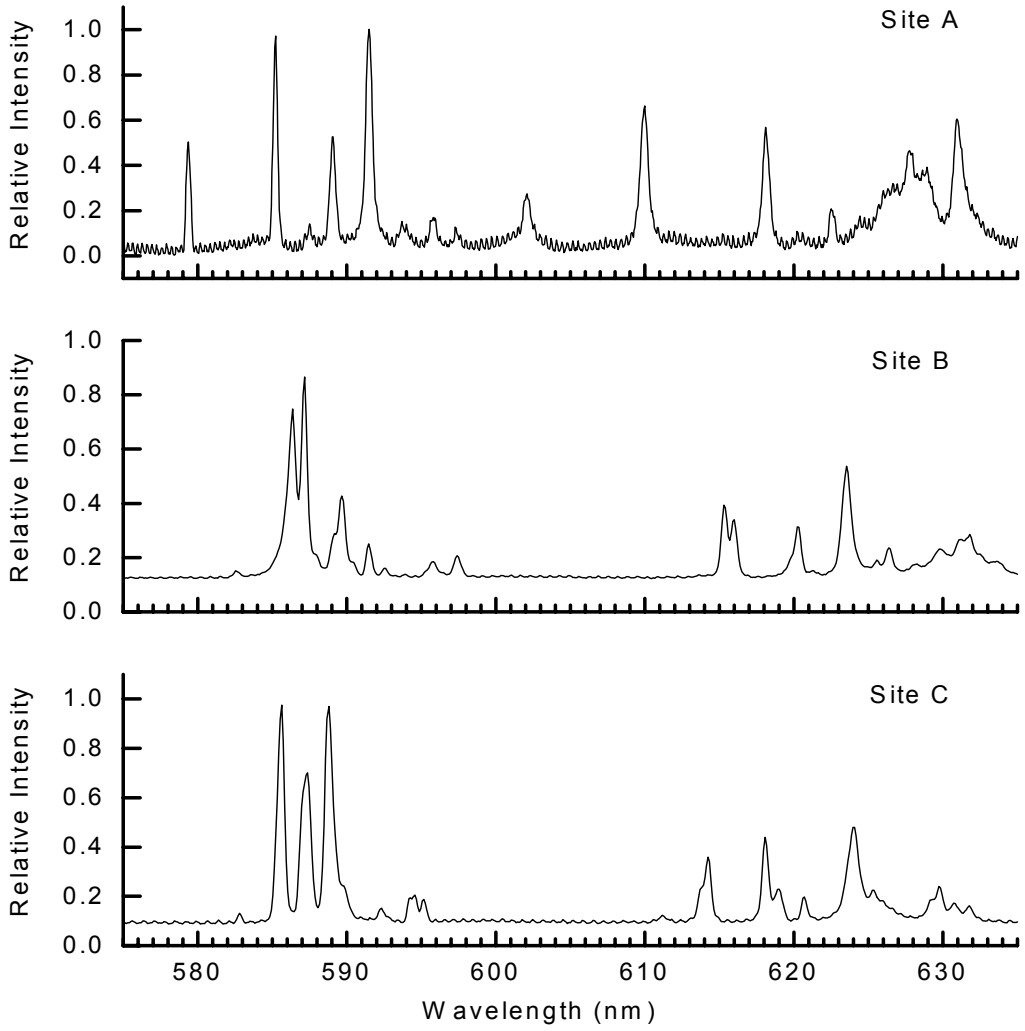

Figure 2-7. Emission spectra of bulk monoclinic 0.1 mol % Eu^{3+}:Y_2O_3 exciting the $^5D_1$ level. The excitation wavelengths were 527.3, 529.2, and 528.7 nm for sites A, B, and C, respectively. The boxcar delay and gate widths were 1 and 150 μs, respectively, and the bandpass of the 1-m monochromator was 0.2 nm.

587.5, and 623.7nm. The 586.7 and 587.5 nm lines correspond to $^5D_1 \rightarrow {}^7F_3$ transitions. Excitation of site C revealed sharp lines at 585.7, 588.8, 589.0, and 624.5 nm and several other lines of weaker intensity. The lines at 585.7 and 588.8 correspond to $^5D_1 \rightarrow {}^7F_3$ transitions. A distinct difference in the spectra of site A compared to sites B and C is a relatively intense $^5D_0 \rightarrow {}^7F_0$ emission line. This transition is nominally forbidden, and is usually quite weak. The dynamics (discussed in the next paragraph) suggest that site A has a stronger electron-phonon coupling than sites B and C, and the strong $^5D_0 \rightarrow {}^7F_0$ emission of site A is consistent with that supposition. Electron-phonon coupling is the interaction between the electronic states of a dopant and the phonons (vibrations) of the host lattice and variations in the electron-phonon coupling are observed for different transitions and different host lattices[79].

Figure 2-8 shows the $^5D_0 \rightarrow {}^7F_2$ emission spectra of bulk monoclinic 0.1% Eu^{3+}:Y_2O_3 when exciting the $^5D_0$ level of sites A, B, and C. The emission spectra of site A had an intensity lower than that of sites B and C spectra, and it also had more lines than expected for the $^5D_0 \rightarrow {}^7F_2$ transition. On the basis of the number of site A lines in Figure 2-4, the emission line at 601.9 can be assigned as a $^5D_0 \rightarrow {}^7F_1$ transition. The lines at 609.7, 617.7, 627.7, and 630.6 nm are strong and sharp and can be assigned as $^5D_0 \rightarrow {}^7F_2$ transitions. The other features in the spectrum appear as broad or weak shoulders and are probably vibronic bands or satellite lines. The only difference between these assignments and the work on monoclinic Eu^{3+}:Gd_2O_3 is that the 631.0 nm line in Eu^{3+}:Gd_2O_3 was assigned as a vibronic sideband [75]. The emission spectrum of site B has sharp lines at 615.5, 616.2, and 623.7 nm and a broad, structured feature at 631.4 nm. The emission

spectrum of site C has sharp lines at 614.8, 618.7, and 624.6 nm and a shoulder at 626.2 nm. The line at 614.8 nm appears to be an unresolved doublet, which would be consistent with the calculated spectrum in reference 75.

Luminescence decay lifetimes were obtained by selectively exciting and monitoring specific lines for each site. The lifetime values reported for each site are the average of measurements recorded when monitoring different emission lines. Direct excitation of the $^5D_0$ level of the bulk material resulted in single-exponential lifetimes of 1.57, 0.78 and 0.82 ms, for sites A, B, and C, respectively.

Table 2-1 summarizes the lifetimes obtained from the decay transients of the bulk monoclinic 0.1% Eu^{3+}:Y_2O_3. The $^5D_1$ decay times for sites B and C were measured by monitoring $^5D_1 \rightarrow {}^7F_3$ emission in the 585-602 nm spectral range. These lifetimes were obtained from a single-exponential fit to the data. The $^5D_1$ decay times for sites B and C were 112 and 138 μs,

respectively. The directly excited $^5D_1$ emission of site A did not appear to be a single exponential but the signal was too weak to obtain a good fit. The $^5D_1$ decay time for site A was obtained by monitoring the $^5D_0$ emission after exciting the $^5D_1$ levels. Observations of transitions from $^5D_0$ after excitation of $^5D_1$ show an initial rise-time followed by an exponential decay. Fitting these transients to the exponential decay function $y = y_0 + A_1e^{-(x-x0)/\tau_1} + A_2e^{-(x-x0)/\tau_2}$, where τ_1 and τ_2 are the $^5D_0$ and $^5D_1$ lifetimes respectively, y_0 is the offset, $(x-x_0)$ is the decay, and A is the amplitude, produced a $^5D_0$ lifetime that was the same as that when measured directly and a $^5D_1$ lifetime of 71 μs for site A.

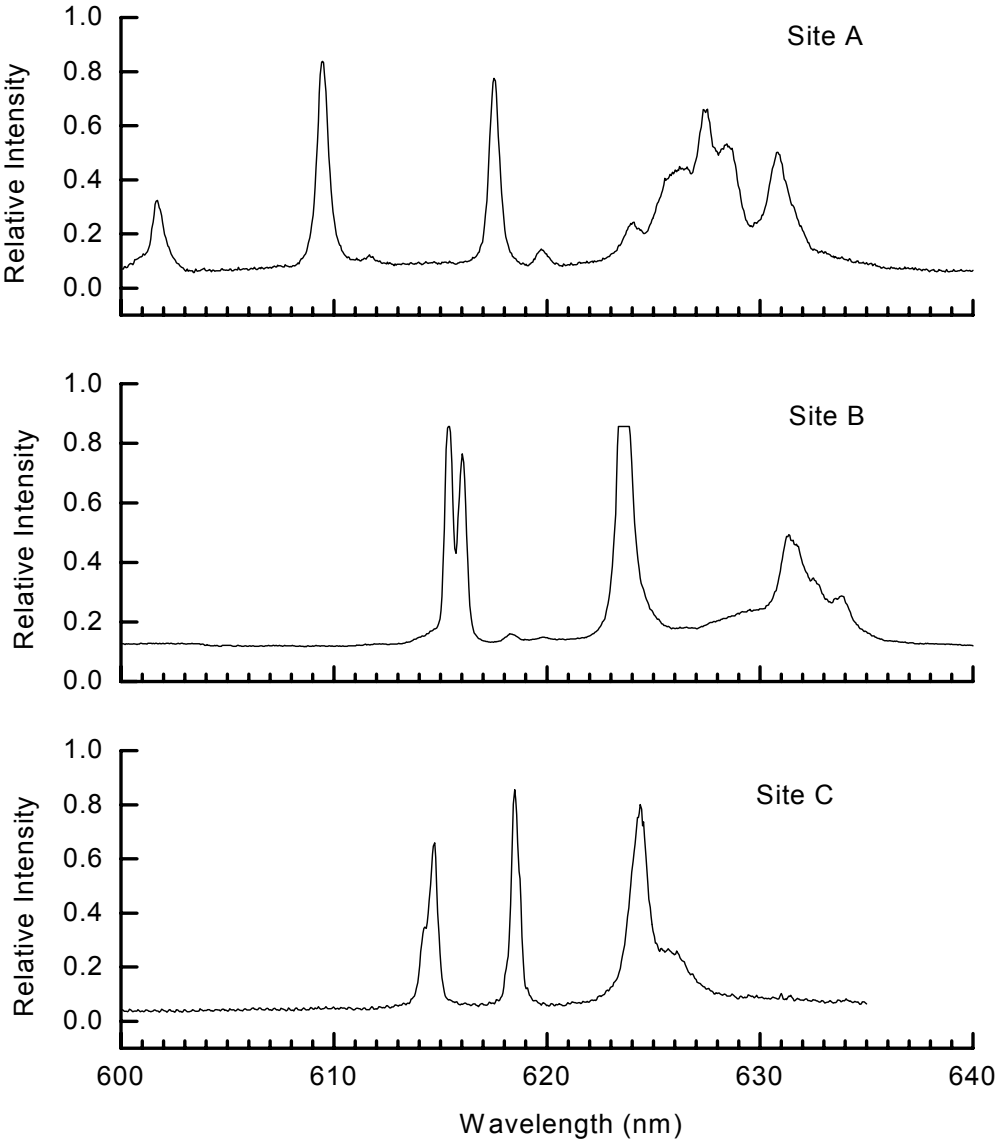

Figure 2-8. $^5D_0 \rightarrow {}^7F_2$ emission spectra of bulk monoclinic 0.1 mol % Eu^{3+}:Y_2O_3. The excitation wavelengths were 579.4, 582.7, and 582.9 nm for sites A, B, and C, respectively. The boxcar delay and gate widths were 1 and 150 μs, respectively, and the bandpass of the 1-m monochromator was 0.2 nm.

Table 2-1. Luminescence lifetimes of bulk monoclinic 0.1 mol % Eu^3:Y_2O_3 as determined by laser spectroscopy.

	Site A	Site B	Site C
$^5D_1$	71 ± 7 μs	112 ± 7 μs	138 ± 7 μs
$^5D_0$	1.57 ± 0.07 ms	0.78 ± 0.04 ms	0.82 ± 0.04 ms

2. D. Summary

These optical results on bulk monoclinic 0.1 mol % Eu^{3+}:Y_2O_3 provide reference spectra and excited-state lifetimes that allow evaluation of the optical properties of Eu^{3+}:Y_2O_3 nanocrystals. The anomalies of site A, such as the additional lines in the $^5D_0 \rightarrow {}^7F_2$ spectra, are attributed to intrinsic features of the monoclinic phase of Y_2O_3. For the work done with monoclinic Eu^{3+}:Gd_2O_3, additional lines in the $^5D_0 \rightarrow {}^7F_2$ spectra were assigned as vibronic sidebands[80].

The $^5D_0$ and $^5D_1$ fluorescence lifetimes of sites A, B, and C in the bulk material allow a direct comparison with the nanocrystalline lifetimes. Now that the fluorescence properties of bulk monoclinic Eu^{3+}:Y_2O_3 are known, the fluorescence dynamics of nanocrystalline Eu^{3+}:Y_2O_3 can be investigated as a function of variables such as particle size and annealing.

Chapter 3. Size Dependence of the Luminescence Spectra and Dynamics of 0.1 mol % Eu^{3+}:Y_2O_3 Nanocrystals

3. A. Experimental

3. A. 1. Sample Preparation

Nanocrystalline 0.1% Eu^{3+}:Y_2O_3 samples were prepared by a gas-phase-condensation technique [81,82] using CO_2-laser vaporization of pressed and sintered pellets of 0.1mol % Eu^{3+}:Y_2O_3. The starting material was prepared by pressing mixtures of pre-dried Eu_2O_3 (99.99%, Aldrich) and Y_2O_3 (99.99%, Aldrich) under 5000 psi. The pellets were sintered overnight in air in a platinum crucible at 1000 ^{0}C. After sintering, the pellets were placed on a rotating stage (one revolution takes approximately 8 minutes) in a vacuum chamber and the CO_2-laser was focused onto the pellet to a spot size of approximately 2 mm. The pellets were vaporized in a nitrogen atmosphere at pressures 400, 100, or 10 Torr, depending on the experiment. The nanocrystals were collected on a pyrex cold finger filled with 60 ^{0}C water, which kept the quenching temperature constant. The production rate was approximately 10 mg/hour. A schematic of the preparation chamber is shown in Figure 3-1.

3. A. 2. Powder X-ray Diffraction

Powder X-ray diffraction (XRD) results were obtained using a Scintag XDS-2000 diffractometer with Cu Kα radiation. The nanocrystals were placed in spectroscopic grade acetone and dispersed using a Branson 1510 Ultrasonicator for approximately fifteen minutes. After dispersion, the crystals were deposited onto a quartz plate with a Pasteur pipet and allowed to air dry for approximately five minutes. After drying, the quartz plate containing the dispersed nanocrystals was placed in the sample holder in the

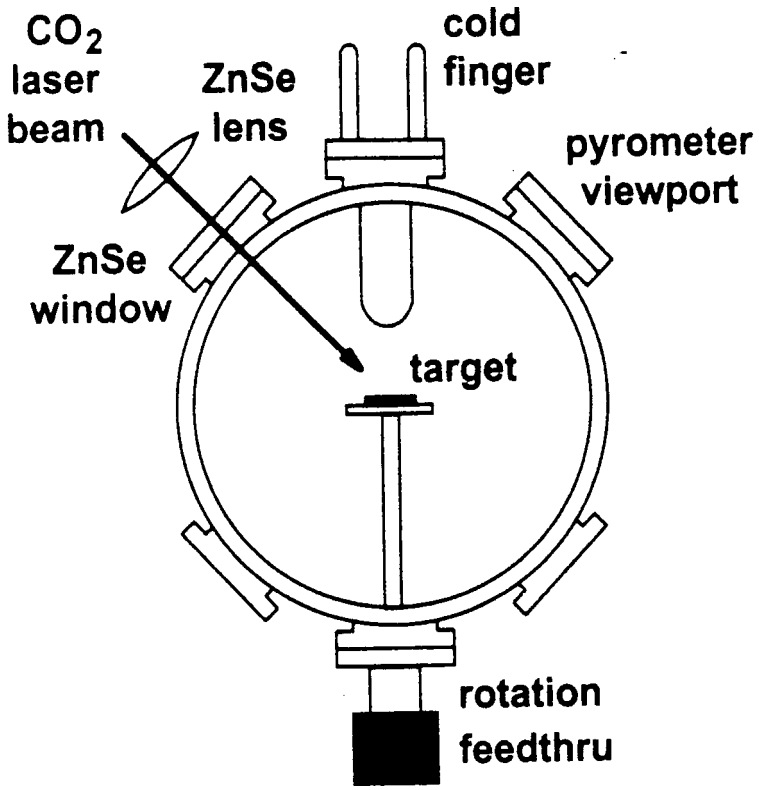

Figure 3-1. Schematic of vaporization chamber used for the preparation of nanocrystals. The interior of the chamber is filled with nitrogen.

diffractometer. The standard sample used for calibration of the diffractometer was Al_2O_3.

3. A. 3. Transmission Electron Microscopy

The nanocrystalline 0.1% Eu^{3+}:Y_2O_3 samples were prepared for transmission electron microscopy by dispersing the nanocrystals in spectroscopic grade acetone and sonicating with the Branson 1510 Ultrasonicator for fifteen minutes. After sonication, the dispersed crystals were placed on copper grids using a Pasteur pipet. The copper grids were individually loaded into a Phillips Transmission Electron Microscope (EM 420) for analysis. For each sample, a minimum of three micrographs was obtained by photographing three different regions on the grid to ensure randomization.

Particle size determinations were made by surveying the micrographs. For one particle size determination, a minimum of fifty particle diameters was measured. The resulting diameter measurements were used to produce a histogram, which indicated the dominant particle size diameter corresponding to a specific chamber pressure used in the preparation.

3. A. 4. Laser Spectroscopy of 0.1% Eu^{3+}:Y_2O_3 Nanocrystals with Diameters of 15 nm, 13 nm, and 7 nm

The laser spectroscopy experiments were performed by the method described in detail in Chapter 2.

3. B. Results and Discussion

3. B. 1. Characterization

The powder X-ray diffraction pattern of nanocrystalline 15-nm 0.1% Eu^{3+}:Y_2O_3 as shown in Figure 3-2 is essentially identical with respect to line positions, line widths, and relative intensities to the powder pattern of submicrometer monoclinic Y_2O_3 powder

prepared by thermal plasma processing with an average diameter of approximately 21 nm [12]. The diffraction lines of the nanocrystalline material are broadened due to the small particle size. Small crystals have relatively few lattice planes that contribute to the interference of the reflected X-rays. As a result, the widths of the diffraction lines increase when the particle size is reduced.

The photograph shown in Figure 3-3 and the histogram shown in Figure 3-4 illustrate the results of the transmission electron microscopy experiments that were performed on 0.1% Eu^{3+}:Y_2O_3 prepared using 400 Torr of nitrogen in the vaporization chamber. The particles were collected from all regions of the cold finger. The particle diameters ranged from 7 to 23 nm with a dominant particle diameter of 15 nm.

After the results from the 15-nm experiment were obtained, nanocrystals were prepared using the same pressure (400 Torr) but the nanocrystals were collected differently. The particles were collected at specific locations on the cold finger: 6.5 cm from the target and 3.0 cm from the target. The histograms, shown in Figure 3-5, indicate that collecting crystals at different distances from the target to the cold finger gave different results. The nanocrystals that were collected 6.5 cm from the target had a larger distribution range (12-24 nm) and a larger dominant particle diameter (18 nm). The nanocrystals that were collected 3.0 cm from the target had a distribution range of 12-20 nm and a dominant particle diameter of 15. These results are significant because they allow for the production of nanocrystals with different particle sizes.

In Table 3-1, the dominant particle diameters, range of particle diameters, pressures of nitrogen in Torr, and distances from the cold finger summarize the additional results

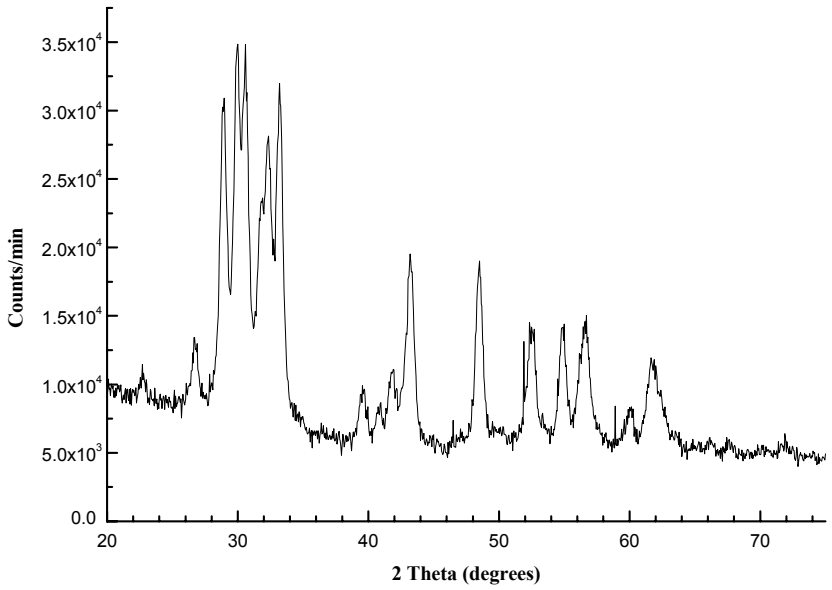

Figure 3-2 . Powder X-ray diffraction pattern of 15-nm monoclinic 0.1 mol % Eu^{3+}:Y_2O_3 prepared by laser-vaporization-gas-phase condensation method. The sample was prepared using 400 Torr nitrogen in the vaporization chamber. The crystals were collected from all regions on the cold finger.

obtained by the preparation of 0.1 mol % Eu^{3+}:Y_2O_3 by the laser-vaporization-gas-phase condensation method. The results show that both chamber pressure and the distance from the target to the cold finger have an effect on the particle diameter distribution.
The reproducibility of the synthesis was tested by making multiple samples, performing TEM experiments, and plotting a histogram of the data. The dominant particle diameters never varied more than ± 1 nm when the preparation conditions were the same for repeat experiments.

3. B. 2. Laser Spectroscopy

Figure 3-6 shows the $^7F_0 \rightarrow {}^5D_0$ broadband excitation spectra of bulk, 15-nm, 13-nm, and 7-nm 0.1% Eu^{3+}:Y_2O_3 recorded with a 0.25-m monochromator set at 614 nm. The spectra were recorded by the author with the exception of the 7-nm sample, which was recorded by Dr. Huabiao Yuan. The spectrum of the bulk material shows sharp lines at 579.4, 582.7, and 582.8 nm for sites A, B, and C, respectively.

When the spectral results are compared, several significant changes are evident in the broadband excitation spectra as the particle size decreased. First, the widths of the three sharp monoclinic lines broaden as the particle size is decreased. The line width of the site A line is 0.3 nm for the 15-nm sample, 0.5 nm for the 13-nm sample, and 0.8 nm for the 7-nm sample. Line width measurements for sites B and C were not obtained since the lines for sites B and C merged into a single peak as the particle size was decreased. The total line width contains contributions from the inhomogeneous line width, which is caused by strains and defects in the lattice[79]. The line width measurements for site A indicate that the increase in the surface volume does have an effect on the line widths in

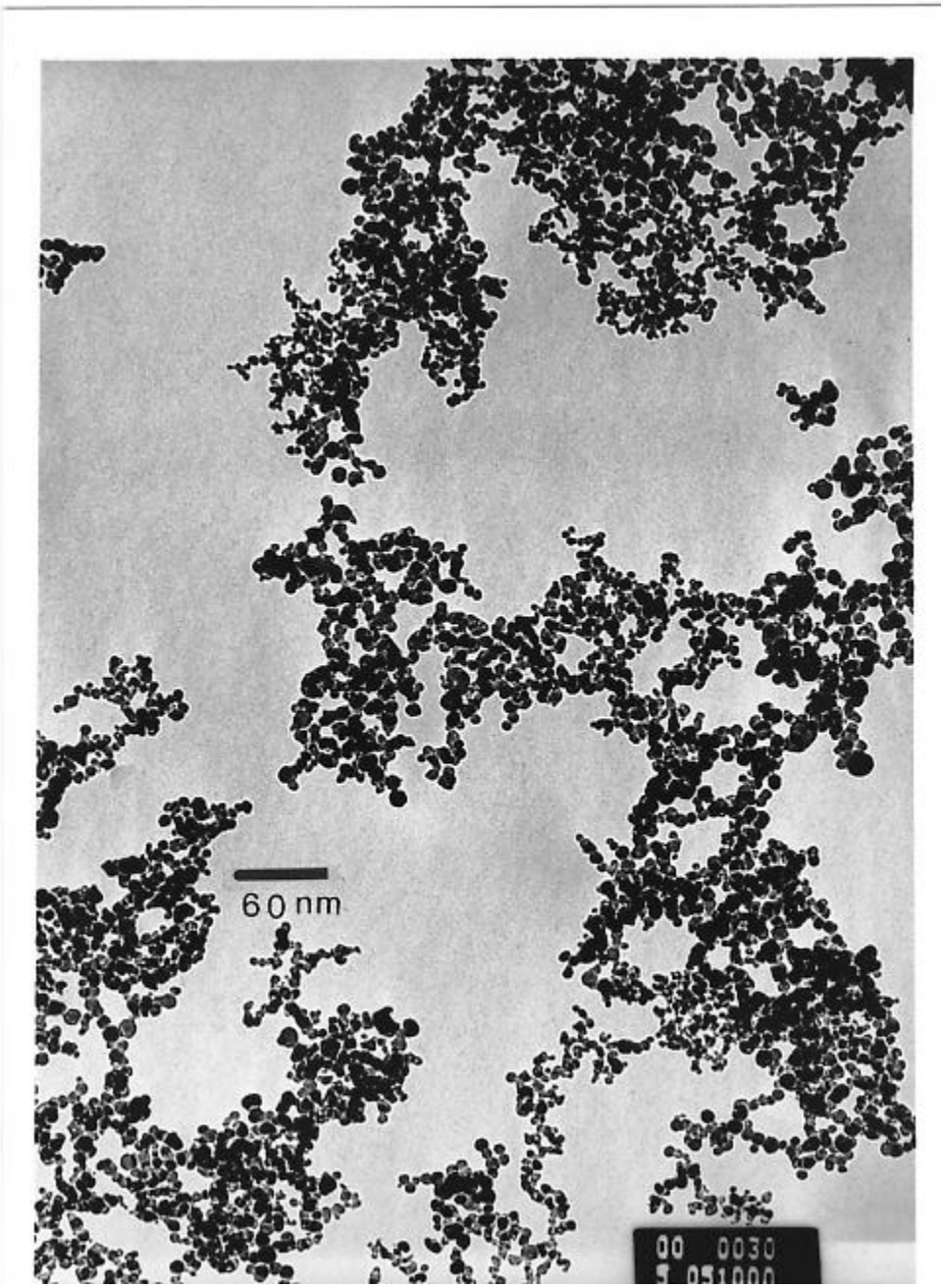

Figure 3-3. Photograph generated from the TEM micrograph of 0.1 mol % Eu^{3+}:Y_2O_3 prepared with 400 Torr nitrogen in the vaporization chamber. The nanocrystals were collected from all regions of the cold finger.

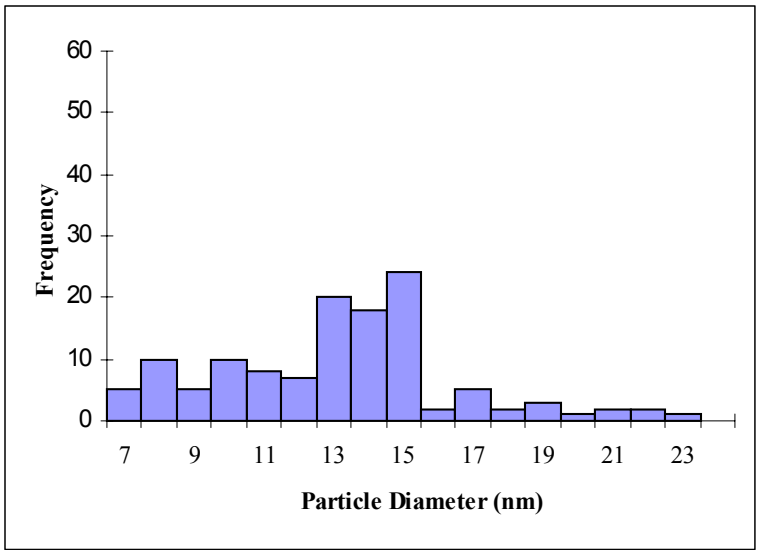

Figure 3-4. Histogram of 15-nm 0.1 mol % Eu^{3+}:Y_2O_3 prepared using 400 Torr nitrogen in the vaporization chamber. The crystals were collected from all regions of the cold finger.

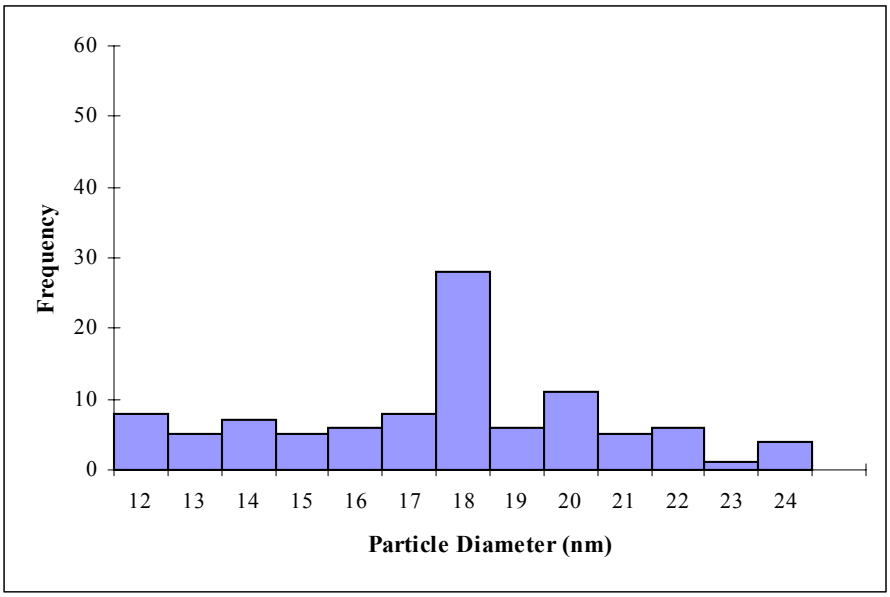

(a)

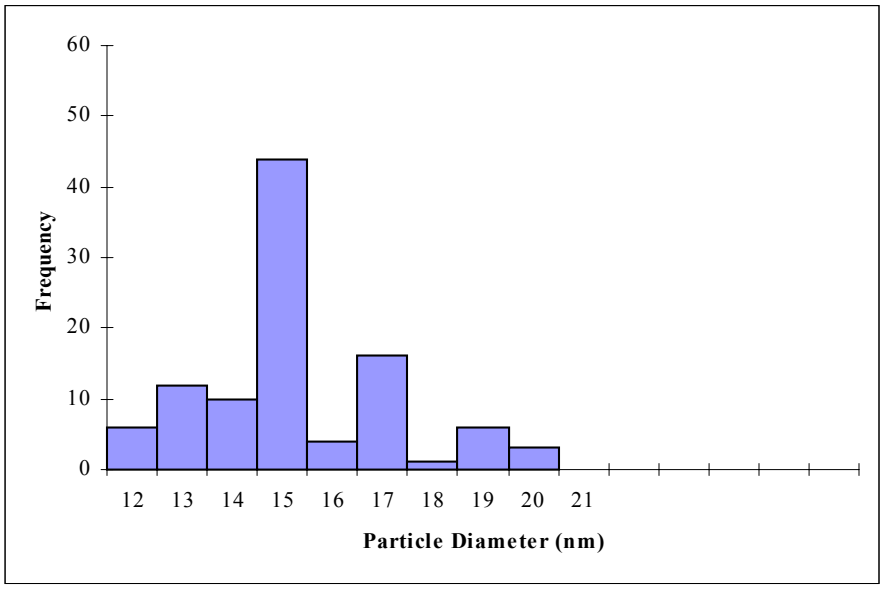

(b)

Figure 3-5. Histograms resulting from the TEM of 0.1 mol % Eu^{3+}:Y_2O_3 nanocrystals prepared with 400 Torr N_2. In (a), the particles were collected 6.5 cm from the target; In (b), the particles were collected 3.0 cm from the target.

Table 3-1. Results from the laser-vaporization-gas-phase condensation of Eu^{3+}:Y_2O_3 with a pre-vaporization dopant concentration of 0.1 mol %. The reproducibility of the results is ± 1 nm.

Nitrogen Pressure (Torr)	Distance from target to cold finger (cm)	Dominant Particle Diameter (nm)	Particle Distribution Range (nm)
400	6.5	18	12-24
400	3.0	15	12-20
400	2.0	13	8-22
100	3.0	9	7-13
100	2.0	7	4-14
10	3.0	4	3-6

the nanocrystals and is attributed to the fact that more of the signal being detected in the smaller particles is coming from atoms on the surface of the nanocrystals. Atoms on the surface can be displaced from their normal lattice positions, creating more disorder. The current consensus in the literature regarding spectral line broadening in nanocrystalline ceramics is consistent with these results[26,83].

Figure 3-7 shows the correlation between surface area and particle size. The volume fraction of surface atoms was calculated by the following equation:

$$\text{Volume fraction of surface atoms} = \{[\, 4/3\pi r^3 - 4/3\pi(r-\delta)^3] / 4/3\pi r^3\} \times 100$$

where δ is the assumed surface thickness of 0.5 nm and r is the particle radius. The assumption of the surface thickness of 0.5 nm is consistent with the literature.

The second trend that was observed with decreasing particle size is the appearance of additional phases or sites. The spectrum of the 13-nm sample shows the appearance of a peak at 580.6 nm. As the particle size is reduced to 7 nm, the intensity of the peak at 580.6 nm increases. This peak corresponds to the C_2 site in cubic-phase Y_2O_3 [69]. In addition to the presence of the cubic phase, a broad band that overlaps with the site A excitation line was observed. This broad band is most obvious in the spectra of the 7-nm particles, but it is also present in the 15- and 13-nm samples at a much weaker intensity and is attributed to the formation of an amorphous phase, resulting from the low pressure of nitrogen used in the preparation. This conclusion is based on the similar results observed in the preparation of nm-Gd powder by the evaporation condensation of Gd atoms in an inert gas atmosphere[84] and the preparation of nm-Ti powder by condensation with inert gas[85]. Shao[84] reported that the XRD results obtained for the gadolinium powder show the formation of an amorphous phase, which was attributed to low inert gas

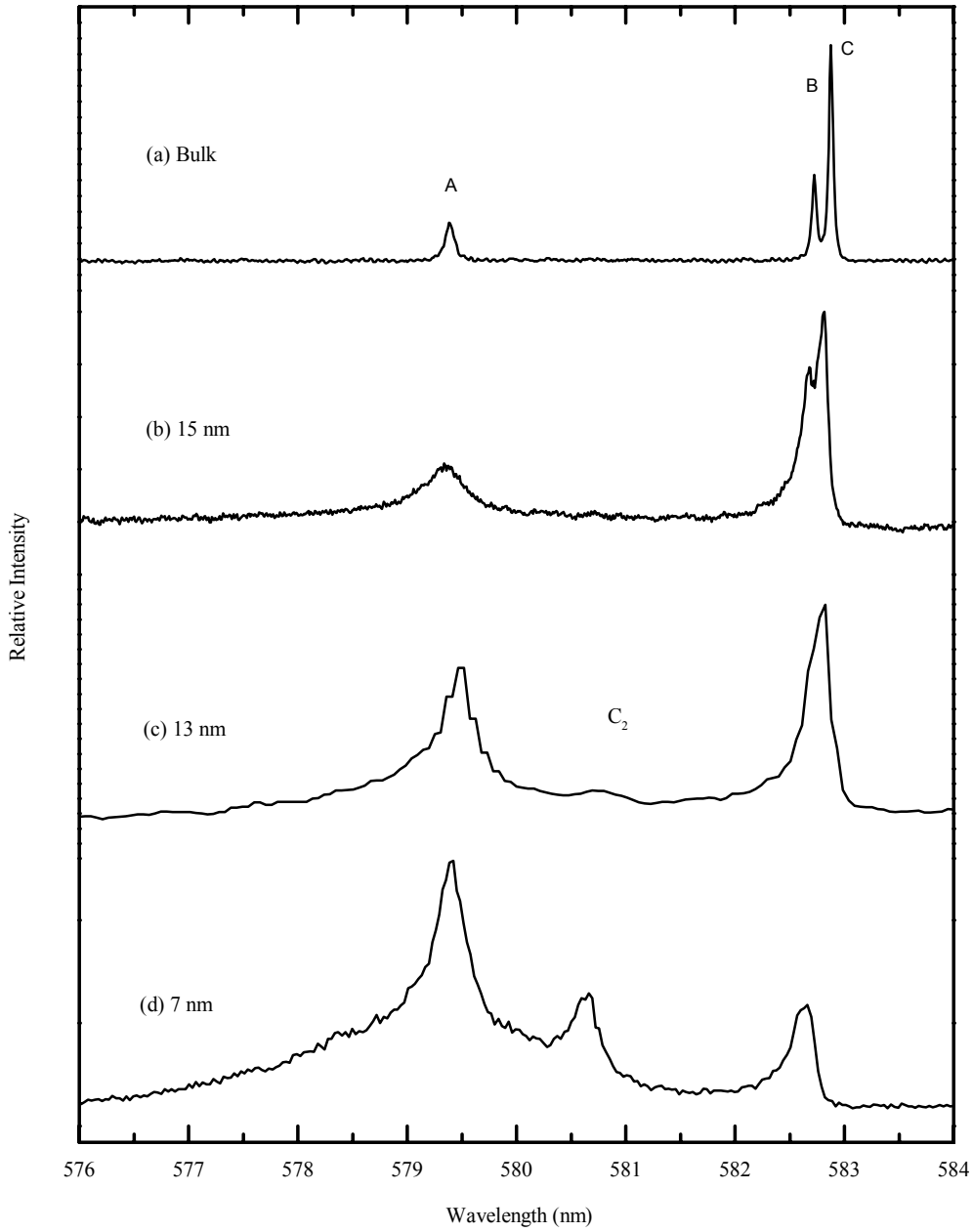

Figure 3-6. $^7F_0 \rightarrow {}^5D_0$ excitation spectra of 0.1% Eu^{3+}:Y_2O_3 at 13 K. The spectra were recorded with a 0.25-m monochromator set at 614 nm. The delay and gate for the spectra were 20 and 150 μs, respectively.

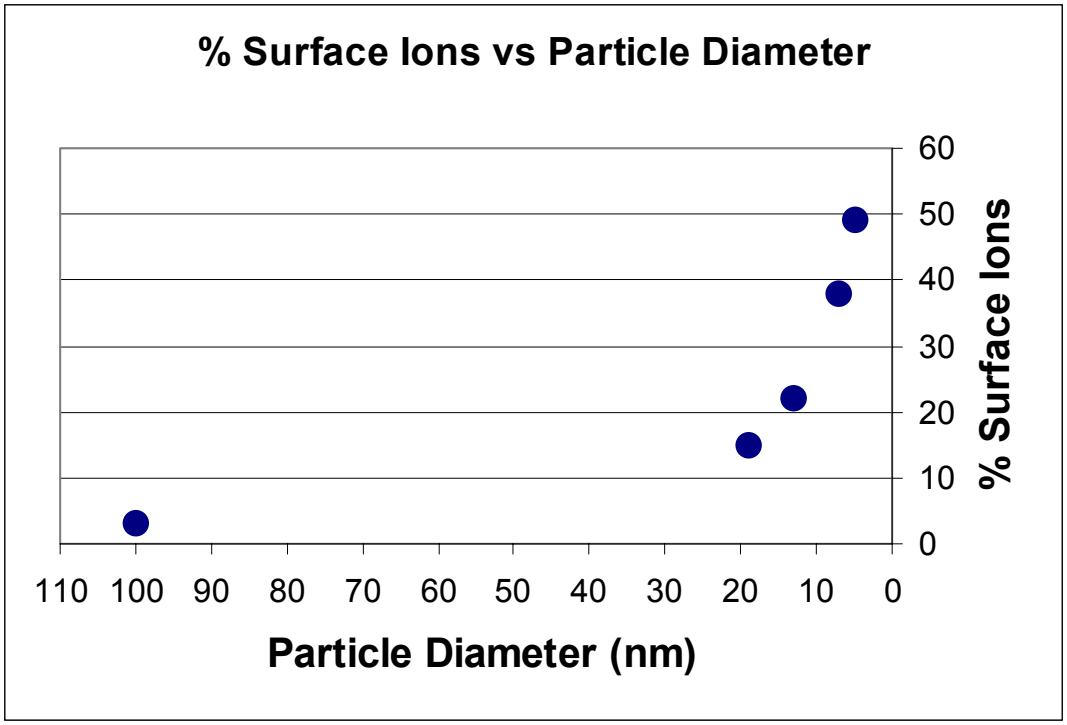

Figure 3-7. Volume fraction of ions on the surface as a function of particle diameter.

pressure (2 Torr). Both groups reported that the particle size of the samples decreased with decreased inert gas pressure.

Figure 3-8 shows the $^5D_0$ site-selective luminescence spectra for site A, which illustrate several trends for the nanocrystalline materials. Excitation of site A shows the sharp site A lines as seen in the bulk materials, but also broad features and the emission lines of sites B and C (614-616 nm). Sites B and C lines were observed in all of the nanocrystalline samples for site A excitation. Since the Eu concentration is low (0.1 mol %), site-to-site energy transfer is not expected. The true concentration in the nanocrystals might be higher than in the starting material or there might be some segregation of the dopant ion in the nanocrystals creating a higher local concentration that allows for energy transfer. The spectrum for the 15-nm sample shows lower signal-to-noise due to the smaller bandpass used with the 1-m monochromator.

Figure 3-9 shows the site-selective luminescence spectra for site B that were obtained by exciting $^5D_0$. The site B emission spectra contain peaks at the wavelengths obtained for the bulk material but additional lines at 614.7 and 618.6 nm emerge in the 13-nm sample. These additional lines are due to site C. The broad band that appears at 614 nm in the site A spectrum also appears in the site B spectra, although it is much less intense. With decreasing particle size, the intensity of this broad feature gets stronger, showing the same trend as the broad band in the excitation spectra (Figure 3-6).

In the site C luminescence spectra, shown in Figure 3-10, the site C lines predominate while site B lines appear as shoulders on the site C lines. The broad band at 614 nm that appears in the site A and B spectra is present in the site C spectra as well. As seen in Figure 3-6, the $^5D_0$ excitation lines for sites B and C are broader than in the bulk material

and for the smallest particles merge to appear as one peak. This spectral overlap of sites B and C explains the co-existence of emission lines from both sites B and C in the emission spectra. Some selectivity in exciting sites B and C is possible by exciting wavelengths on the sides of the broadened excitation line. As Figures 3-9 and 10 show, doing so affects the relative intensity of the site B and C emission lines. Table 3-2 summarizes the luminescence data that were obtained. Table 3-3 lists the $^5D_0$ decay times obtained by selectively exciting and monitoring the sharp lines in the bulk and nanocrystalline materials. The decay transients for the bulk and 15-nm samples were single exponential and the reported decay times were obtained from single-exponential fits to the decay curves. The decay transients for the 13-nm and 7-nm samples were not single exponential and the decay times reported for these samples were obtained by fitting the linear portions of log plots of the transients (4-10 ms for the 13-nm sample and 5-15 ms for the 7-nm sample). The multi-exponential decay suggests there is some quenching by surface defects in the 13 and 7-nm samples. Statistical analysis of the lifetime data is not included in this thesis because of the research regarding the lifetimes of nanocrystals as discussed in the next paragraph.

The dependence of the fluorescence lifetimes of Eu^{3+}:Y_2O_3 nanoparticles on the surrounding medium was investigated by Meltzer, Feofilov, Tissue, and Yuan [86]. They reported that the radiative lifetimes of the excited states of impurity ions strongly depend on the effective refractive index of the media surrounding the nanoparticles and the substance that fills the space around them. They found that placing the nanoparticles in a material with a greater index of refraction resulted in a reduced lifetime. For “dry”

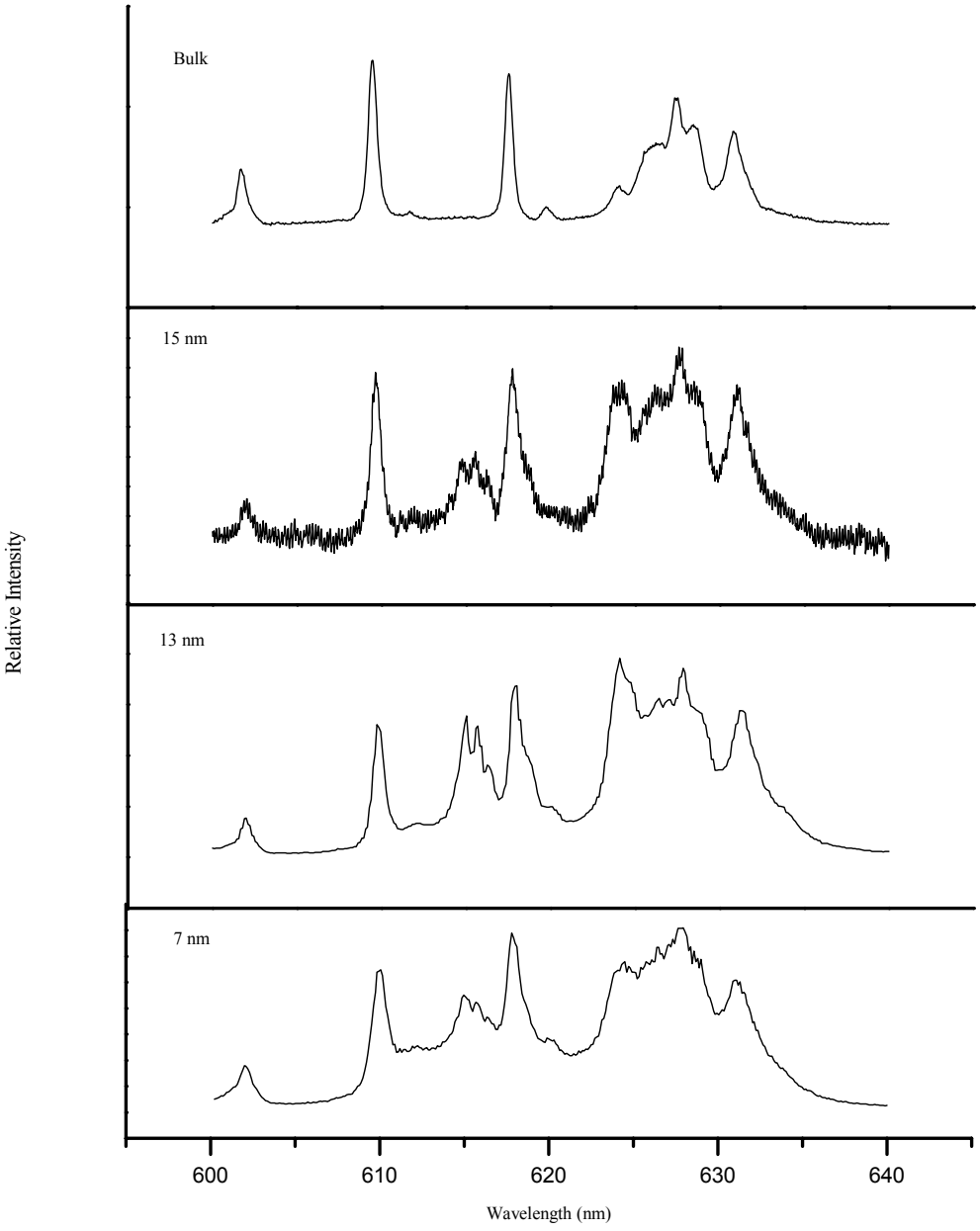

Figure 3-8. $^5D_0 \rightarrow {}^7F_2$ Site A luminescence spectra of bulk (top) and nanocrystalline 0.1 % Eu^{3+}:Y_2O_3 at 13 K. The excitation wavelength for all spectra was 579.89 nm. The bulk and15-nm samples were recorded with a 1-m monochromator with a bandpass of 0.4 nm. The other spectra were recorded with a bandpass of 0.6 nm.

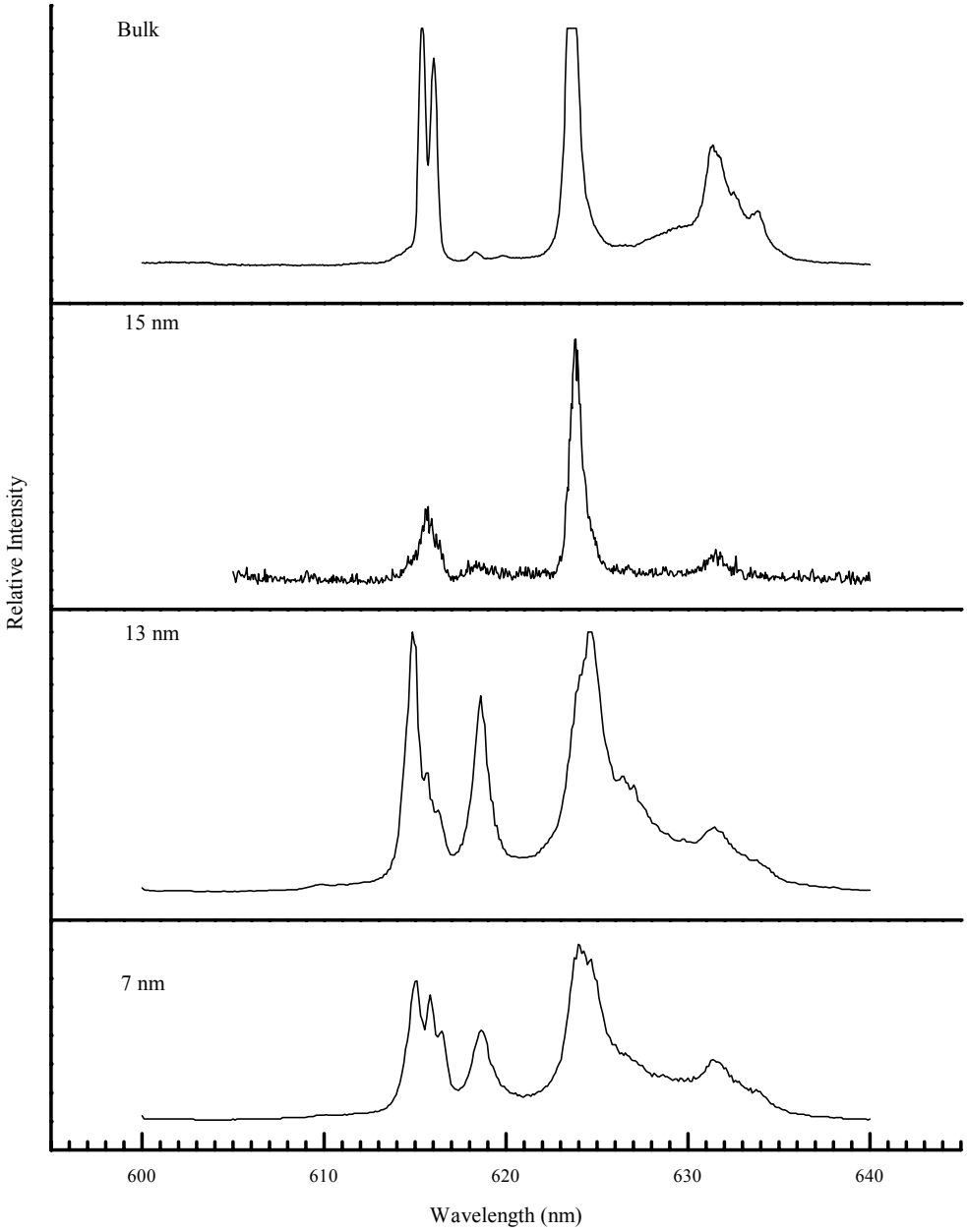

Figure 3-9. $^5D_0 \rightarrow {}^7F_2$ Site B luminescence spectra of 0.1 % Eu^{3+}:Y_2O_3 at 13 K. The spectra were recorded with a 1-m monochromator with a 0.08 nm bandpass for the 13-and 7-nm samples and 0.16 bandpass for the bulk and 15-nm. The excitation wavelength for all spectra was 582.72 nm.

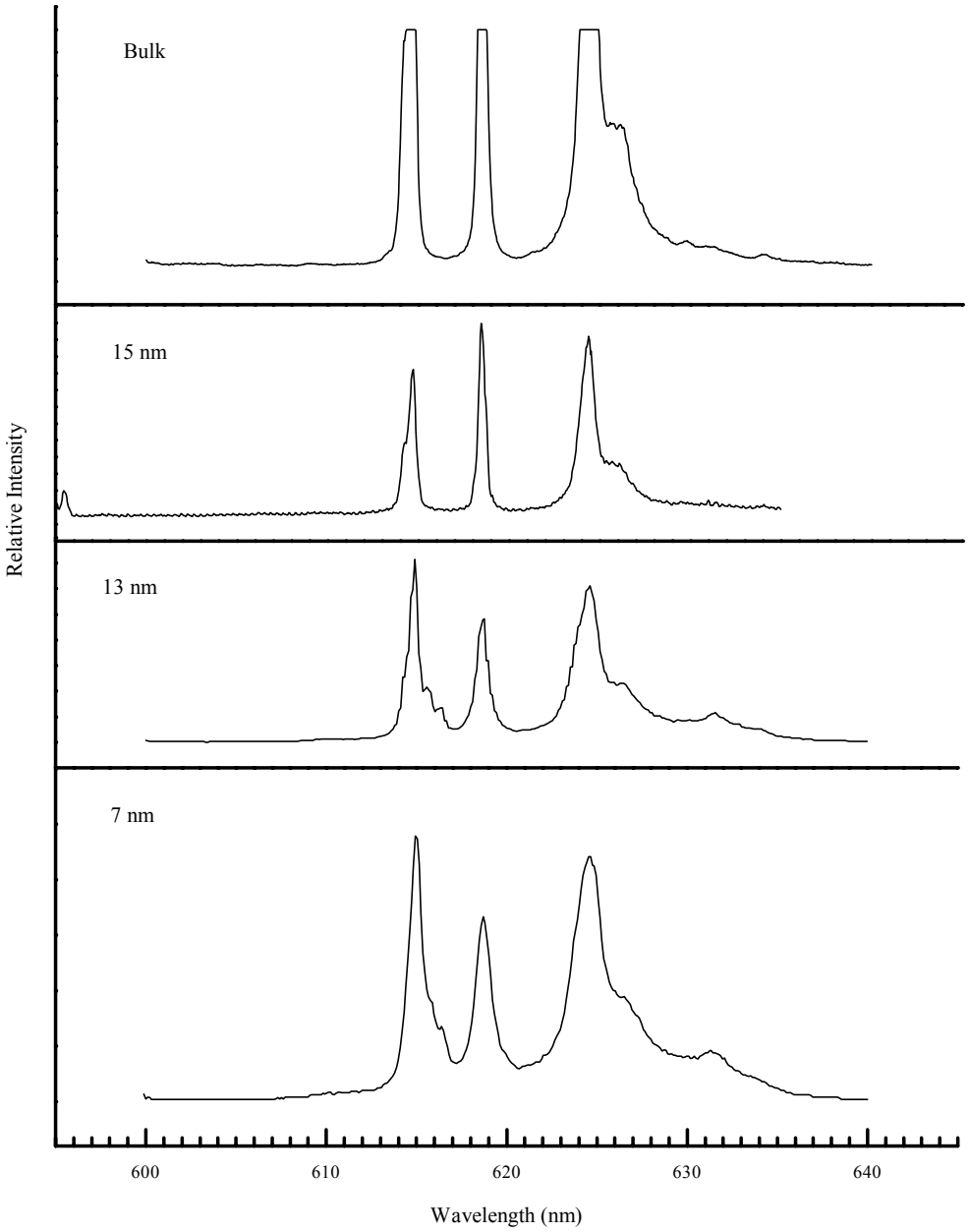

Figure 3-10 . $^5D_0 \rightarrow {}^7F_2$ Site C luminescence spectra of 0.1% Eu^{3+}:Y_2O_3 bulk (top) and nanocrystals at 13 K. The spectra were recorded with a 1-m monochromator with a 0.08 nm bandpass for the two smaller samples and 0.16 nm for the two larger samples. The excitation wavelength for all spectra was 582.87 nm.

Table 3-2. $^5D_0 \rightarrow {}^7F_2$ luminescence peak assignments for sites A, B, and C in 0.1 mol % Eu^{3+}:Y_2O_3. Peaks that emerged with decreasing particle size are shown in bold.

	Site A peak assignments (nm)	Site B peak assignments (nm	Site C peak assignments (nm)
Bulk	601.7, 609.4, 617.7, 624.1, 627.6, 630.9	615.5, 616.6, 623.5, 631.5	614.7, 618.6, 624.3
15 nm	601.7, 609.6, **615.5**, 617.7, 624.1, 627.6, 631.0	616.6, 623.6, 631.5	614.7, 618.6, 624.3
13 nm	601.7, 609.7, 615.5, 617.7, 624.1, 627.8, 631.0	614.7, 616.6, **618.6**, 624.7, 631.5	614.9, 618.7, 624.6
7 nm	602.0, 609.8, 615.5, 617.7, 624.1, 627.8, 631.0	615.5, 615.8, 618.6, 624.1, 631.5	615.0, 618.7, 624.6

nanocrystalline samples (those not placed in an immersion liquid), the radiative lifetimes depend on the degree to which the sample is compacted in a sample holder. Since the degree of compacting is not standardized, the lifetime values that were obtained and reported in this thesis must be considered an estimate.

Table 3-3. **Estimation of $^5D_0$ decay times of 0.1% Eu^{3+}:Y_2O_3 at 13 K. The reported values are the average values that were obtained by monitoring each line in the emission spectra.**

Sample	Particle Range (nm)	Site A (ms)	Site B (ms)	Site C (ms)
Bulk		1.6	0.8	0.8
15-nm	7-23	1.8	1.3	1.3
13-nm	8-17	4.2	2.8	3.2

3. C. Summary of Size Dependence Work

The excitation and luminescence spectra of the nanocrystalline Eu^{3+}:Y_2O_3 show three phases: (1) the sharp lines of the monoclinic Y_2O_3, which dominate in the larger nanoparticles; (2) the C_2 site of the cubic phase, which appears in the smaller particles; and (3) broad bands due to a disordered phase that increases with intensity as the particle size decreases. The broadening of the sharp spectral lines with decreasing particle size is attributed to increased disorder induced by the lattice distortion. However, the observation of distinct spectral lines from the monoclinic phase confirms the presence of some crystalline phase for all of the particle sizes.

The formation of the nanoparticles in the monoclinic phase has been attributed to the Gibbs-Thomson effect [19,76], which is a pressure created by surface tension However, as the particle size decreases to 7 nm, cubic-phase Y_2O_3 forms and a disordered phase associated with broad bands dramatically increases its dominance in the spectra (Fig. 3-8). These results indicate that the Gibbs-Thompson effect is not controlling the crystal structure in the smallest particles because with the reduced particle diameters the surface tension should increase, therefore creating a larger pressure effect. The reappearance of the cubic phase in the small particles might indicate that the surface becomes less liquid-like, minimizing the surface tension. With the surface tension at a minimum, the particles form in the cubic phase like the micrometer-structured materials.

The presence of the broad band that increases dramatically as the particle size decreases is attributed to an amorphous phase that results from the disorder created during the vaporization-condensation process. Recall that the small particle diameters result from low pressure of nitrogen gas in the vaporization chamber. As the particles are

vaporized, they undergo collisions with the inert gas molecules before condensing onto the cold finger. If fewer gas molecules are present, then there are fewer collisions which results in faster condensation times. Many oxides will form amorphous phases when heated and cooled quickly, since there is not sufficient "time" for the atoms to arrange themselves in an ordered array. This phenomenon is observed in bulk SiO_2, for example. Crystalline SiO_2 (quartz) exists in a highly ordered cubic crystal structure but upon heating and cooling forms an amorphous phase material (glass). Therefore, the presence of an amorphous phase increases its dominance in the optical spectra of the nanomaterials as the chamber pressure decreases.

The particle size dependence on the luminescence spectra of Eu^{3+}:Y_2O_3 revealed structural changes, specifically phase transformations that occur in these materials. To learn more about the structure of nanocrystalline materials, a study was initiated to prepare and characterize nanocrystalline Eu^{3+}:CaO, since this system contains a host ion with a different charge than the dopant ion. When there is a charge mismatch, defects occur to maintain overall charge neutrality[3]. Since the defect chemistry has not been studied extensively in nanocrystalline systems, experiments were designed to produce and characterize nanocrystalline Eu^{3+}:CaO with the eventual goal of determining the dopant distribution (defect chemistry) in these materials.

Chapter 4. Preparation, Characterization, and Broad-Band Excitation Spectra of Nanocrystalline Eu^{3+}:CaO

4. A. Introduction

Calcium oxide exists in a face-centered cubic crystal structure[3] and is prepared from heating calcium carbonate, which results in decomposition into calcium oxide and carbon dioxide. Calcium oxide is stable at high temperatures but its surface can be attacked by water and carbon dioxide at room temperature [70]. The resulting reactions are: $CaO\ (s) + CO_2\ (g) \rightarrow CaCO_3\ (s)$ and $CaO\ (s) + H_2O\ (g) \rightarrow Ca(OH)_2\ (s)$. Both calcium carbonate and calcium hydroxide are amorphous materials under these synthesis conditions.

The europium ion has been used to probe the structure and defect chemistry of bulk calcium oxide[70] but the dopant distribution (defect chemistry) in nanocrystalline calcium oxide had not been investigated prior to the work presented in this chapter. Since the laser spectroscopy of bulk Eu^{3+}:CaO has been published, the bulk material will serve as a baseline for studying the dopant distribution in nanocrystalline Eu^{3+}:CaO.

4. B. Experimental

Since Ca^{2+} and Eu^{3+} have greater relative differences in ionic radii than Y_2O_3 and Eu_2O_3, it was determined that the method of preparing the bulk Eu^{3+}:CaO, which is the precursor for the nanocrystalline material, would be altered from the method described previously for the preparation of bulk Eu^{3+}:Y_2O_3. The ionic radius of the Ca^{2+} ion is 114 pm, the ionic radius of the Eu^{3+} ion is 108 pm, and the ionic radius of the Y^{3+} ion is 104 pm[3].

Bulk Eu^{3+}:CaO was prepared by the method described by Porter and Wright [70]. The major difference between the preparation of the calcium and yttrium oxides doped with

europium is the addition of the dopant. In the yttrium oxide system, there is no charge difference in the host and dopant atoms, and the dopant is added as europium oxide and dry-mixed in a mill for fifteen minutes. After the dry-mix step, the materials are sintered in a furnace overnight at 1100 ^{0}C to increase the homogeneous distribution of the dopant within the host lattice. It is conventional in the literature to use a sintering temperature of 1000 ^{0}C or greater when sintering bulk materials for the preparation of nanocrystals by gas phase condesation[1,21].

To prepare low concentration samples accurately, the dopant is added by dissolving europium oxide in 5% nitric acid. The acid containing the dopant is then added to the calcium oxide and heated to evaporation. As with all nanocrystalline materials, the compound is sintered overnight at a high temperature (in this case, 1100 ^{0}C) to insure a homogeneous distribution of the dopant within the lattice. For sintering, a platinum crucible is used to prevent the reaction of the crucible with the materials. Separate crucibles are used for different materials to reduce the chance of contamination during the sintering process.

For the evaporation step, 5 % nitric acid and deionized water are used for cleaning the glassware to prevent contamination. The stainless steel die set that was used for pressing pellets of the bulk material was cleaned with 5 % nitric acid, followed by a rinse with deionized water, which was followed by a rinse with acetone after every press.

Following the preparation of the bulk material, the nanocrystals were formed by the laser-vaporization, gas-condensation method as described in detail in chapter 3. The chamber atmosphere was nitrogen gas at 400 Torr and the cold finger temperature was

approximately 60 ^{0}C. The nanocrystals were scraped from the bottom of the cold finger and placed under vacuum to minimize the reaction of the surface of the nanocrystals with water and carbon dioxide.

TEM was used to determine the particle size of the nanocrystals. After the preparation of the nanocrystalline Eu^{3+}:CaO, the nanocrystals were dispersed in spectroscopic-grade acetone using a Branson 1510 Ultrasonicator. Following the sonication, the dispersed crystals were placed on a copper grid for analysis. Transmission electron microscopy was performed using a Phillips 420 electron microscope and the resulting micrographs were used to survey the particle size range and morphology of the nanocrystals. The dominant particle size and range were determined by measuring the diameters of the individual particle images with calipers. The term "dominant particle size" is used instead of "average particle size" because the calculated average particle size is not necessarily representative of the true nature of the sample. In fact, on occasion, the average particle size appears with a low frequency in the histogram plot. Therefore, plotting a histogram of the data, obtained from a survey of micrographs, gives a more accurate representation of the majority of the particles being studied.

Laser spectroscopy experiments were conducted as described in detail in Chapter 2.

4. C. Results

Laser-induced fluorescence was visually observed for the as-prepared nanocrystalline Eu^{3+}:CaO material (with a pre-vaporization concentration of 0.1 mol % Eu^{3+}) by placing a red filter in front of the sample. The sample fluoresced strongly and was easily visible when the dye laser was set to 528.9 nm. The sample temperature was approximately 13 K during the experiment.

The $^7F_0 \rightarrow {}^5D_1$ excitation spectrum of the nanocrystalline sample is shown in Figure 4-1. The excitation spectrum was obtained by scanning the dye laser from 524-530 nm and monitoring fluorescence from all sites with a 0.25-meter monochromator with a 6-nm bandpass. The large bandpass of the monochromator allows for the collection of the broadband excitation spectrum so that all sites are shown. The most obvious feature in the spectrum is the broad peak centered at 526.4 nm. This wavelength corresponds to the monoclinic Eu_2O_3 phase [1]. The presence of this peak probably indicates that Eu_2O_3 was selectively vaporized during the laser-vaporization, gas-phase condensation process. The presence of this phase was not desirable since a study of the dopant distribution was planned. To try to eliminate the Eu_2O_3 phase, experiments were performed in which the dopant ion (dissolved in nitric acid) was added *after* the laser-vaporization-gas-phase condensation of nanocrystalline CaO.

A series of experiments proved, however, that this was not feasible. The nanocrystals would dissolve upon addition of the nitric acid solution containing the dopant. When the nitric acid concentration was reduced, then the dopant was not sufficiently dissolved. After these experiments were completed, it was determined that the materials would be made as before, which involved adding the dopant prior to vaporization.

To try to eliminate the monoclinic europium oxide phase, as observed in the spectrum shown in Figure 4-1, the experimental conditions were altered in two ways: (1) the pellets were made thicker and (2) higher laser powers were used for vaporization of the pellets. Since CaO has a higher melting point (2572 ^{0}C) than Eu_2O_3 (2350 ^{0}C), a higher laser output was used in an attempt to avoid selective vaporization of the europium oxide. The pellets were made thicker to insure greater stability during the vaporization process since

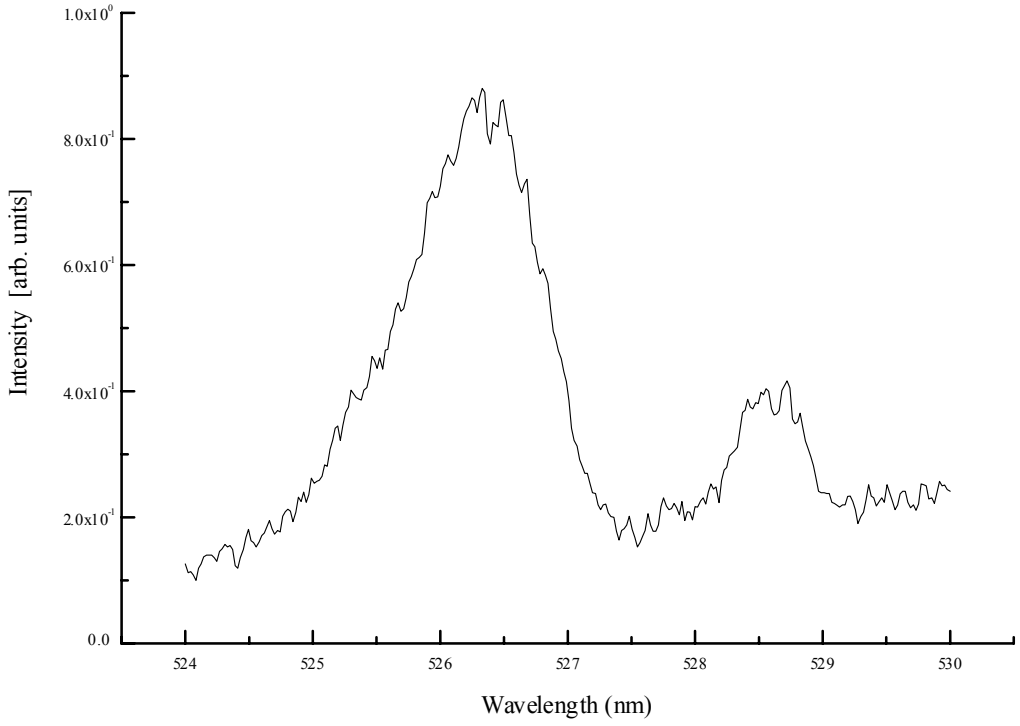

Figure 4-1. $^7F_0 \rightarrow {}^5D_1$ excitation spectrum of 0.1 mol % Eu^{3+}:CaO using a 0.25-m monochromator set at 614 nm. The delay and gate were 1 and 150 μs, respectively. The scan rate was 0.200 Angstroms/sec.

one of the effects of laser vaporization is frequently a fractured pellet. Pellet fracturing is undesirable during the experiment because the experiment has to be stopped and a new pellet has to be loaded onto the stage.

The spectrum shown in Figure 4-2 shows the broadband excitation spectrum of Eu^{3+}:CaO that was obtained after making the alterations described in the preceding paragraph. The laser output was 25 Watts and the pellet thickness was 12.7 mm. The most obvious features in this spectrum are the peaks centered at 528.3 and 528.8 nm. These wavelengths correspond to the values obtained by Porter and Wright for the bulk Eu^{3+}:CaO [70]. Unfortunately, the broad peak centered at 526.4 nm was not eliminated completely. Therefore, the experimental conditions were again altered with the hope of eliminating the europium oxide phase. The laser energy was increased to 30 Watts and the spectrum shown Figure 4-3 was obtained.

The spectrum that is shown in Figure 4-3 agrees with the spectrum published by Porter and Wright for the bulk Eu^{3+}:CaO sample[70]. Porter and Wright's $^7F_0 \rightarrow {}^5D_1$ broad band excitation spectrum showed absorption lines at 527.4 528.3, 528.5, 528.8, and 528.9 nm. The only difference in the two spectra is that the lines are broadened in the nanocrystalline spectrum. Since more of the signal being detected in the nanocrystalline sample is coming from atoms on the surface, rather than the interior, the line broadening is most likely due to surface atoms that are displaced from their lattice positions.

Figure 4-4 shows the TEM micrograph of as-prepared nanocrystalline Eu^{3+}:CaO with a pre-vaporization concentration of 0.1 mol % of dopant . The morphology of the Eu^{3+}:CaO nanocrystals was similar to that of the Eu^{3+}:Y_2O_3 nanocrystals. When the micrograph negative is placed upon a light box for viewing, the particles have well-

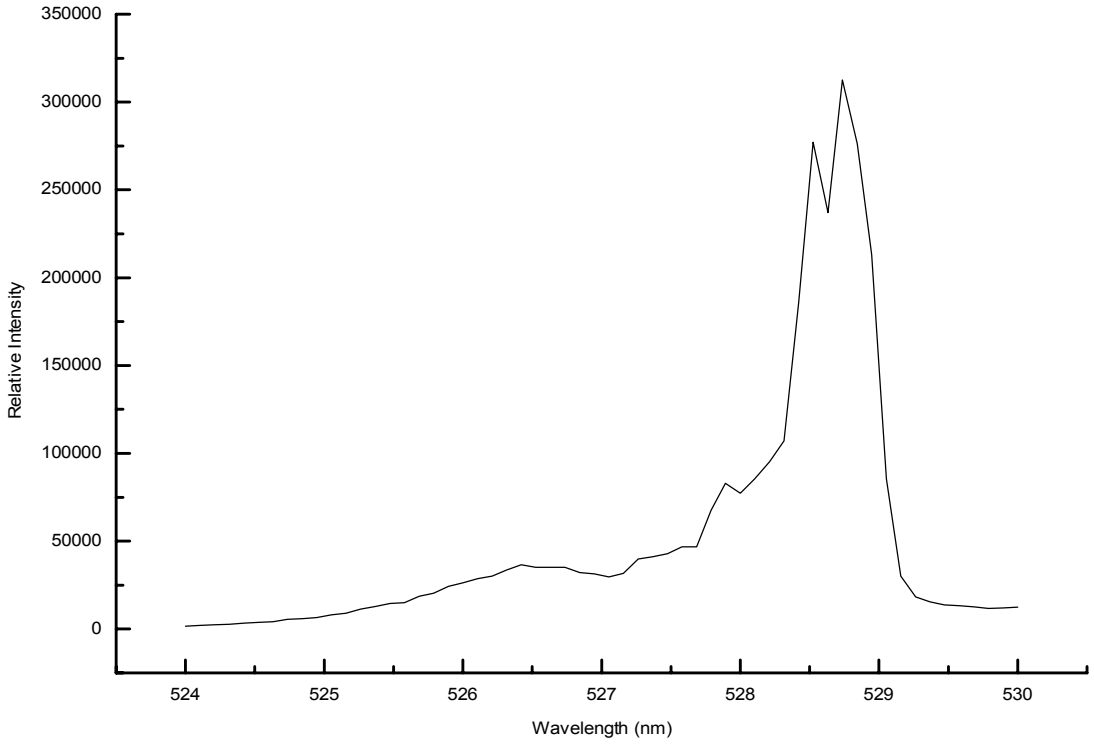

Figure 4-2. Broad-band $^7F_0 \rightarrow {}^5D_1$ excitation of nanocrystalline 0.1 mol %Eu^{3+}:CaO. The spectrum was recorded with a 0.25-m monochromator set at 614 nm with a 6-nm bandpass. The scan rate was 1.0 Angstroms/sec.

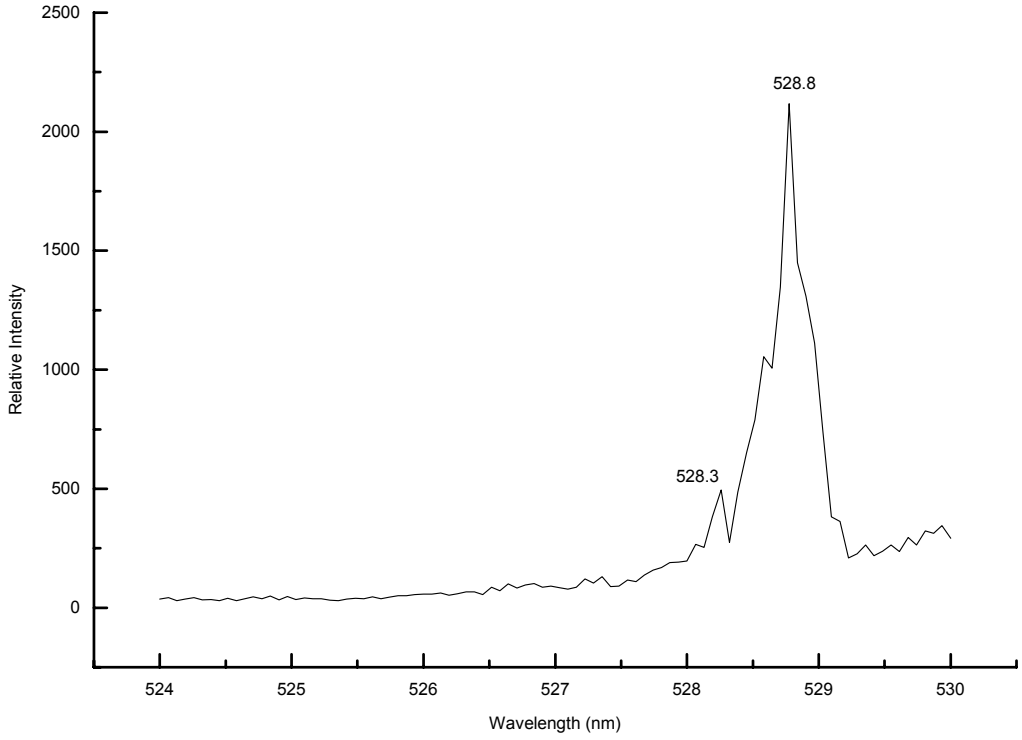

Figure 4-3. Broad-band $^7F_0 \rightarrow {}^5D_1$ excitation spectrum of nanocrystalline Eu^{3+}:CaO after altering laser energy. The spectrum was recorded with a 0.25-m monochromator set at 614 nm with a bandpass of 6 nm. The scan rate was 0.300 Angstroms/sec.

defined edges and the particles are agglomerated in a network. This sample is representative of all samples that are prepared with 400 Torr N_2. For particle size determinations, the magnification is typically 86,000 or lower since edge distortions can appear at higher magnifications. Figure 4-5 shows the histogram generated from the survey results of the micrographs of the nanocrystalline Eu^{3+}:CaO. The dominant particle sizes of the nanocrystals prepared by the preceding method were 23 nm with a range of 12-29 nm.

Nanocrystalline Eu^{3+}:CaO with a pre-vaporization concentration of 0.1 mol % of dopant was successfully made by the laser-vaporization-gas-phase condensation method. The TEM results showed that the dominant particle diameter was 23 nm and the particle diameter distribution was 12-29 nm. A qualitative analysis of the TEM results shows that . the particles are networked and agglomerated and this behavior is consistent with other metal oxide nanocrystalline materials reported in the literature.[2,39,81,87,88]

Now that single-phase nanocrystalline Eu^{3+}:CaO has been made, characterized, and shown to fluoresce, site-selective spectroscopic experiments can be performed to determine the effect of concentration, sample age, and annealing on the luminescence spectra. Site-selective spectra are obtained using a higher resolution monochromator with a smaller bandpass and scanning the dye laser. In the site-selective excitation spectra, the individual sites that the europium ion can occupy are shown.

By preparing nanocrystalline samples with different europium concentrations and obtaining the site-selective excitation spectra, the dopant distribution can be investigated. It is speculated that the dopant distribution in the nanocrystalline system will be different surface instead of the interior. There are few reports in the literature regarding dopant

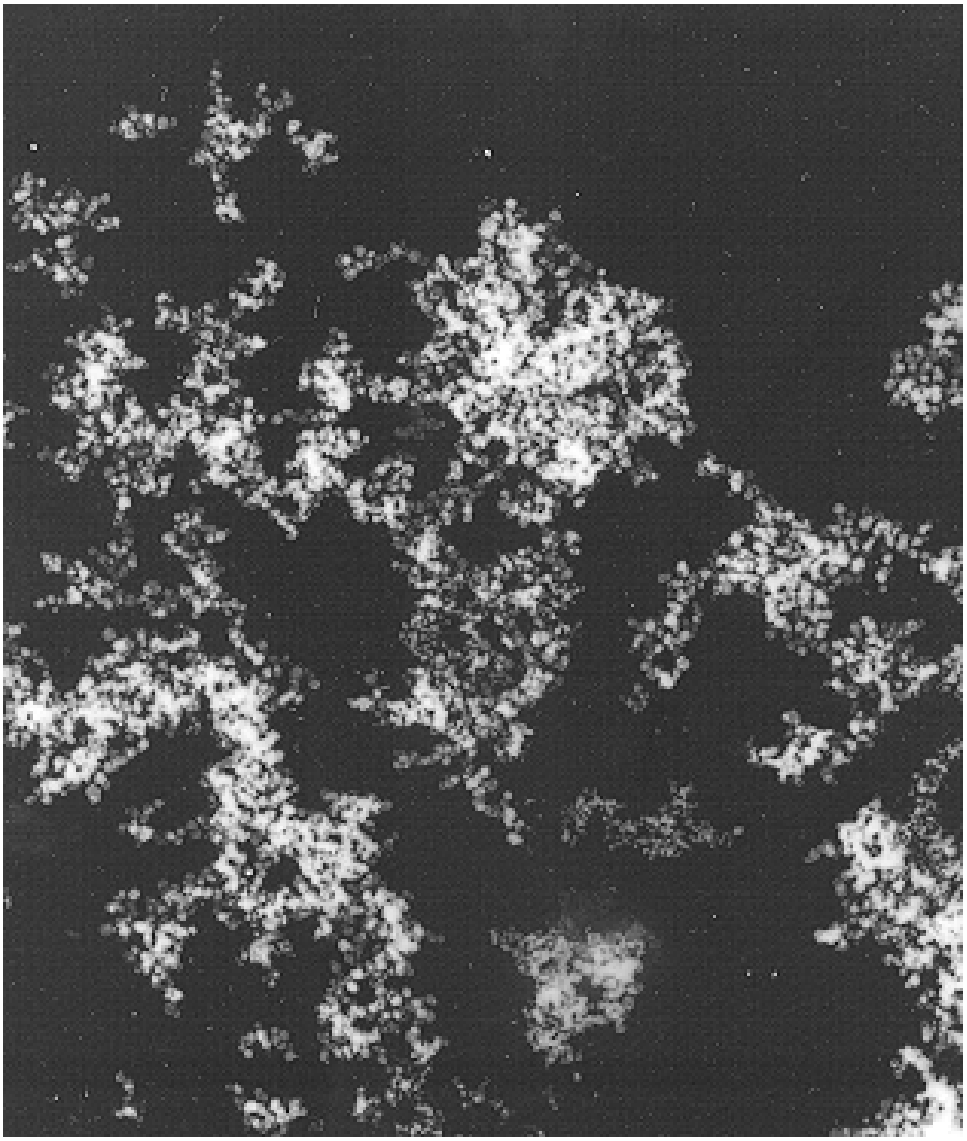

Scale: __ 115 nm

Figure 4-4. Negative of TEM image of nanocrystalline Eu^{3+}:CaO prepared with 400 Torr N_2. The white images are the nanocrystals. The TEM instrument magnification was 31000. The sample corresponds to the spectrum shown in 4-3.

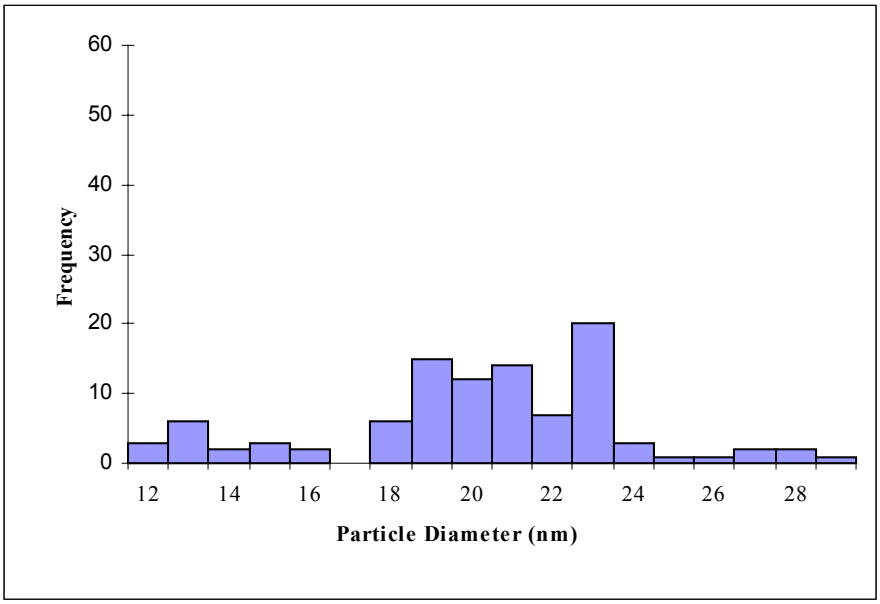

Figure 4-5. Histogram of results from TEM of 0.1% Eu^{3+}:CaO prepared with 400 Torr N_2.

distribution in nanocrystalline systems and the ones that do exist have not been discussed in the context of the luminescence spectra.

Chapter 5: Initial Survey of Site-Selective Spectroscopy and Defect Chemistry of Nanocrystalline Eu^{3+}:CaO

5. A. Introduction

Site-selective spectroscopy allows for the study of crystalline systems in which the valence of the dopant ion is different from that of the host ions. The presence of multiple sites that result from charge compensation within the solid gives rise to optical spectra that are complex, but individual sites are discernable by either exciting specific absorption lines or by monitoring specific fluorescence lines[70]. By studying the individual sites, it is possible to gain insight into the defects that can occur within a solid.

Maier[89] suggests that referring to all departures from ideal structure as defect chemistry allows for the unification of many different phenomena, such as ionic conduction in crystals, doping effects in semiconductors, color centers in alkali metal halides, corrosion of metals, sintering of solid materials, mechanisms of gas sensors, performance of photosensitive electrodes, and many more. In such phenomena, the concentration of defects plays a crucial role.

The most elementary type of defect in a solid is a point defect [89]. In the most simplistic definition, a point defect is either an extra particle or a missing particle in a solid. A 2-D schematic of point defects is shown in Figure 5-1.

The point defect that consists of an extra or interstitial atom is commonly referred to as a Frenkel defect and the defect that consists of a missing atom or vacancy is a Schottky defect [89]. In defect terminology, dopant atoms constitute extrinsic point defects while intrinsic point defects are vacancies or self-interstitials [89]. Under thermal equilibrium, any crystal will contain a certain concentration of intrinsic point defect species, which

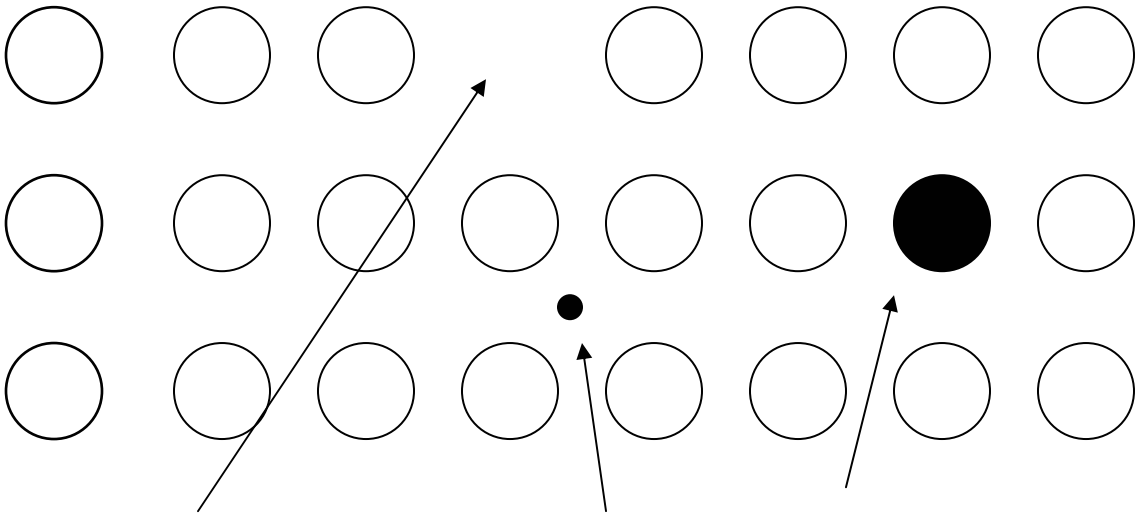

Figure 5-1. 2-D schematic illustrating the types of point defects in a solid [90].

leads to a lower Gibb's free energy of the crystal compared to a defect-free crystal [91].

In a binary oxide, such as CaO, the introduction of charged defects requires the simultaneous introduction of defects of opposite charge to maintain a neutral charge [92]. It is well established from early work that the intrinsic defect in the rocksalt structure, which calcium oxide possesses, is the Schottky defect [93]. The Kroger-Vink notation (as described on page iv) used for the Schottky defect is shown below for a compound whose ideal composition is MX:

$$M_M + X_X \rightarrow MX + V'_M + V^{\bullet}_X$$

where M_M represents a cation in a cation site and X_X represents an anion in an anion site. MX represents the formation of a molecule, while V_M and V_X are cation and anion vacancies, respectively [89]. By convention, in defect chemistry not only must the particles and charges on the two sides of the equation balance, but the lattice sites must balance as well. For CaO, the intrinsic or Schottky defect is one calcium vacancy and one oxygen vacancy [70].

In addition to the intrinsic defects in a solid, additional defects can be generated by doping. The replacement of a Ca^{2+} ion by an Eu^{3+} ion is charge compensated by the generation of a vacancy at a calcium site [70]. Equilibrium is established by the simultaneous reduction of the concentration of anion vacancies. Therefore, the introduction of an ion with an effective positive charge causes an increase in the concentrations of all negatively charged defects and a reduction in the concentrations of all positively charged defects [89]. The positive defect for CaO doped with Eu^{3+} is the oxygen vacancy, $V^{\cdot\cdot}_O$, and the negative defect is the calcium vacancy, V''_{Ca} [3].

The site-selective laser spectroscopy results of bulk Eu^{3+}:CaO were published by L.C. Porter and J.C. Wright in 1982 [70]. Porter and Wright found that two dominant rare earth sites are present in Eu^{3+}: CaO – a cubic site (site B) and an orthorhombic site (site A). The B site has only one line in the $^7F_0 \rightarrow {}^5D_1$ excitation spectrum of the bulk material which is characteristic of an ion in a site with cubic symmetry [70]. The A site has the maximum number of lines possible for the $^7F_0 \rightarrow {}^5D_1$ transition (3 lines) and the excitation spectrum observed by Porter and Wright was consistent with the orthorhombic site that was observed by McGeehin and Henderson in Gd^{3+}:CaO [94]. Table 5-1 shows the wavelengths that were obtained from Porter and Wright's experiments. Porter and Wright believe the A site corresponds to an associated pair site; a site in which the Eu^{3+} ion and its charge compensation, (V''_{Ca}), are paired. Porter and Wright observed a relatively long lifetime for the A and B site $^5D_1$ level, (0.33 and 0.73 ms), which is characteristic of a single Eu^{3+} ion site not a cluster site[70]. Clusters consist of several dopant ions and their charge compensations[95].

Porter and Wright's[70] data for bulk Eu^{3+}:CaO show that at low dopant concentration, the cubic site dominates. As the concentration of the dopant is raised, the cubic/orthorhombic ratio approaches 1. To obtain the data, Porter and Wright prepared a series of samples containing different europium concentrations (3.2×10^{-5} to 1.9×10^{-2} mol %) and measured the $^7F_0 \rightarrow {}^5D_1$ excitation spectra. Their measurements involved the use of a broadband monochromator to monitor luminescence from all sites initially and a 1-m monochromator for the site-selective measurements. Porter and Wright took the intensity of the lines from the spectra of site A and the intensity of the line from the spectrum of site B to set up a ratio of the B/A site. This ratio was plotted as a function of

Table 5-1. Wavelengths that were reported from the site-selective excitation spectra of bulk Eu^{3+}:CaO by Porter and Wright[70]. The fluorescence wavelength that was used for site A was 613.1 nm and 594.1 nm for site B.

	Wavelength (nm)	Relative Peak Heights
Site A (orthorhombic)	527.4	0.3
	528.3	0.5
	528.8	1
Site B (cubic)	528.9	Not applicable

the europium concentration in the sample. Porter and Wright concluded that at europium concentrations of greater than 0.002 mol %, there is an equal population of europium ions in cubic and orthorhombic sites.

According to Porter and Wright,

> if one assumes simple mass action relationships describe the pairing of rare earth dopants with their V''_{Ca} compensations and the intrinsic defect equilibria between V''_{Ca} and $V^{\cdot\cdot}_{O}$ defects, the system can be described by the equations
> $K_p = [(Eu_{Ca} * V_{Ca})']/[Eu^{\cdot}_{Ca}]\,[V''_{Ca}]$ and $K_I = [V''_{Ca}]\,[V^{\cdot\cdot}_{O}]$.
> The conditions for mass and charge balance demand
> $C_{Eu} = [Eu^{\cdot}_{Ca}] + [(Eu_{Ca} * V_{Ca})']$ and $2[V^{\cdot\cdot}_{O}] + [Eu^{\cdot}_{Ca}] = [(Eu_{Ca} * V_{Ca})'] + 2[V''_{Ca}]$,
> respectively. This model predicts that the orthorhombic site concentration will increase relative to the cubic site concentration as the dopant concentration (C_{Eu}) is raised until they become equal at high concentration. In this limit, a single calcium vacancy compensates one Eu^{3+} locally and one Eu^{3+} distantly[70].

As a result of Porter and Wright's study, experiments were initiated to produce samples of nanocrystalline Eu^{3+}:CaO with different dopant concentrations. The ultimate goal was to use laser spectroscopy to determine the cubic/orthorhombic ratio and therefore the dopant distribution in 13-nm Eu^{3+}:CaO, since dopant distributions in nanocrystals are expected to differ from the distributions in bulk materials.

5. B. Experimental

5. B. 1. Sample Preparation

The samples for this study were made using the laser-vaporization-gas-phase condensation method described in Chapter 3. It was known from the work performed by Eilers and Tissue for Eu_2O_3 nanocrystals [81] and from the work with nanocrystalline Eu^{3+}:Y_2O_3, that lower chamber pressure would yield smaller particles so all of the samples prepared for this study were made using 10 Torr nitrogen in the vaporization chamber.

Bulk Eu^{3+}:CaO samples were prepared with concentrations of 4 x 10^{-4} mol % Eu^{3+}, 5 x 10^{-4} mol % Eu^{3+}, 6 x 10^{-3} mol % Eu^{3+}, 3 x 10^{-2} mol % Eu^{3+}, and 1 x 10^{-1} mol % Eu^{3+}. All of the samples were prepared by first dissolving the exact stoichiometry of Eu_2O_3 in 25 mL of 5% HNO_3. The solution was added to the CaO and heated to evaporate the liquid. The mixture was placed into a furnace and sintered at 1100 ^oC overnight. Following removal from the furnace, the material was pressed into pellets. The pellets were sintered at 1000 ^0C for several hours to increase pellet hardness. Typically, two pellets were prepared from a single batch of powder. The pellets were vaporized by the laser-vaporization, gas-phase condensation method described previously. For all experiments, the laser power of the continuous CO_2 laser was 40 W, the chamber pressure was 10 Torr, and the cold finger distance from the target was 3 cm. The laser power was increased to 40 W for these experiments to minimize the chance of selective vaporization of Eu_2O_3, which results in mixed-phase samples.

5. B. 2. Transmission Electron Microscopy

Transmission electron microscopy, as described in detail previously, was used to determine the dominant particle diameter and particle diameter distribution of the nanocrystals.

5. B. 3. ICP-AES

Since the goal of this study was to change the dopant concentration in the nanocrystals and to use laser spectroscopy to study the site-selective luminescence behavior, the exact dopant concentrations were determined. ICP-AES (inductively-coupled plasma atomic emission spectroscopy) measurements were performed by Nancy Ballengee in the Department of Soil Science at Virginia Tech and by the author, with the

assistance of Professor Gary Long, in the Department of Chemistry at Virginia Tech. Ballengee analyzed for europium and Williams analyzed for both europium and calcium. The ICP-AES experiments were performed on the same sample solutions by both Ballengee and Williams, therefore eliminating variability in the sample preparation.

The preparation of the nanocrystalline Eu^{3+}:CaO samples for analysis by ICP-AES (inductively-coupled plasma atomic emission spectroscopy) was done by dissolving 4.2 mg of each sample in 5 mL 5 % v/v HNO_3 and diluting to a total volume of 30 mL with deionized water. The nanocrystals were weighed using an electronic balance. For Eu calibration purposes, a series of solutions were prepared using a commercial standard reference solution (Aldrich) of 980 μg/mL Eu in 5 % v/v HNO_3. The concentrations of the prepared Eu standards were 9.8 ppm, 0.098 ppm, and 0.00098 ppm. For Ca calibration purposes, a series of solutions were prepared by dissolving the appropriate masses of $CaCl_2$ in acidified deionized water so that the final concentrations of the solutions were 10 and 1 ppm. The samples, standards and a blank were analyzed by ICP-AES. The instrument used for the analysis in the Department of Soil Science was a SpectroFlame Modula Tabletop ICP (FTMOA-85D) and the instrument used in the Department of Chemistry was a Perkin-Elmer ICP 6000.

5. B. 4. Site-Selective Laser Spectroscopy of Nanocrystalline Eu^{3+}:CaO

The site-selective excitation measurements were made differently than the broadband excitation measurements described previously in chapter 2. For the site-selective measurements, the pulsed YAG-pumped dye laser, with Coumarin 540A dye, was used as the excitation source and a 1-m monochromator was used to monitor the fluorescence

instead of a 0.25-m monochromator. The 1.0-m monochromator was used because the higher resolution allows for emission from individual sites to be measured.

Since site-selective spectroscopy can be used to study the structure of nanocrystalline materials, site-selective laser spectroscopy experiments were first used to determine the phase distribution of the nanocrystals. Since the phase distribution study revealed the existence of mixed phases in some samples, a study of annealed nanocrystalline Eu^{3+}:CaO using site-selective spectroscopy was performed. The goal of the annealing experiment was to determine how annealing would affect the phase distribution in the nanocrystals. Following the annealing study, a series of experiments were performed to determine how experimental parameters would affect the luminescence spectra of nanocrystalline Eu^{3+}:CaO.

5. C. Results and Discussion

5. C. 1. Transmission Electron Microscopy

Figure 5-2 shows the TEM micrograph of Eu^{3+}:CaO prepared with 10 Torr of nitrogen in the vaporization chamber. The morphology of the nanocrystals was similar to that of samples prepared with 400 Torr of nitrogen. When the micrograph negative is placed on a light box for viewing, the particles show well-defined edges and are arranged in a network array. For particle size determinations, the magnification is typically 86,000 or lower to allow for more precise measurements. At higher magnifications, some distortion of edges was observed. All particle size determinations were made using the micrograph negatives: however, enlarged positives are shown instead of the negatives for clarity. Figure 5-3 shows the histogram that was generated from the survey results of the micrographs. The dominant particle size was 13 nm with a particle diameter range of 9-

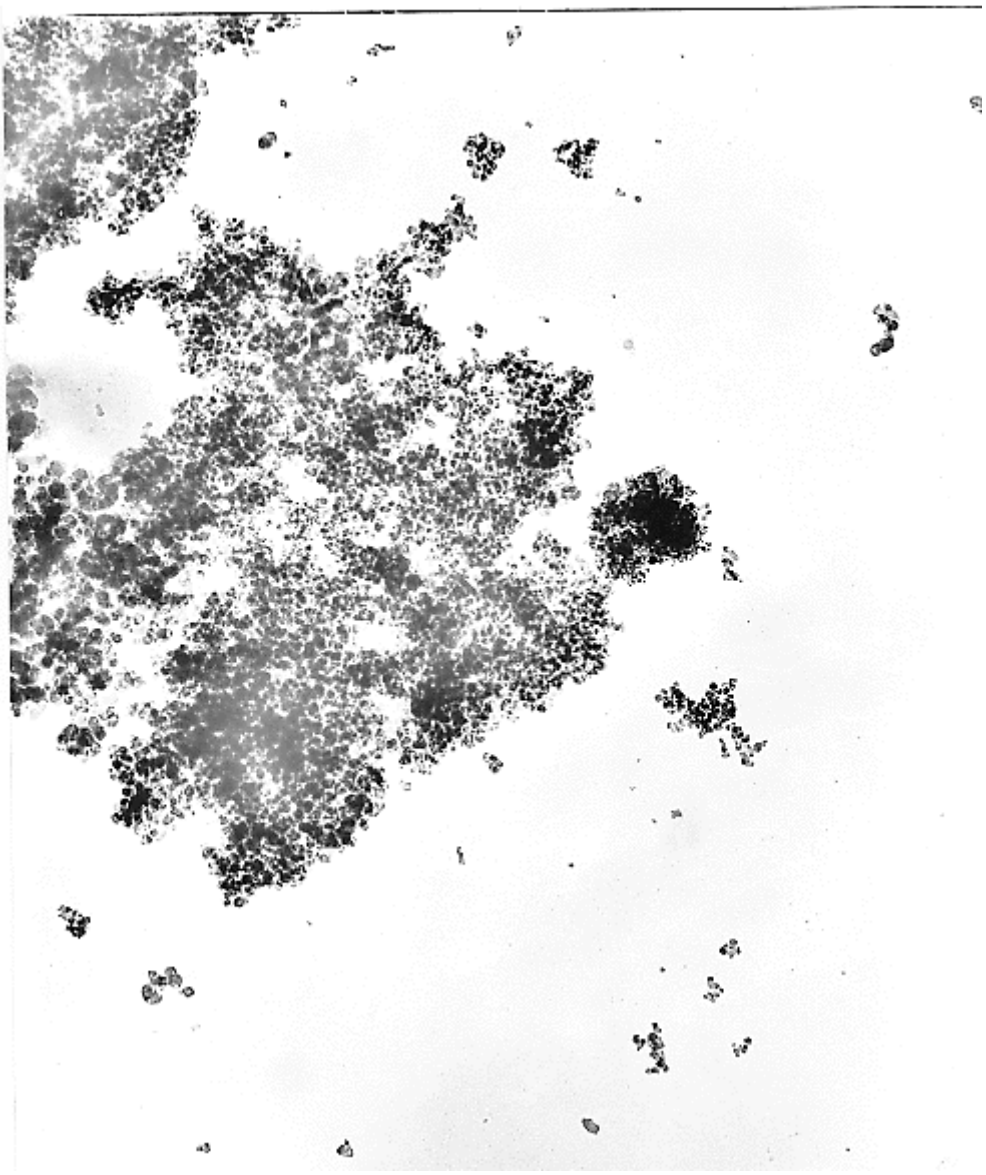

Scale: __ 52 nm

Figure 5-2. Positive of TEM image of 0.02 mol % Eu^{3+}:CaO prepared with 10 Torr N_2. The dark images are the nanocrystals. The TEM instrumental magnification was 24,000.

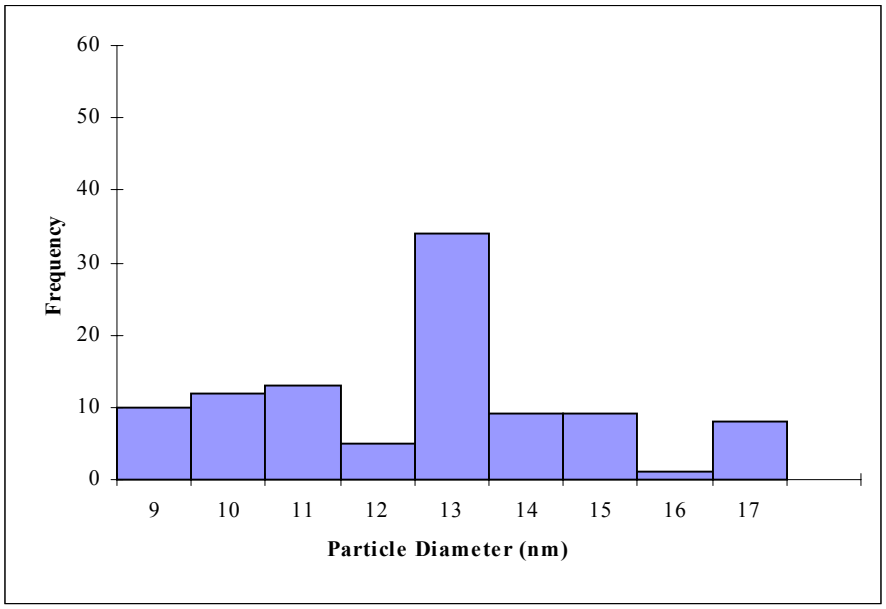

Figure 5-3. Histogram of results from TEM of nanocrystalline Eu^{3+}:CaO prepared with 10 Torr N_2.

17 nm.

5. C. 2. ICP-AES

Table 5-2 shows the data obtained from the ICP-AES analysis of nanocrystalline Eu^{3+}:CaO samples. The ICP-AES results, shown in Table 5-2, indicate that the measurements are precise. The % RSD values are less than 10 %, which indicates good precision. It was noted at the time of the experiments for calcium that the nebulizer was clogged. As a result, the nebulizer was removed and reinserted. After reinsertion of the nebulizer, the standard solutions were analyzed for calibration purposes. Following the analysis of the standard solutions, the sample solutions were analyzed. The calibration curve that was obtained for calcium is shown in Figure 5-4.

While the samples with the highest europium concentrations are outside the range of the standard solutions, at 24.582 and 11.222 ppm, the values are well within the limit of linearity for calcium. According to the Perkin-Elmer ICP instrument handbook, the limit of linearity for calcium is approximately 200 ppm. Therefore, the calibration data provide a reasonable indicator of instrument response. The europium data were obtained directly from Nancy Ballengee in the Department of Soil Science and therefore the calibration data are not available. The europium data that were obtained by the author were discarded since the concentrations of europium were near the detection limit of the Perkin-Elmer ICP 6000.

The concentration data were used to determine the percentage of europium in the nanocrystalline samples, shown in Table 5-3. To estimate the % RSD of the final ratio of calcium and europium, the following equation was used:

% RSD of final result = $\sqrt{c^2_{Eu} + c^2_{Ca} + c^2_{Eu}}$ where c is the % RSD of a sample

Table 5-2. Data obtained from the ICP-AES analysis of nanocrystalline Eu^{3+}:CaO samples.

Sample Identification Number	As-prepared concentration of Eu^{3+}:CaO prior to nanocrystalline synthesis (mol % Eu^{3+})	Concentration of Eu in solution (ppm) determined by ICP-AES	% RSD of Eu measurement	Concentration of Ca in solution (ppm) determined by ICP-AES	% RSD of Ca measurement
133	0.1	7.91	0.702	24.582	0.84
205	0.032	0.4662	0.739	11.222	1.59
203	0.006	0.0541	0.815	0.9495	8.92
204	0.0005	0.0368	1.982	3.644	8.41
206	0.0004	0.0671	1.226	8.137	5.09

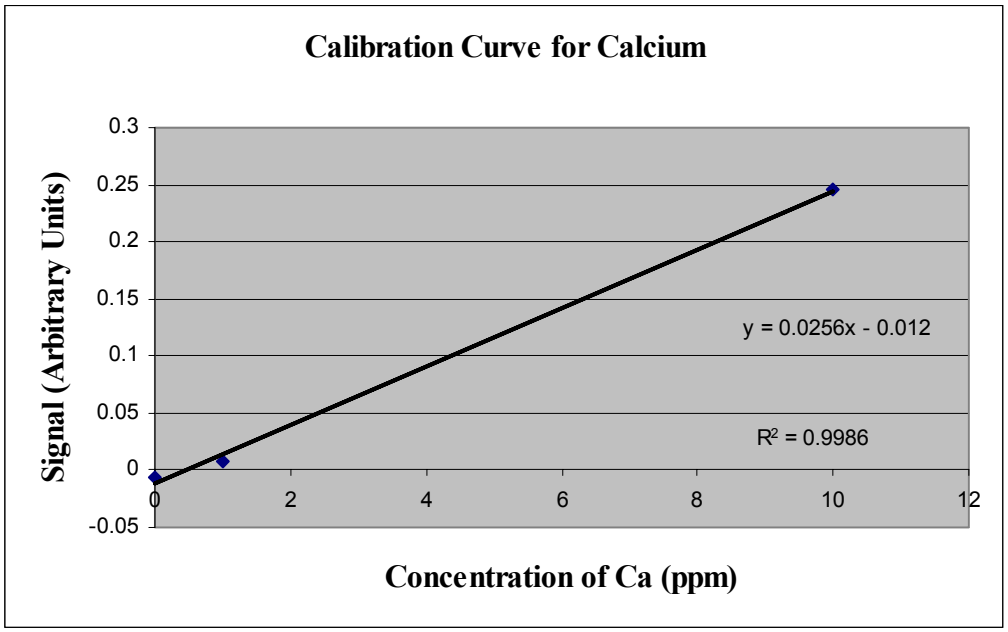

Figure 5-4. Calibration curve generated from the ICP-AES analysis of calcium standards.

measurement[96].

To determine the total composition of the nanocrystalline samples, the following equation was used: $C_0 = C_s \times V \times 10^{-4} / W$

where:

C_0 = concentration of metal in sample (%)

C_s = concentration of metal in sample solution (ppm)

V = final volume of sample solution (mL)

W = weight of original sample (g)

The results of the calculations are shown in Table 5-4.

From the percentages shown in Table 5-4, the total composition of the samples (also shown in Table 5-4) was calculated by assuming a 100 g sample and using the formula masses of the oxides[97].

The results in Table 5-4 indicate that either the nanocrystals contained other compounds, that the weights of the nanocrystals (0.0042 g) were inaccurate, or that the nanocrystals did not completely dissolve since the percentages did not add to 100 percent.

It is not likely that the nanocrystals failed to dissolve since the materials were dissolved in 5 mL of 5 % v/v nitric acid before being diluted to the 30 mL mark with deionized water. Since all of the nanocrystals were more than 2 months old by the time the ICP-AES analyses were performed, it is likely that the calcium oxide was converted to calcium carbonate and calcium hydroxide by the following reactions:

$CaO\ (s) + CO_2\ (g) \rightarrow CaCO_3\ (s)$

$CaO\ (s) + H_2O\ (g) \rightarrow Ca(OH)_2\ (s)$

Calcium hydroxide is slightly soluble in water (0.268 g/L) at room temperature but

Table 5-3. The pre-vaporization concentration of Eu (mol %) and mol % of Eu in Eu^{3+}:CaO nanocrystals.

Sample Identification Number	Pre-vaporization concentration of Eu in bulk samples (mol %)	Mol % Eu in nanocrystals and % RSD
133	0.1	8.5 ± 1.3 %
205	0.03	1.1 ± 1.9 %
203	0.006	1.5 ± 9.0 %
204	0.0005	0.27 ± 8.9 %
206	0.0004	0.22 ± 5.4 %

Table 5-4. Mass percentage of Ca and Eu and mass percentage of the oxides in nanocrystalline Eu^{3+}:CaO.

Sample # /Mol % Eu in Bulk Pellet	[Eu] in solution (ppm)	Weight of nano sample (g)	Mass % Eu in nano sample	Mass % Eu_2O_3 in nano sample	[Ca] in solution (ppm)	Mass % Ca in nano sample	Mass % CaO in nano sample
133 / 0.1	7.91	0.0034	6.98	2.0	24.582	21.69	38.7
205 / 0.03	0.4662	0.0042	0.333	0.095	11.222	8.016	14.3
203 / 0.006	0.0541	0.0042	0.0386	0.011	0.9495	0.678	1.22
204 /0.0005	0.0368	0.0042	0.0263	0.0075	3.644	2.60	4.65
206/0.0004	0.0671	0.0042	0.0480	0.0136	8.137	5.81	10.4

dissolves readily in strong acids[98]. Calcium carbonate has a solubility of 0.013 g/L in water at room temperature[98] but dissolves in nitric acid to form soluble calcium nitrate, carbon dioxide and water. The suggested protocol for performing ICP-AES analysis of europium oxide is the use of 5 % nitric acid to dissolve the solid. Therefore, the assumption is that the nanocrystals did dissolve in solution.

It is likely that the weights of the nanocrystals were inaccurate because a quantitative transfer of nanocrystalline materials is nearly impossible. In all experiments involving nanocrystalline samples, there is typically some loss of material because the nanocrystals become airborne very easily. Since the amount of material transferred was so small (0.0042 g in all cases except one), even a small loss would significantly affect the results. However, a loss of nearly 90 % does not seem likely. Therefore, the assumption is that the masses do not add to 100 percent due to both lack of quantitative material transfer and the presence of other compounds, such as calcium carbonate or calcium hydroxide.

The data shown in Table 5-4 were evaluated to estimate the accuracy of the concentration measurement. It was determined that the presence of either calcium carbonate or calcium hydroxide, along with a systematic error of unknown origin, renders the concentration measurement inaccurate. It is speculated, however, that the post-vaporization concentrations of Eu are higher in all of the nanocrystalline samples than in the bulk materials from which the nanocrystals were prepared, due to the difference in the melting points of CaO and Eu_2O_3. The melting points differ by more than 10 %, which increases the chance of selective vaporization of Eu_2O_3, as the pellets are vaporized.

To try to estimate the amount of error in the concentration measurements, the sample that was deemed to be most accurate (sample 133) was considered. This particular

sample was selected because it had the highest pre-dopant concentration, the % RSD was the lowest value obtained (<1 %), and the masses of the oxides added much closer to 100 % than the other samples (approximately 30 %). The percentage error in the mass percentage is therefore approximately 70 %. Therefore, as a rough estimate, the concentrations could have an error of approximately 70 % or higher. Even applying errors much higher than 70 %, indicate that there was Eu enrichment in all of the nanocrystalline samples. This probable increase in dopant concentration when the bulk material is vaporized and condensed onto a cold finger suggests that the Eu_2O_3 is selectively vaporized and since Eu_2O_3 has a lower melting point than CaO, this is a reasonable speculation.

To determine the degree of enrichment in the nanocrystals, the data were analyzed to determine an enrichment factor. Since the accuracy of the concentration has been determined to have an error of approximately 70 %, the actual degree of enrichment could be expected to fall between a range of 26-144 for sample 133. For samples 205, 203, 204, and 206, the ranges are 11-63, 75-425, 162-918, and 165-935, respectively. Using these factors will allow for an estimation of how the pre-vaporization and post-vaporization concentrations might vary. Currently, there are no quantitative results in the literature regarding the degree of enrichment in nanocrystalline materials prepared by the laser-vaporization-gas-phase condensation method so these speculated enrichment factors cannot be compared with any other experimental results. However, it has been suggested that post-vaporization concentrations of Eu^{3+} may be larger based on luminescence results obtained with Eu^{3+}:Y_2O_3[99].

To test the reproducibility of the nanocrystalline synthesis, two samples with the same pre-vaporization concentration of dopant were prepared. The results obtained from the ICP-AES analysis (Table 5-5) indicate that the variation in the Eu concentration (ppm) was 30 % and the variation in the Ca concentration was 33%. These variations in concentration are attributed to inconsistent vaporization of the bulk materials. Although the concentrations show a large variation, the results indicate that the overall ratio of Ca to Eu has a relative error of 5 %. Due to the inaccuracy associated with the concentration measurements, however, the reproducibility cannot be estimated with confidence.

The concentrations and enrichment factors suggested here are not intended as a rigorous statistical analysis of the data. To determine the true reproducibility of the nanocrystalline synthesis, many more experiments would need to be performed in order to determine an average and standard deviation. Therefore, the post-vaporization concentrations shown in all of the figures should be considered only as a rough estimate.

The ICP-AES results obtained from this initial survey of nanocrystalline Eu^{3+}:CaO indicate that future experiments on nanocrystalline materials prepared by laser-vaporization-gas-phase condensation should include a dopant concentration study. Many of the literature reports regarding doped nanocrystalline materials do not include a concentration study[100-102]. For future studies on this particular material, vaporizing with a higher laser output may eliminate some of the problems associated with selective vaporization.

To obtain concentration data for nanocrystalline Eu^{3+}:CaO, it is suggested that concentration measurements be made soon after the laser spectroscopic analysis if percent composition of the oxides is desired. The hygroscopic nature of calcium oxide is

Table 5-5. Nanocrystalline Eu^{3+}:CaO reproducibility results obtained from ICP-AES analysis.

Sample I.D.	Pre-vaporization concentration (mol %)	Concentration of Eu (ppm) / % RSD	Concentration of Ca (ppm) / % RSD	Ca/Eu ratio	Mol % Eu
202	0.0005	0.0522 / 0.875	5.442/ 1.92	396.2	0.25
204	0.0005	0.0368/ 1.982	3.644/ 8.41	376.3	0.27

likely to be further accelerated by the reduced particle size of the nanoparticles, which increases the surface area. As a result, the formation of $CaCO_3$ and $Ca(OH)_2$ will be accelerated compared to the bulk.

Concentration data tell how much europium is present in the nanocrystals but does not tell the phase distribution in the nanocrystals. Site-selective laser spectroscopic results provide the phase distribution and are presented in the following section.

5. C. 3. Determination of Phase Distribution by Site-selective Laser Spectroscopy of Nanocrystalline Eu^{3+}:CaO

The site-selective spectroscopic results for nanocrystalline Eu^{3+}:CaO are arranged from low to high dopant concentration. The spectra of A and B sites are shown together for comparison of the relative intensity of the site A and B lines. The wavelengths used to monitor the fluorescence with the monochromator were determined from the broadband experiments described in chapter 4 since these wavelengths were consistent with the wavelengths used by Porter and Wright[70] for the bulk samples.

Figure 5-5 shows the $^7F_0 \rightarrow {}^5D_1$ excitation spectrum obtained by monitoring the fluorescence from sites A and B of the 0.22 mol % Eu^{3+}:CaO sample. In the site A spectrum there are four distinct peaks at 527.4 nm, 528.0 nm, 528.3 nm, and 528.8 nm and an unresolved doublet peak with a maximum at 526.1 nm. The peaks at 527.4 nm, 528.3 nm, and 528.8 nm were expected since those positions correspond to the wavelengths obtained in the experiments with bulk sample published by Porter and Wright[70]. The peaks at 528.0 nm and 526.1 nm correspond to the peaks found in the monoclinic Eu_2O_3 spectrum [73], which indicates that there are two Eu-containing phases present in this sample; the cubic phase of CaO and the monoclinic phase of Eu_2O_3.

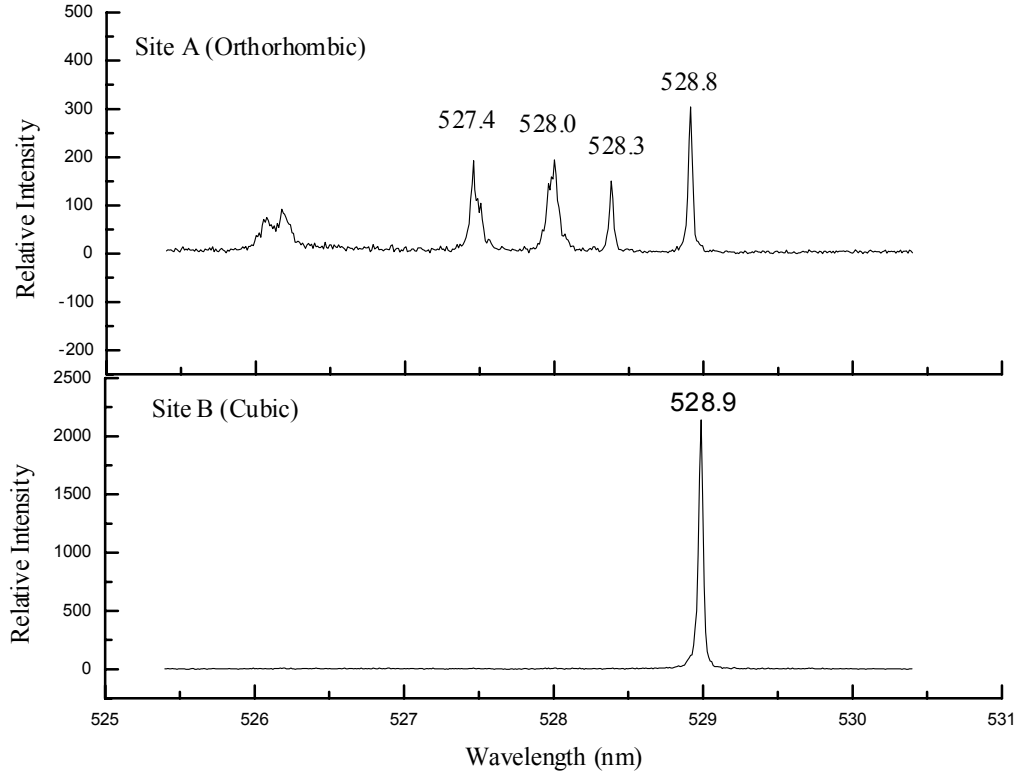

Figure 5-5. Site-selective excitation spectra of sites A and B in nanocrystalline 0.22 mol mol % Eu^{3+}:CaO (sample # 206). The gate and delay for the A were 1ms and 1 μs. The gate and delay for the B were 1 ms and 400 μs. For the A spectrum, the 1-m monochromator was set to 613.1 nm. For the site B spectrum, the 1-m monochromator was set to 594.1 nm. The scan rate of the dye laser was 0.05 Angstroms/sec, and the laser energy was 280 μJ.

Figure 5-6 shows the spectral results obtained by monitoring the fluorescence of sites A and B in nanocrystalline 0.27 mol % Eu^{3+}:CaO. The site A spectrum shows three lines for site A at 527.4 nm, 528.4 nm, and 528.8 nm. These line positions correspond to the wavelengths obtained for site A in the bulk material studied by Porter and Wright [70]. The one line in the spectrum of site B at 528.9 nm corresponds to the wavelength of 528.9 nm obtained for site B in the bulk sample by Porter and Wright [70]. These results indicate that the 0.27 mol % sample is a single-phase sample: cubic Eu^{3+}:CaO.

Figure 5-7 shows the $^7F_0 \rightarrow {}^5D_1$ excitation spectrum obtained by monitoring the fluorescence from sites A and B for the nanocrystalline 1.1 mol % Eu^{3+}:CaO. The spectrum contains five distinct peaks at 526.1 nm, 526.3 nm, 527.4 nm, 528.0 nm, and 528.8 nm. The peaks at 527.4 nm, and 528.8 nm were expected since those positions correspond to the wavelengths obtained in the single-phase samples. The additional peaks correspond to the peaks found in the monoclinic Eu_2O_3 spectrum [73]. The one line at 528.9 nm is consistent with the line for site B in the bulk sample. These spectral results indicate that the 1.1 mol % sample has two phases; cubic Eu^{3+}:CaO and monoclinic Eu_2O_3.

Figure 5-8 shows the site-selective results from monitoring the fluorescence of sites A and B in the nanocrystalline 1.5 mol % Eu^{3+}:CaO sample. The spectrum shows three lines for site A at 527.4 nm, 528.4 nm, and 528.8 nm. These line positions correspond to the wavelengths obtained for site A in the bulk material by Porter and Wright[70]. The one line at 528.9 nm corresponds to the wavelength of 528.9 nm obtained for site B in the bulk material by Porter and Wright[70]. These results indicate that the 1.5 mol % sample is single-phase: cubic Eu^{3+}:CaO.

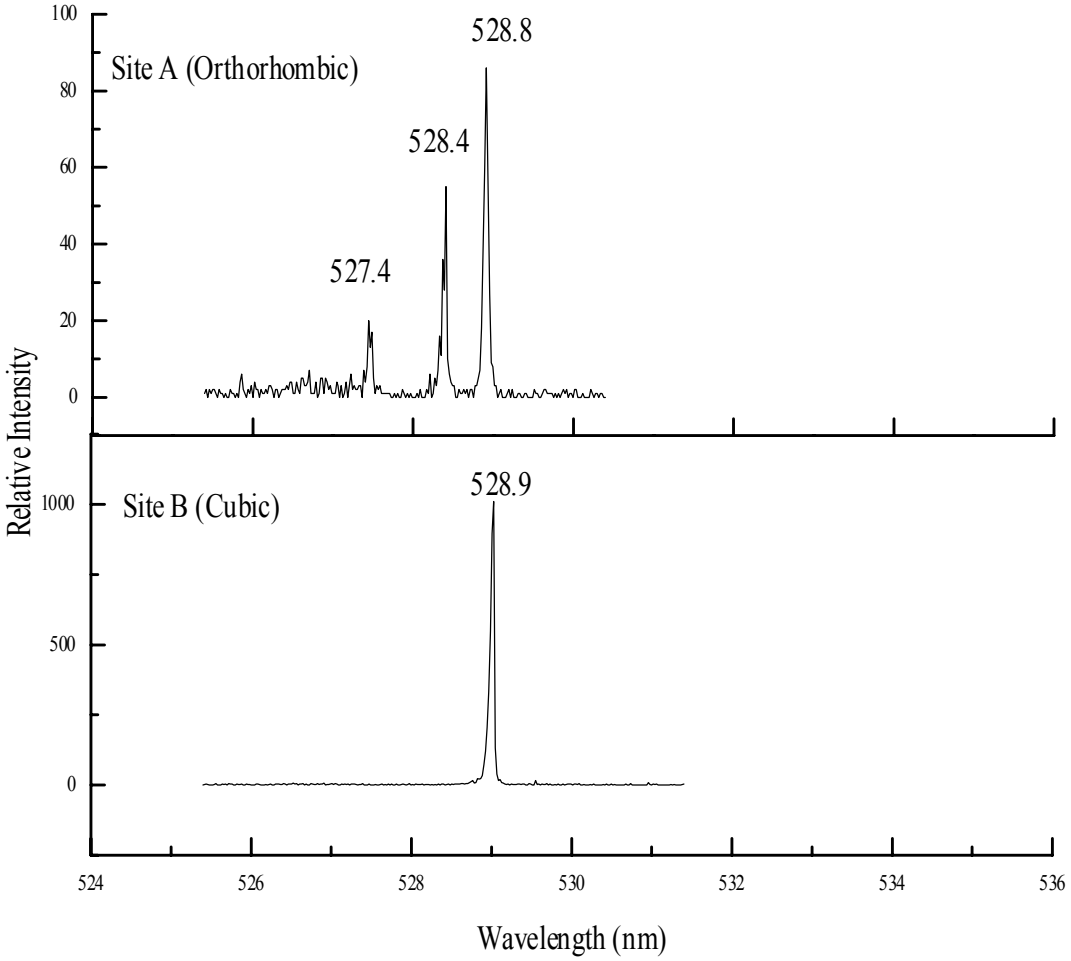

Figure 5-6. Site-selective excitation of nanocrystalline 0.27 mol % Eu^{3+}:CaO (#204). The delay and gate for the site A (top) spectrum were 1 μs and 1 ms. The delay and gate for the site B (bottom) spectrum were 400 μs and 1 ms. To obtain the site A spectrum, the 1-m monochromator was set to 613.1 nm. For site B, the 1-m monochromator was set to 594.1 nm. The scan rate of the dye laser was 0.1 A/sec, and the laser energy was 280 μJ.

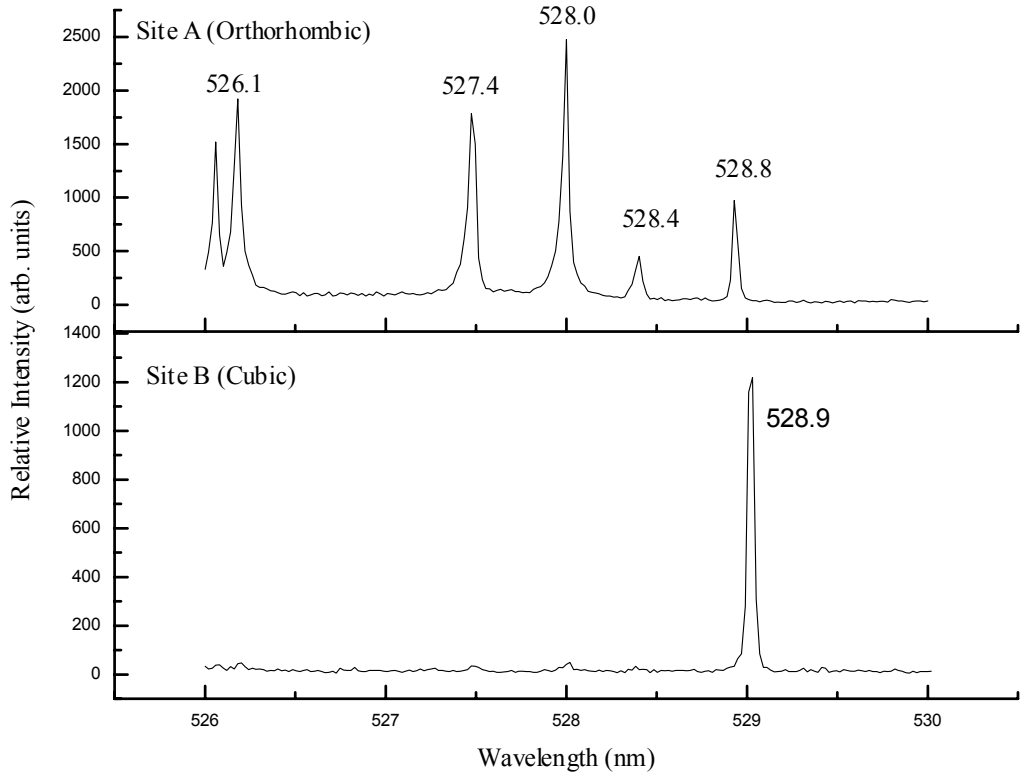

Figure 5-7. Site-selective excitation spectra of 1.1 mol % Eu^{3+}:CaO (#205). The delay and gate for A were 1 μs and 1 ms. For B, the gate and delay were 400 μs and 1 ms. For A site the 1-m monochromator was set to 613.1 nm. For the site B spectrum, the 1-m monochromator was set to 594.1 nm. The scan rate of the dye laser was 0.05 Angstroms/sec, and the laser energy was 280 μJ.

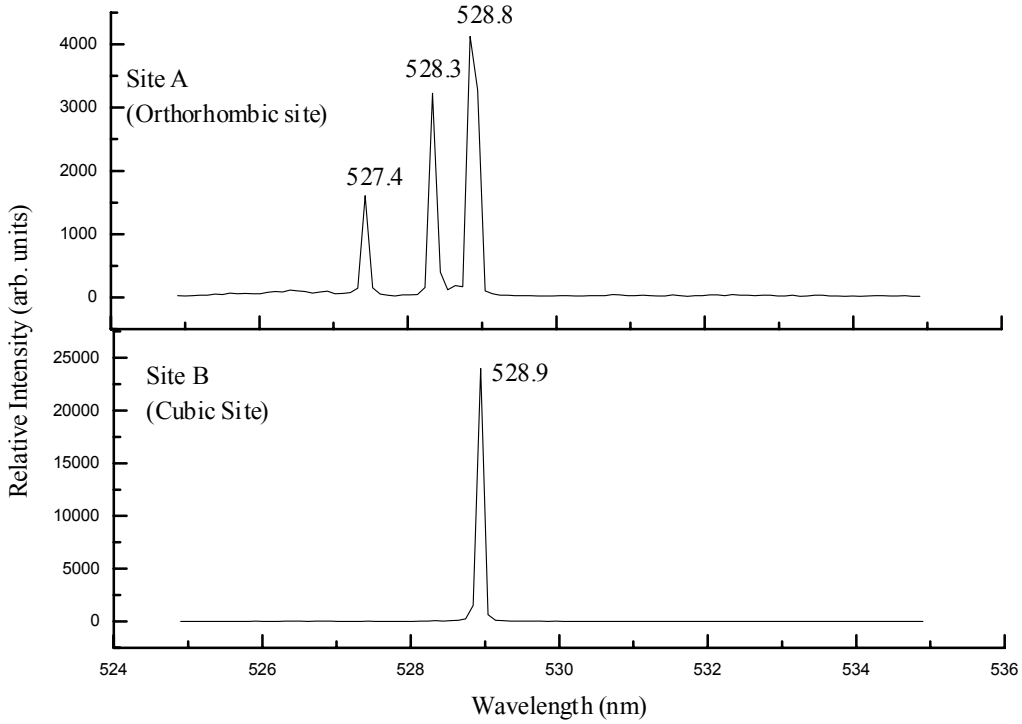

Figure 5-8. $^7F_0 \rightarrow {}^5D_1$ excitation spectra of nanocrystalline 1.5 mol % Eu^{3+}:CaO (#203). The delay and gate for the site A spectrum were 1 and 150 μs, and the delay and gate for the site B spectrum were 400 and 150 μs. To obtain the site A spectrum, the 1-m monochromator was set to 613.3 nm. The spectrum for site B was obtained by setting the 1- m monochromator to 594.1 nm. The scan rate of the dye laser was 0.5 A/sec, and the laser energy was 224 μJ.

The site-selective results for the 8.1 mol % Eu^{3+}:CaO are shown in Figure 5-9. The excitation of site A shows peaks at 527.4 nm, 528.3 nm, and 528.8 nm which correspond to the peaks obtained for site A in the bulk material studied by Porter and Wright[70]. The slight rise in the 526-527 nm region and small hump in the 528-529 region are indicative of the monoclinic Eu_2O_3 phase. The one line at 528.9 nm corresponds to the wavelength of 528.9 nm obtained for site B in the bulk material by Porter and Wright[70]. These results indicate that the 8.1 mol % sample has two phases; cubic Eu^{3+}:CaO and monoclinic Eu_2O_3.

The concentration dependency on the luminescence spectra of nanocrystalline Eu^{3+}:CaO does not show a clear trend with regard to the pre-vaporization dopant concentration and the presence of single-phase material. The spectrum for the sample with the lowest pre-vaporization concentration of dopant (sample 206) showed lines for Eu_2O_3 while some spectra obtained with samples with higher pre-vaporization concentrations do not. These results indicate that the presence of the secondary monoclinic Eu_2O_3 phase in the nanocrystalline samples is not dependent on the pre-vaporization concentration of the dopant but rather is a result of dynamics as the nanocrystals are vaporized. The two photographs shown in Figure 5-10 were taken of the bulk pellet residue that remains after vaporization of Eu^{3+}:CaO with the CO_2-laser. The top photograph shows that there is not uniform vaporization as the pellet slowly rotates on the stage in the vaporization chamber. As a result of the cratering caused by uneven vaporization, sample variability is introduced. This hypothesis is further strengthened by viewing the dark, glassy areas in the residue shown in the bottom photograph. These glassy areas indicate melting of the pellet, which obviously occurs in some regions but

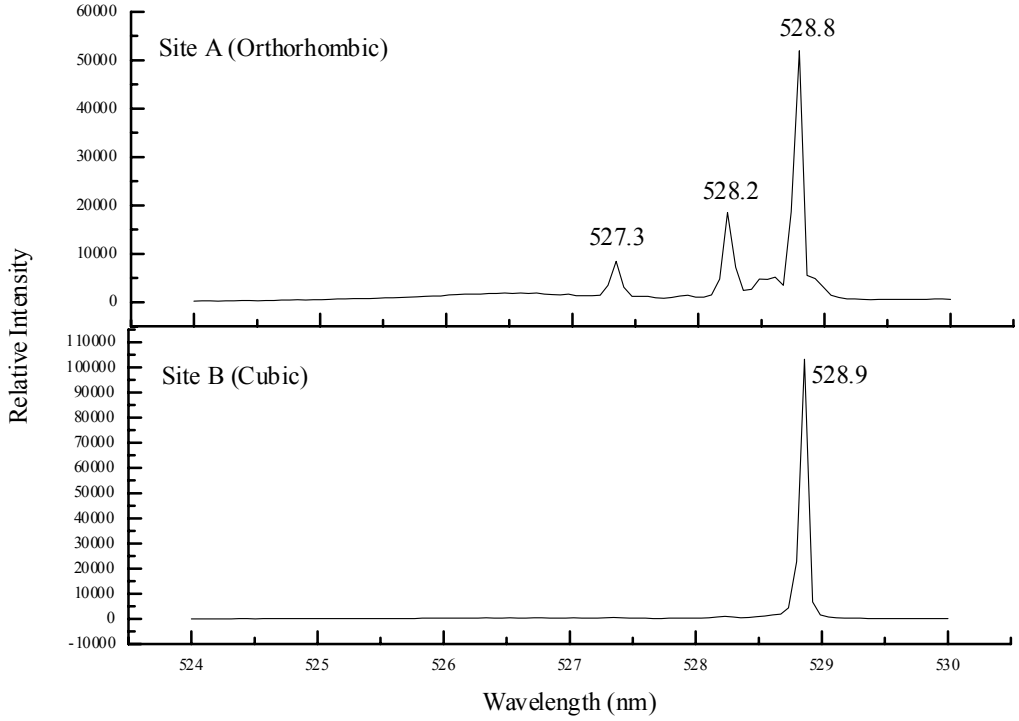

Figure 5-9. $^7F_0 \rightarrow {}^5D_1$ excitation spectra of sites A and B for the nanocrystalline 8.1 mol % Eu^{3+}:CaO. For the A spectrum, the gate and delay were 100 μs and 1 ms and for the B spectrum, the gate and delay were 400 and 150 μs.

Figure 5-10. Photographs taken of Eu^{3+}:CaO residue, after vaporization with the CO_2-laser at 40 Watts, show the inhomogeneous vaporization of the bulk bulk pellets as they rotate on the stage in the vaporization chamber.

not all regions of the pellet during the vaporization process. These results indicate that the laser-vaporization-gas-phase condensation method of preparing the nanocrystalline Eu^{3+}:CaO may result in mixed-phase samples. As a result of the phase distribution study, a study was initiated to determine the effect of annealing on the monoclinic Eu_2O_3 secondary phase that was observed in some of the samples.

5. C. 4. Effect of Annealing on Site-Selective Spectra of Nanocrystalline Eu^{3+}:CaO

Annealing studies of other metal oxide nanocrystals (such as TiO_2) have shown that the particle size will increase upon heating[103] so choosing the annealing parameters was crucial since the goal was to eliminate the Eu_2O_3 phase without significant particle growth. In nanocrystalline TiO_2, the particle size remained unchanged to 600 ^{0}C but rapid particle growth took place above 800 ^{0}C. In an attempt to eliminate the Eu_2O_3 monoclinic phase, the annealing experiment was carried out at 800 ^{0}C.

The nanocrystalline 1.1 mol % Eu^{3+}:CaO (#205) was removed from the desiccator and placed in a Pt crucible. The crucible containing the nanocrystals was placed in a furnace that was pre-heated to 800 ^{0}C. After 30 minutes, the nanocrystals were removed from the furnace and allowed to cool on the desktop until the crucible could be handled. The annealed nanocrystals were placed in the copper sample holder for laser spectroscopy.

Figures 5-11 and 5-12 show the micrographs obtained from TEM experiments on the non-annealed and annealed samples. A survey of the micrographs revealed that the particle size was not significantly affected under these annealing conditions (800 ^{0}C and 30 minutes). The dominant particle size of the non-annealed sample was 13 nm and the dominant particle size for the annealed sample was 14 nm. Since the reproducibility is ± 1 nm, these values are equivalent. A qualitative analysis of the images, which was

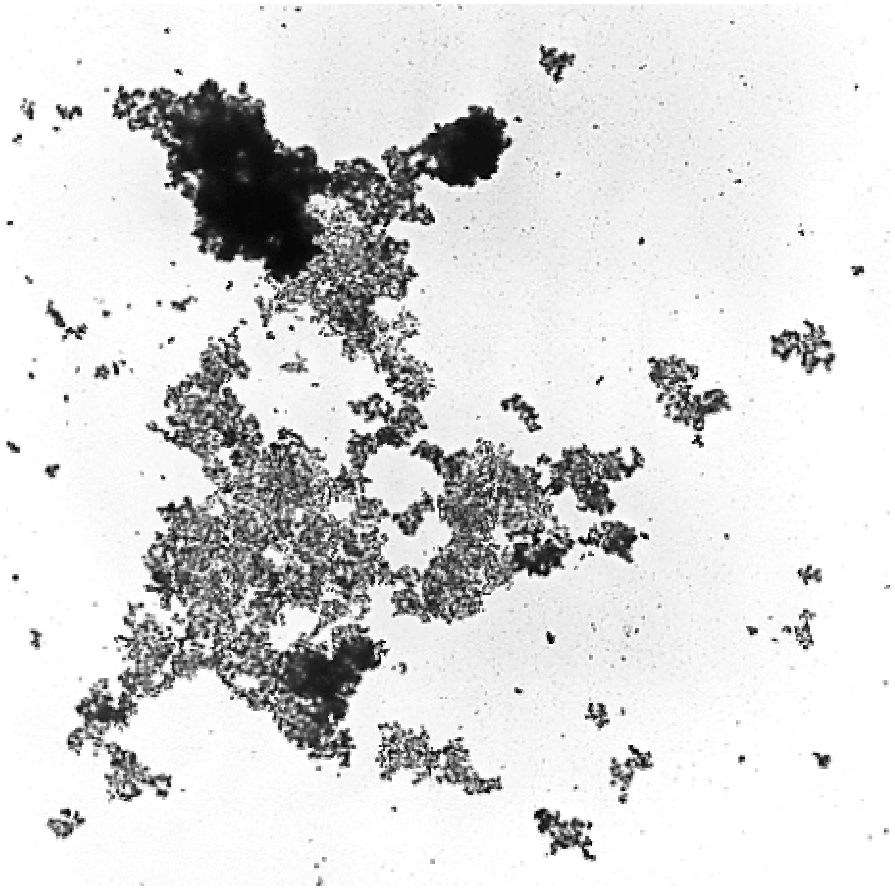

Scale: __ 104 nm

Figure 5-11. Positive of TEM image of non-annealed nanocrystalline 1.1 mol % Eu^{3+}:CaO. The instrument magnification was 6350. The network arrangement is characteristic of nanocrystalline metal oxides prepared by laser-vaporization gas-phase condensation method.

.

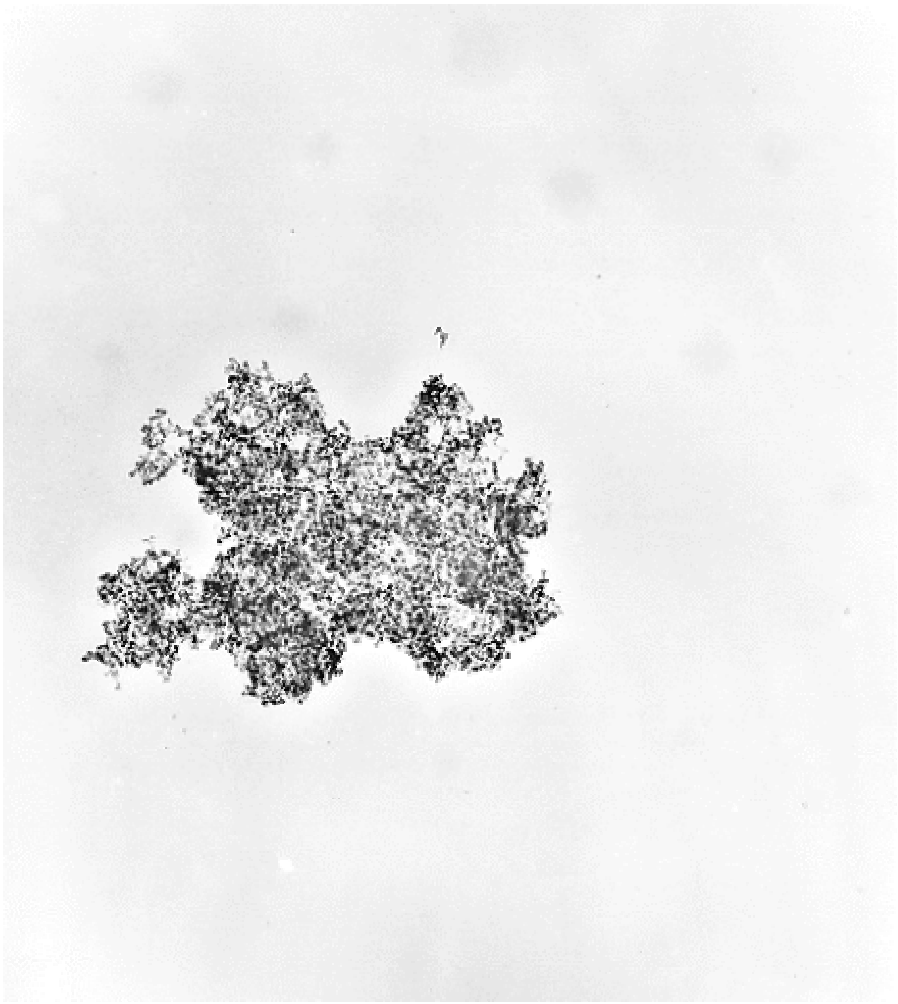

Scale: __ 56 nm

Figure 5-12. Positive of TEM image of annealed nanocrystalline 1.1 mol % Eu^{3+}:CaO. The instrument magnification was 18500.

performed by viewing the images under the electron microscope, revealed that the network array is more condensed after annealing, which indicates a decrease in the porosity of the crystals. Similar results for other nanophase oxides were reported in a review by Siegel [29].

After the sample was annealed, laser spectroscopic measurements were made to determine the degree to which the monoclinic Eu_2O_3 phase was reduced by heating. Figure 5-13 shows the broadband $^7F_0 \rightarrow {}^5D_1$ excitation spectrum obtained using a 0.25-m monochromator with a bandpass of 6 nm. The peaks at 527.4, 528.3, and 528.8 correspond to the wavelengths that were obtained in the study by Porter and Wright [70] for bulk Eu^{3+}:CaO. The broad feature beginning at 526 nm is evident although the intensity has been significantly reduced compared to the non-annealed sample. Excitation of the 526-nn peak revealed a luminescence spectrum, shown in Figure 5-14, that contained the major peak at 624 nm. Although the spectrum has a very low signal-to-noise ratio, the spectrum does provide an indication of the intensity of luminescence at 624 nm. The presence of this peak is indicative of the monoclinic Eu_2O_3 phase because the major emission reported for the monoclinic Eu_2O_3 was 624 nm [73]. This indicates that the annealing did not completely eliminate the monoclinic Eu_2O_3 phase; however, the results of the site-selective excitation for site A, shown in Figure 5-15, indicate that the contribution of the monoclinic Eu_2O_3 in the spectrum is negligible.

5. C. 5. Effect of Annealing on the Cubic/Orthorhombic Ratio

The effect of annealing on the variability of the cubic/orthorhombic ratio of the nanocrystals was evaluated. Figure 5-15 shows the spectra obtained for the non-annealed and annealed 1.1 mol % Eu^{3+}:CaO nanocrystalline sample and Table 5-6 shows the

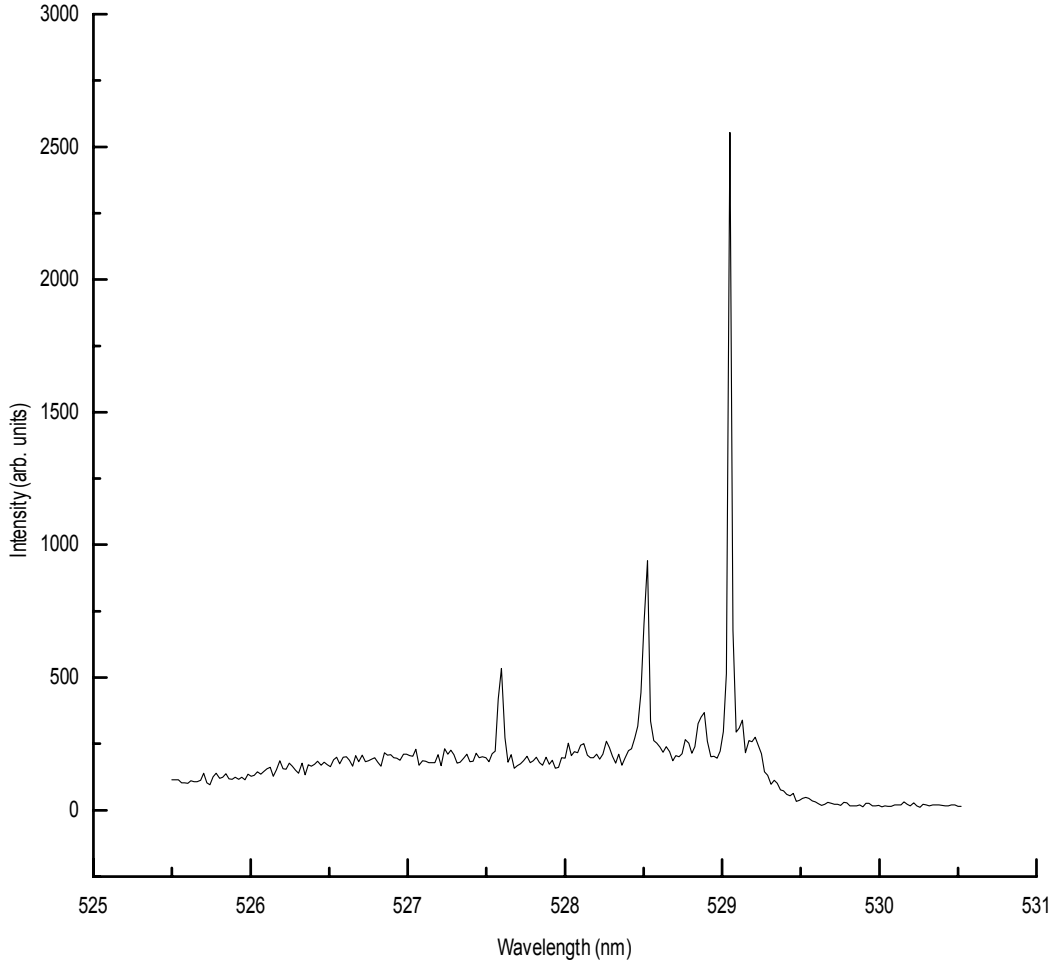

Figure 5-13 . Broadband $^7F_0 \rightarrow {}^5D_1$ excitation of 1.1 % Eu^{3+}:CaO after the sample was annealed for 30 minutes at 800 ^{0}C. The spectrum was recorded using a 0.25-m monochromator with a 6-nm bandpass. The delay and gate were 1 μs and 1 ms, respectively.

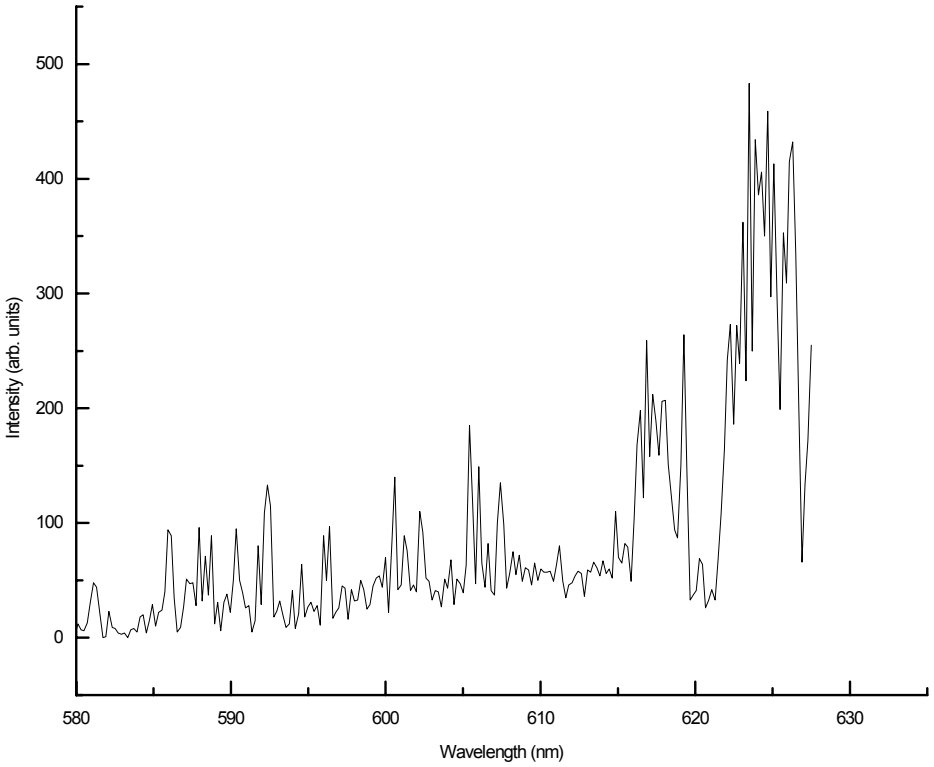

Figure 5-14 . Luminescence spectrum of nanocrystalline 1.1 mol % Eu^{3+}:CaO after 30-minute annealing at 800 ^{0}C. The spectrum was obtained by exciting 528.0 nm and was recorded using a 1-m monochromator with a slit width of 400 μm. The delay and gate were 1 μs and 1 ms, respectively.

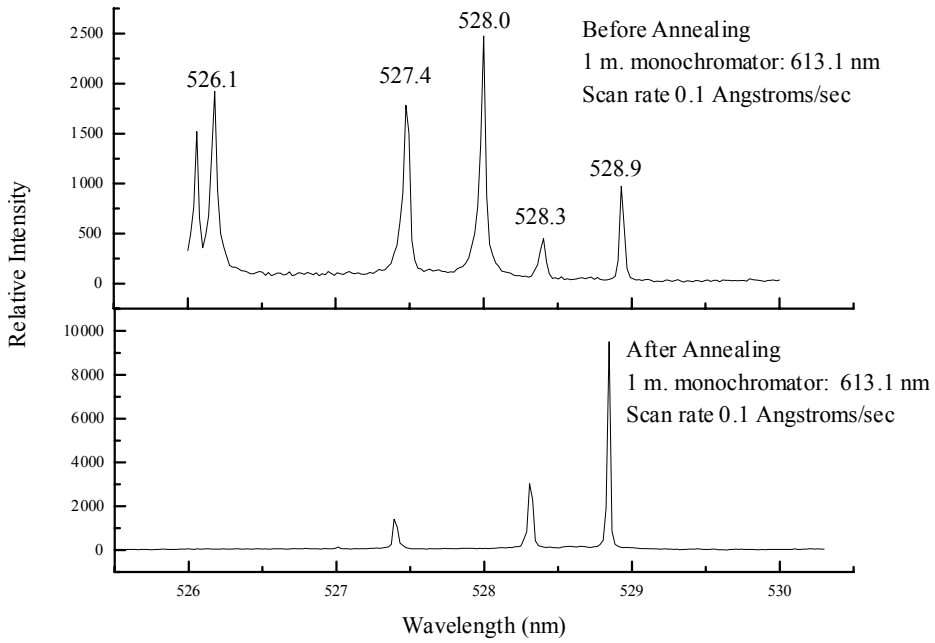

Figure 5-15. $^7F_0 \rightarrow {}^5D_1$ site-selective site A excitation of non-annealed and annealed 1.1 mol % Eu^{3+}:CaO using a 1-m monochromator set at 613.1 nm. The delay and gate were 1μs and 1 ms, respectively.

variation in the cubic/orthorhombic ratios as a function of annealing. The results from the annealing experiment indicate that the cubic/orthorhombic ratio was 0.40 prior to annealing and 1.9 after annealing, which indicates a variation of 79 % in the ratios. Therefore, the dopant distribution in annealed nanocrystalline materials cannot be directly compared to non-annealed samples.

According to the literature, annealing can affect the particle size distribution in nanocrystalline materials[104]. Bhargava[104] and co-workers suggest that annealing can lead to bulk-like optical spectral features. The annealing results are significant because they are consistent with the supposition made by Bhargava. The spectrum of the annealed sample clearly shows the reduction in the monoclinic Eu_2O_3 phase and the bulk-like optical features obtained in the bulk material studied by Porter and Wright[70]. The site selective spectrum of site A in the annealed sample shows lines at the same wavelengths as the bulk material. Likewise, the site selective spectrum of site B shows a single line at the same wavelength as the single line in the spectrum for the bulk material. The results indicate that nanocrystalline Eu^{3+}:CaO can be prepared by the laser-vaporization-gas-phase condensation and unstable phases can be removed by annealing.

To determine the percentage reduction in the presence of the metastable monoclinic Eu_2O_3 in the sample by annealing, the relative intensities of the line at 528.0 nm were compared in the annealed and non-annealed spectrum. This line was chosen because it does not appear in the spectrum of Eu^{3+}:CaO, which means that the line at 528.0 nm is due to the monoclinic Eu_2O_3. The intensity of the line at 528.0 nm was 2490 in the non--annealed spectrum and 102 in the annealed spectrum. The percentage difference in the intensities of the line at 528.0 nm was 96%, indicating that annealing removed the

Table 5-6. Variation of cubic/orthorhombic ratio as a function of annealing. The sample was 13-nm 1.1 mol % Eu^{3+}:CaO.

Date	527.4-nm peak intensity	528.3-nm peak intensity	528.8-nm peak intensity	528.9-nm peak intensity
Non-annealed	1762	515	987	1290
Annealed	1524	3216	9843	27365
Variation	14 %	84 %	90 %	95 %

monoclinic Eu_2O_3 phase by 96 %.

5. C. 6. Analysis of Spectral Line Intensities

The relative peak height intensities in the optical spectra of the nanocrystalline samples were obtained and compared to the results obtained with bulk Eu^{3+}:CaO by Porter and Wright[70]. The results of the peak height measurements and the relative peak height intensities of the nanocrystalline samples are summarized in Table 5-7. To obtain the ratios, the data were normalized by dividing each peak by the most intense peak in the spectrum.

The data show that the two samples that are single phase (cubic Eu^{3+}:CaO) have the greatest similarity in peak height intensity ratios and show a correlation to the relative peak height intensity ratio obtained by Porter and Wright. Porter and Wright's spectral peak height intensity ratios for a bulk sample with a dopant concentration of 0.033 mol % Eu were 0.3 : 0.5 : 1. The single-phase data shown in Table 5-6 were averaged and the relative peak height ratio was determined to be 0.3 : 0.65 : 1. These results indicate that the variation in the relative peak height ratio of nanocrystalline and bulk material is approximately 30 %.

The variation in the peak height intensities of the mixed-phase samples is attributed to the fact that there two Eu-containing phases present. The spectral line intensities vary because the Eu^{3+} ions can be distributed among the two phases and this distribution would be expected to change as the concentration of the dopant changes.

5. C. 7. Effect of Scan Rate on the Cubic/Orthorhombic Ratio

Site-selective data can be used to determine the cubic/orthorhombic ratio and therefore the dopant distribution, as demonstrated by Porter and Wright with the bulk Eu^{3+}:CaO[70].

Table 5.7 Relative peak height intensities and relative peak height intensity ratios of nanocrystalline Eu^{3+}:CaO.

Sample # / concentration of Eu (mol %)	Phases Present	Peak Height Intensity at 527.4 nm (cm)	Peak Height Intensity at 528.3 nm (cm)	Peak Height Intensity at 528.8 nm (cm)	Relative Peak Height Intensity Ratios (in order of 527.4, 528.3, and 528.8)
206 / 0.22 mol % Eu	Cubic Eu^{3+}: CaO and monoclinic Eu_2O_3	1.1	0.8	1.9	0.6 : 0.4 : 1
204 / 0.27 mol % Eu	Cubic Eu^{3+}: CaO	0.9	2.6	4.1	0.2 : 0.6 : 1
205 / 1.1 mol % Eu	Cubic Eu^{3+}: CaO and monoclinic Eu_2O_3	2.4	0.5	1.2	1 : 0.2 : 0.5
203 / 1.5 mol % Eu	Cubic Eu^{3+}: CaO	1.3	2.5	3.4	0.4 : 0.7 : 1
133 / 8.1 mol % Eu	Cubic Eu^{3+}: CaO and monoclinic Eu_2O_3	0.5	1.0	3.0	0.2 : 0.3 : 1

With this goal in mind, further laser spectroscopy experiments were performed to determine how the scan rate would affect the cubic/orthorhombic ratios. To determine how the intensity values may vary with scan rate, spectra were taken using different scan rates to determine the error in the measurements. Other parameters, such as laser intensity and slit width were kept constant. The data that were obtained for the 0.27 mol % Eu^{3+}:CaO sample are shown in Table 5-8.

To determine the overall cubic/orthorhombic ratio from the data shown in Table 5-8, the peak intensity of the B site (cubic) line at 528.9 nm was divided by the sum of the peak intensities of the A site (orthorhombic) lines at 527.4, 528.3, and 528.8 nm. The result of this calculation was a ratio of 6.1 for the 0.1 Angstroms/sec scan and 4.9 for the 0.5 Angstroms/sec scan. Therefore, the percent variation in the ratios is approximately 20 %.

The relative percentage error in the peak intensity measurements are shown in Table 5-8. The data show that the peak intensities can vary to approximately 30 %.

5. C. 8. Determination of Dopant Distribution in Single-Phase, Non-Annealed Nanocrystalline Eu^{3+}:CaO

Since the laser-vaporization-gas-phase condensation method of preparing the nanocrystalline Eu^{3+}:CaO resulted in mixed-phase materials in some cases, only the samples that were single-phase and non-annealed were used for the dopant distribution study.

The data presented by Porter and Wright[70] for bulk Eu^{3+}:CaO showed that at high dopant concentration (>0.002 mol % Eu), the ratio of cubic/orthorhombic sites remain

Table 5-8. Variation in peak intensity with scan rate for nanocrystalline 0.27 mol % Eu^{3+}:CaO.

Scan Rate Å/sec	Laser Energy μJ	527.4-nm peak intensity	528.3-nm peak intensity	528.8-nm peak intensity	528.9-nm peak intensity
0.1	280	20	55	89	1000
0.5	280	29	66	92	923
Variation		31 %	16 %	3 %	8 %

independent of concentration. The results that were obtained for the nanocrystalline samples suggest that the ratios are not independent of concentration. The cubic/orthorhombic ratios were determined by taking the relative intensity of the site B (cubic) line and the relative intensities of the site A lines (orthorhombic) from the site-selective spectra. Table 5-9 correlates the dopant concentration and cubic/orthorhombic ratios for the single-phase non-annealed nanocrystalline samples.

The data that are shown in Table 5-9 cannot be compared as absolute values because multiple measurements are needed to provide a reasonable assumption for the variability of sample 203. If one assumes that the variation in sample 203 is similar to the 30 percent variation observed for sample 204, then one could speculate that the ratios of the two single-phase nanocrystalline samples show a minimum variation of 17 % and a maximum variation of 76 %. Since the experimental ratios are not conclusive, a model to predict the dopant distribution (defect chemistry) was developed.

To predict the defect behavior for the nanocrystals, one must consider the role that the increased surface area might play on the defect chemistry in nanocrystals. The orthorhombic site corresponds to an associated pair where a V''_{Ca} compensates a $Eu^{\bullet}_{Ca}$ in the nearest neighbor position along the [100] axis[70]. A representation of the [100] axis in calcium oxide is represented in Figure 5-17. According to Henrich and Cox[105], the ideal geometry of the (100) surface is unambiguous since the bulk structure consists of layers of atomically flat planes that are composed of equal numbers of cations and anions. Figure 5-18 represents the [100] axis in calcium oxide with a europium substitution.

Recall that the extrinsic defect created by doping CaO with Eu^{3+} is a calcium vacancy. If the dopant concentration is held constant and the particle size is reduced, then one

Table 5-9. Cubic/Orthorhombic ratios for single-phase non-annealed nanocrystalline Eu^{3+}:CaO. The percent variation shown for the value of 5.8 was obtained by using the largest variation observed for this sample.

Sample #	Eu concentration (mol %) and percent error	Cubic/Orthorhombic Ratio
203	*	2.6
204	*	6.5 6.1 4.8 Average: 5.8 ± 30 %

* not conclusive due to undetermined error

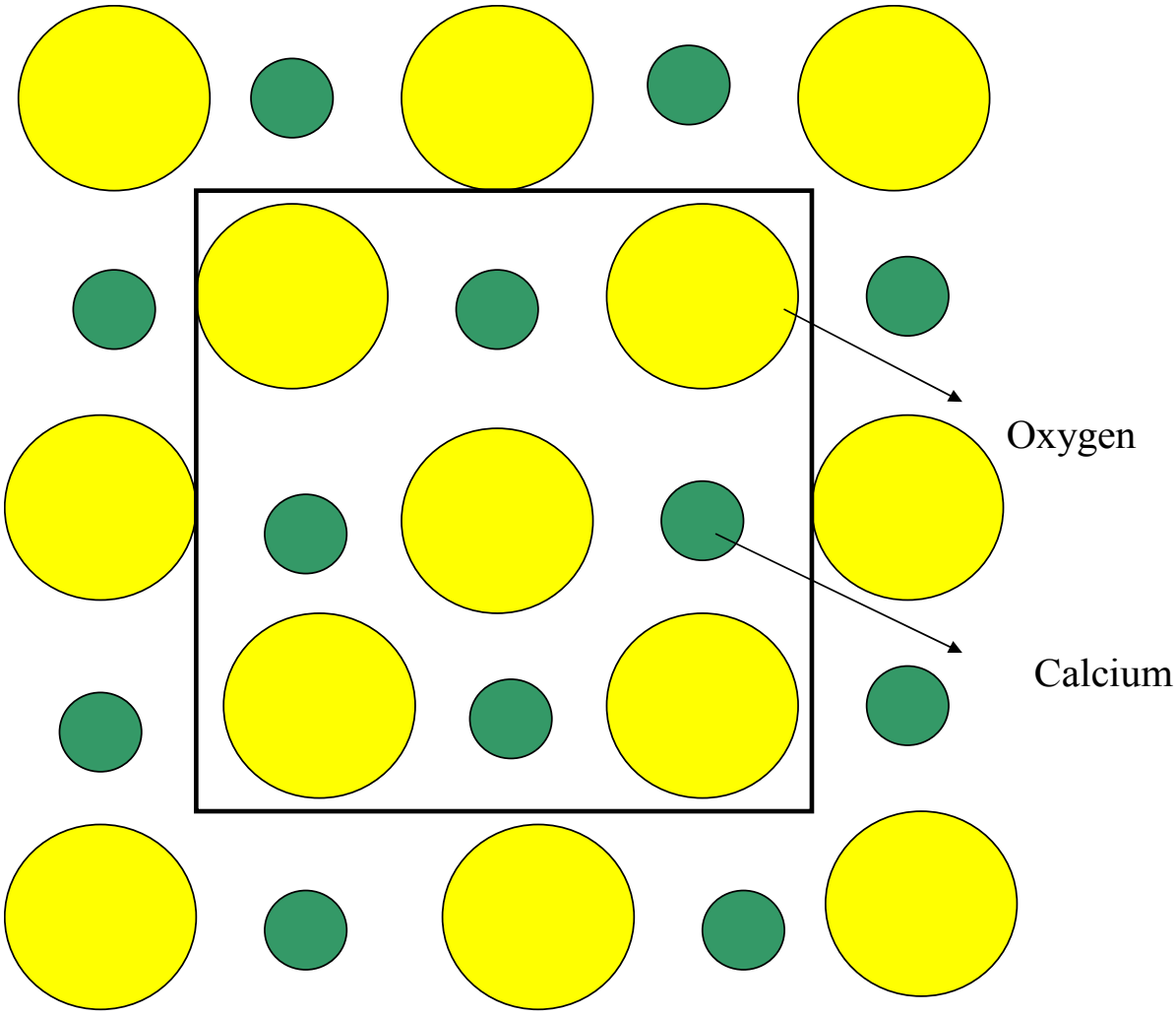

Figure 5-16. Representation of the [100] axis in calcium oxide. The unit cell is outlined.

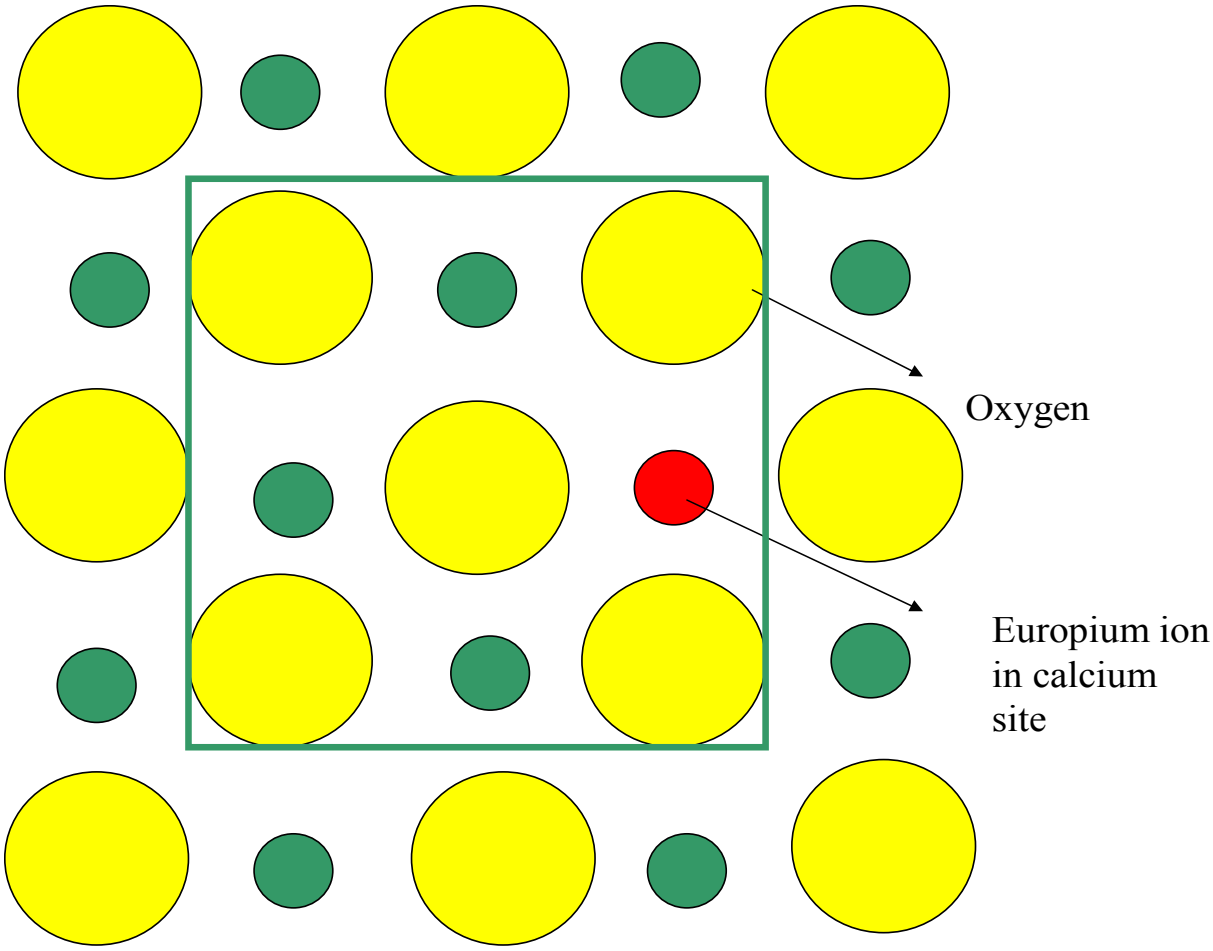

Figure 5-17. Representation of the [100] axis in calcium oxide. The unit cell is outlined. The red circle represents a europium ion in a calcium site ($Eu^{\bullet}_{Ca}$). The pairing of a Eu^{3+} with a calcium vacancy(V''_{Ca}) in a nearest neighbor position is referred to as the orthorhombic site (A site)[70].

would expect the defect chemistry in nanocrystals to differ from the bulk because it has been suggested that cation vacancies may migrate to the surface[106].

5. C. 9. Prediction of the Dopant Distribution (Defect Chemistry) in Nanocrystalline Eu^{3+}:CaO

To study the dopant distribution in the nanocrystals, the increased surface was considered. As shown in Figure 3-7, the vast majority of ions in the bulk material are in the interior of the particle, not on the surface and therefore, the majority of the signal being detected in the bulk material is coming from ions that have their full complement of lattice components. In the nanocrystals, more of the signal is coming from ions at the surface.

The face-centered cubic structure of calcium oxide is shown in Figure 5-18. The ionic radius of Ca^{2+} is 1.14 Å and the ionic radius of oxygen is 1.26 Å[105]. Since the surface thickness is assumed to be 0.5 nm, the surface contains approximately 3 atomic planes.

To predict how the dopant distribution (defect chemistry) will change in the nanoparticles with reduced particle size, information from the literature regarding bulk Eu^{3+}:CaO[70] as well as information regarding the surface chemistry of doped MgO were used[107]. Magnesium oxide was chosen because it is isostructural with CaO[3]. For simplification, the data that were used to determine the defect chemistry of bulk Eu^{3+}:CaO are summarized in Table 5-10. The theoretical fit was obtained using the equations previously introduced on page 78, and using $K_p = 3000$ and $K_i = 10^{-10}$, where K_p represents the constant for pairing defect equilibria and K_i represents intrinsic defect equilibria[70]. Although the value published for K_p was 3000, this is assumed to be a

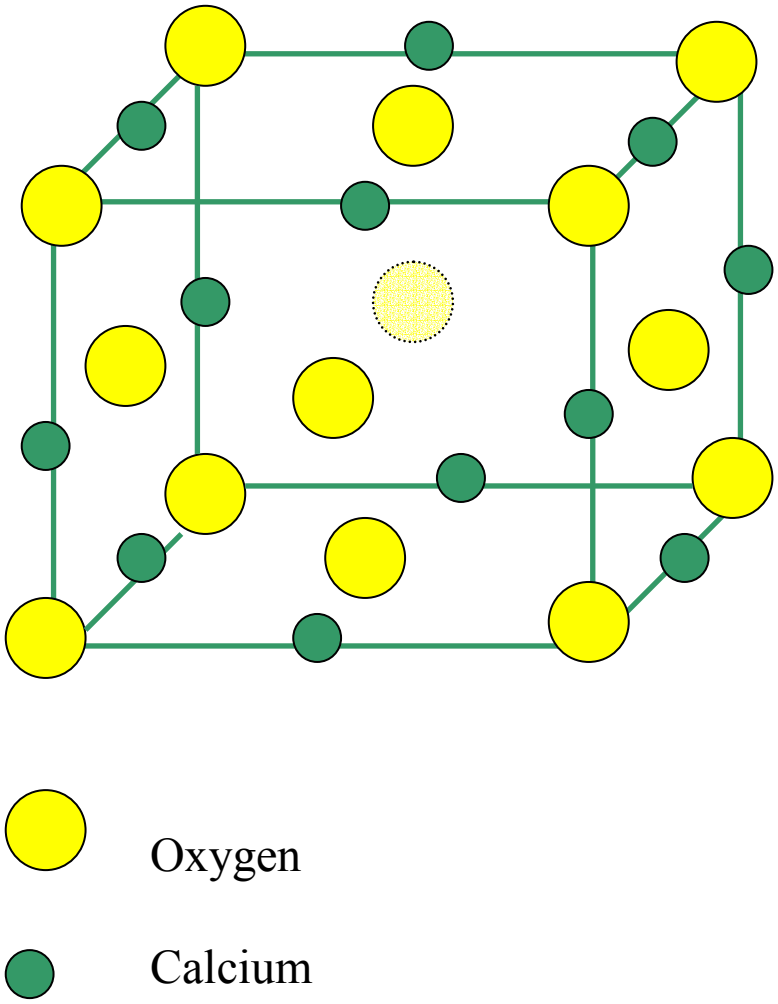

Figure 5-18. Representation of face-centered cubic CaO^3

typographical error because the data from the corresponding graph indicate that a K_p value of 5000 was used. All concentrations in the table are approximate because the data were taken from reading a graph.

The data in Table 5-10 show that at high dopant concentrations, the ratio of the cubic/orthorhombic sites remains independent of concentration. At low concentrations, the orthorhombic site (pairing site) becomes much less important than the cubic site[70].

To determine the role of the surface on the defect chemistry of the nanocrystalline system, the data obtained from studies on doped MgO were used to make a correlation between vacancies at the surface in bulk versus vacancies at the surface in the nanocrystals.

The structure, surface, and catalytic properties of bulk MgO doped with Al^{3+} has been reported[106]. Since MgO is isostructural with CaO, this system can be used to predict how Eu^{3+}:CaO might behave. For all samples studied (Mg/Al molar ratios of 0.5-9.0), the powder X-ray diffraction results did not show any Al_2O_3 phases[106], which indicates that the Al^{3+} ion was incorporated into the MgO lattice. The surface composition of the samples was measured by X-ray photoelectron spectroscopy (XPS) and total surface areas were measured using a sorptometer and BET analysis methods[106]. Bulk elemental analysis of Mg and Al was carried out by atomic absorption spectroscopy (AAS)[106]. Another paper that was useful for predicting how the increase in the surface might affect the defect chemistry of Eu^{3+}:CaO was one regarding the reaction of SO_2 with pure and metal-doped MgO by Rodriguez and co-workers[107].

Using the information provided in the two referenced papers on MgO, the paper on the

Table 5-10. Data obtained from Porter and Wright's paper on the defect chemistry of bulk Eu^{3+}:CaO[70].

Eu concentration (mol %)	Cubic/Orthorhombic ratio and reported error
0.02	1 ± 15 %
0.006	1 ± 15 %
0.001	2 ± 15 %
0.0006	4 ± 15 %
0.0003	4 ± 15 %
0.0001	7 ± 15 %
0.00006	12 ± 30 %
0.00003	14 ± 30 %

defect chemistry of bulk Eu^{3+}:CaO by Porter and Wright[70] and basic principles of defect chemistry[3,105,108], the following assumptions were developed to predict how the reduction in particle size would affect the defect chemistry in nanocrystalline Eu^{3+}:CaO.

Assumptions:

1. Eu is evenly distributed in the nanocrystals.

2. Dopant concentration is assumed to be 0.0006 mol %. This dopant concentration was selected because the calcium vacancy concentration for this dopant concentration is known from studies of bulk Eu^{3+}:CaO[70], (0.0014 mol %).

3. Surface depth is 0.5 nm (approximately three atomic layers for CaO). The use of 0.5 nm is consistent with the literature[107].

4. $K_p = 5000$; $K_p = [(Eu_{Ca} \bullet V_{Ca})'] / [Eu\bullet_{Ca}] [V''_{Ca}]$

5. $K_i = 10^{-10}$; $K_i = [V''_{Ca}] [V^{\bullet\bullet}_O]$

6. The only extrinsic defect created by doping CaO with Eu^{3+} is the calcium vacancy[3,109].

7. The volume fraction of total ions on the surface of nanocrystalline Eu^{3+}:CaO was calculated using: $\{[4/3\pi r^3 - 4/3\pi(r-\delta)^3] / 4/3\pi r^3\} \times 100$

where δ is the assumed surface thickness of 0.5 nm and r is the particle radius. For example, in bulk CaO, the volume fraction of total ions at the surface is 2 %. This percentage was determined by assuming a particle diameter of 100 nm since materials at 100 nm are assumed to have bulk properties.

8. The crystal lattice at the surface is different from the crystal lattice in the interior due to the difference in nearest neighbors. The number of nearest neighbors in calcium oxide is 8 at the surface and 12 in the interior.

9. Luminescence is detected from both interior and surface ions.

To predict how the particle size would affect the cubic/orthorhombic ratio, the equations and assumptions presented in the preceding paragraphs were used. Specifically, the vacancy concentration was varied as a function of particle size by subtracting the vacancy concentration at the surface from the total vacancy concentration. Therefore, by changing the vacancy concentration as a function of particle size and keeping $K_p = 5000$, the cubic/orthorhombic ratio could be estimated. The equations used are shown below and a chart of the results is shown in Figure 5-20.

Equation 1: $4/3\ \pi\ r^3\psi_i$, where r is particle radius and ψ_i (number of atoms per unit cell for interior CaO lattice) = 4.

Equation 2: $4/3\ \pi\ (r-\delta)^3\psi_s$, where δ is the assumed surface thickness of 0.5 nm and ψ_s (number of atoms per unit cell for surface lattice) = 1.

Equation 3: Equation 1-Equation 2

Equation 4: Equation 3/Equation 1

Equation 5: Calcium vacancy concentration * Equation 4

(Note: Calcium vacancy concentration is a function of dopant concentration and can be calculated if the dopant concentration is known. The calcium vacancy concentration does not include the intrinsic concentration because it is considered negligible compared to the extrinsic concentration[3].)

Equation 6: Calcium vacancy concentration – Equation 5

Equation 7: Result of Equation 6 * K_p

The model in Figure 5-20 predicts that the defect chemistry is affected when the particle diameter is approximately 50 nm. As the particle size decreases (and the surface area increases), the cubic/orthorhombic ratio decreases. The decrease in the ratio

suggests that increasing the surface area results in fewer europium ions in a cubic symmetry site. This prediction is reasonable because ions on the surface lack their full complement of nearest neighbors.

Work done by Suyver and co-workers[110] lends support to the model shown in Figure 5-20. Suyver and co-workers performed simulations to predict the probability of dopants residing in nearest neighbor positions in a FCC nanocrystalline structure. The simulations were performed assuming an even distribution of the dopant ions. The conclusion reached by Suyver and co-workers:

> The fact that lattice positions on the surface have only 8 neighbors, instead of the usual 12 for bulk lattice positions, results in a drastic increase in the probability for pair formation compared to larger crystals.

Therefore, the prediction that the cubic/orthorhombic ratio decreases as the particle size decreases suggests that the surface in nanocrystalline materials has a significant effect on the dopant distribution in these materials.

Since the model shown in Figure 5-20 includes a concentration dependency, the particle size can be held constant at 13-nm and the dopant concentration can be varied to predict how the ratios would change as the europium concentrations change. The results are shown in Figure 5-21.

The model shows that an increase in the dopant concentration in a 13-nm sample leads to a decrease in the pairing of the europium ion and its corresponding calcium vacancy. The predicted increase in the cubic/orthorhombic ratio with dopant concentration in the 13-nm sample can rationalized by recalling that the orthorhombic site is the site in which a V''_{Ca} compensates a $Eu^{\bullet}_{Ca}$ in the nearest neighbor position along the [100] axis. Increasing the dopant concentration does not necessarily increase the pairing behavior at

"high" dopant concentrations because it has been speculated that vacancies may migrate to the surface[106]. If the calcium vacancies are migrating to the surface, then the Eu^{3+} ions in the interior of the particle have a lower probability of pairing with the vacancy in the nearest neighbor position. At a dopant concentration of 0.0006 mol %, the $[V_{Ca}''']$ is 0.0014 mol %, according to Porter and Wright[70]. In a 13-nm particle, the total number of ions can be calculated from the following:

Volume of a sphere: $4/3\ \pi\ r^3$ where r is the particle radius

Density = 3.4 g/cm^3 (The density of the host lattice was used since the majority of ions are from the host.)

Formula mass of CaO: 56 g/mol

$$\frac{4}{3}\pi\,(6.5 \times 10^{-7}\ cm)^3 \times \frac{3.4\ g}{cm^3} \times \frac{1\ mol}{56\ g} \times \frac{(6.022 \times 10^{23}\ molecules)}{mol} \times \frac{2\ ions}{molecule} = ions$$

The total number of ions in a particle with a particle diameter of 13 nm was determined to be 83,865 ions. Since the volume fraction of surface ions in a 13-nm particle is 22 %, the total ions in the interior is 65,414 and the total at the surface is 18,451. Calculations were performed assuming that 50 % of the total calcium vacancies migrate to the surface to predict how the migration would affect the number of calcium vacancies and europium 13-nm particle. The results of the calculations are shown in Table 5-11.

For the 0.0006 mol % Eu^{3+} sample, the ratio of europium ions to calcium vacancies is roughly 1:1 in the interior, while the ratio was 1:8 at the surface. For the 0.02 mol % Eu^{3+} sample, the ratio was 18:1 in the interior and 2:1 at the surface. Therefore, raising the dopant concentration results in a reduction in dopant and vacancy pairing due to the migration of calcium vacancies to the surface. This assertion can be made because the

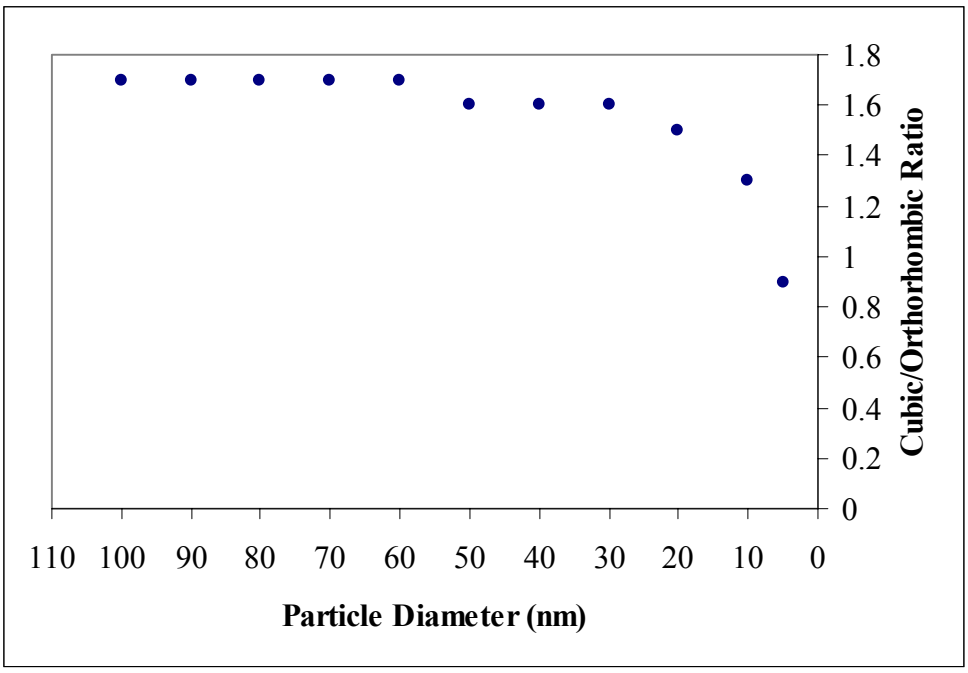

Figure 5-19. Theoretical variation of the cubic/orthorhombic site ratio as a function of particle size. The ratios were determined by using $K_p = [(Eu_{Ca} \bullet V_{Ca})'] / [Eu\bullet_{Ca}] [V''_{Ca}]$, where $K_p = 5000$ and the calcium vacancy concentration varied with particle size.

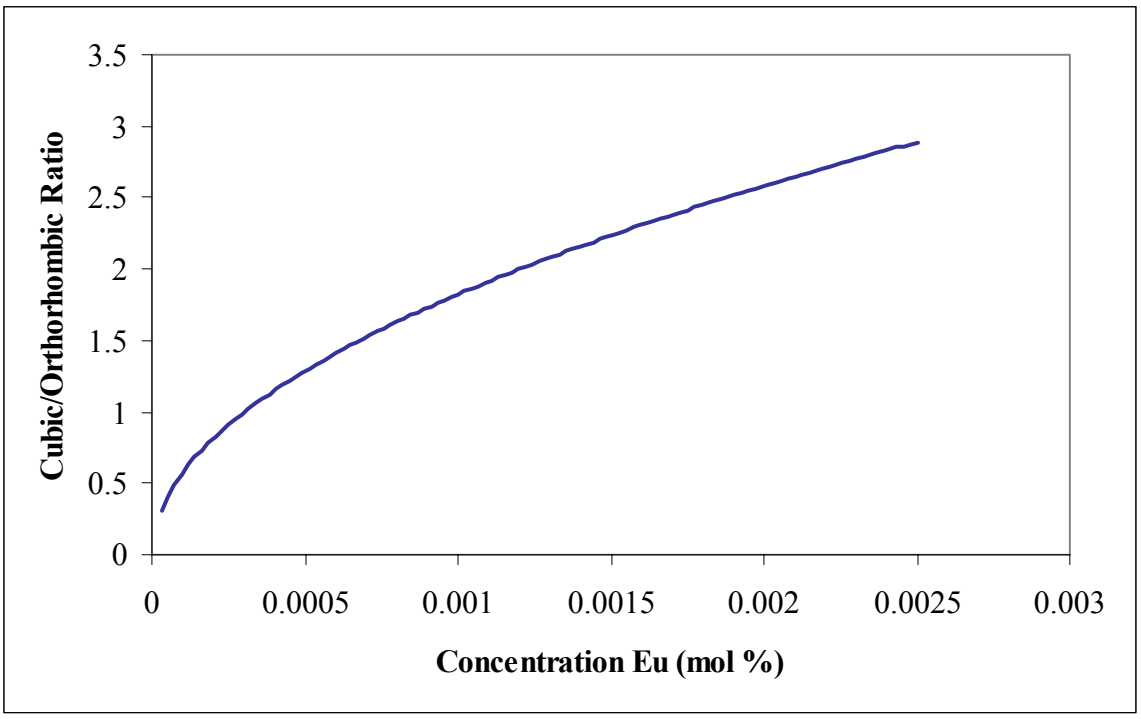

Figure 5-20. Theoretical variation of the cubic/orthorhombic ratio of a 13-nm sample as a function of dopant concentration.

ratio of 18:1 means that there are many more europiums than vacancies in the interior, which would result in more europiums in a cubic site instead of a pairing site (orthorhombic). Roughly 78 % of the luminescence detected comes from the interior in 13-nm particles, while 22 % comes from the surface (from calculations shown in Table 3-7). Therefore, raising the dopant concentration results in a lower chance of a Eu^{3+} ion being in a nearest neighbor position to a calcium vacancy.

Table 5-11. Results of calculations to determine the correlation between surface species versus interior species in a 13-nm sample of Eu^{3+}:CaO.

$[Eu^{3+}]$ mol %	$[V_{Ca}'']$ mol %	Number of Eu^{3+} ions at surface	Number of Eu^{3+} ions in interior	Number of V_{Ca}'' at surface	Number of V_{Ca}'' in interior
0.0006	0.0014	0.11	0.39	0.84	0.32
0.02	0.003	3.7	13.1	1.8	0.7

.

5. D. Summary of Conclusions

This initial survey of the structure, luminescence, and defect chemistry of nanocrystalline Eu^{3+}:CaO has revealed some interesting phenomena. The phase distribution studies of nanocrystalline Eu^{3+}:CaO revealed the appearance of the metastable monoclinic Eu_2O_3 phase in some samples. Although one would predict that the appearance of the phase would increase with increasing europium concentration, this trend was not observed. The appearance of the metastable monoclinic Eu_2O_3 phase in some of the nanocrystalline Eu^{3+}:CaO samples but not others is assumed to be due to inconsistent vaporization as a result of crater formation during the laser-vaporization-gas-phase condensation process. It is speculated that the formation of craters in the pellet causes the laser beam to spread, resulting in uneven vaporization temperatures.

The annealing experiment showed that the monoclinic Eu_2O_3 phase was reduced by 96 % and the annealing conditions used did not result in particle growth. The site-selective spectrum for site A in the non-annealed 1.1 mol % sample showed that the majority of the signal being detected was coming from the monoclinic Eu_2O_3 phase. After annealing the 1.1 mol % sample, the site-selective site A spectrum clearly shows that the presence of Eu_2O_3 in the spectrum is negligible.

These initial site-selective luminescence measurements performed on nanocrystalline Eu^{3+}:CaO revealed that the relative peak intensities varied with scan rate. However, the percent variation of the overall cubic/orthorhombic ratio was within the range reported by Porter and Wright for the bulk samples[70].

The data presented by Porter and Wright[70] for bulk Eu^{3+}:CaO showed that at high dopant concentration (>0.002 mol % Eu), the ratio of cubic/orthorhombic sites remains

independent of concentration while the data obtained for the nanocrystalline materials suggest that the cubic/orthorhombic ratios may vary even at high dopant concentration. To account for these differences, the increased surface area of the nanocrystalline materials was considered. The threshold particle diameter at which the surface area affects the defect chemistry was determined to be 60 nm. The model predicted that the increase in the surface area leads to a decrease in the cubic/orthorhombic ratio. The model was also used to predict the change in the cubic/orthorhombic ratio by increasing the concentration and keeping the particle diameter constant.

5. E. Suggestions for Future Work with Nanocrystalline Eu^{3+}:CaO

For future studies on nanocrystalline Eu^{3+}:CaO, the following considerations are suggested.

The results indicated that the increased surface area in the nanocrystals resulted in an increased reactivity with carbon dioxide and water. If the nanocrystals are not kept in a desiccator after preparation, then laser spectroscopic studies are not feasible because the fluorescence is quenched by the formation of $Ca(OH)_2$ and $CaCO_3$. The increased reactivity of the nanocrystals is also problematic if X-ray diffraction studies are desired. X-ray diffraction studies were attempted with nanocrystalline Eu^{3+}:CaO but the resulting diffraction patterns were characteristic of those for amorphous materials. For future studies, placing the samples in a desiccator immediately after preparation may allow an X-ray diffraction pattern to be obtained.

For TEM studies, it is crucial to obtain the micrographs within a few days of preparation so that crystallinity is preserved. A TEM study was performed on "old" nanocrystals (approx. one month) and a select area diffraction pattern was attempted. A

select area diffraction pattern was not obtained, which indicated that the nanocrystals had become amorphous.

Using laser-vaporization-gas-phase condensation to prepare nanocrystals with significantly different melting points can result in mixed phases because the material with the lower melting point is selectively vaporized. To minimize the formation of mixed phases, it is recommended that a laser output of higher than 40 Watts be used when preparing Eu^{3+}:CaO by this method. However, at higher laser outputs, pellet breakage may become a more severe problem. It is common to have pellet breakage at 40 Watts.

For concentration studies, one must consider the effect that crater formation during vaporization may have on the outcome. If vaporization is not uniform, then the post-vaporization concentrations will likely be inconsistent. For a rigorous concentration study, multiple samples should be prepared using the same experimental conditions in order to obtain the concentration and standard deviation. Based on the observations that were made for this study, it is speculated that this laser-vaporization-gas-phase condensation method to prepare nanocrystalline metal oxides may not give reproducible concentration results, due to the differences in melting point between the oxides.

For luminescence studies, it is recommended that spectra be collected within a few days of preparation. In addition, the scan rate, laser energy, and slit widths should be kept constant to minimize changes in peak intensity.

To determine the reproducibility of the spectra, it is suggested that additional experiments on single-phase samples be performed. For example, an experiment to determine the variability of the signal as a function of time can be performed. The purpose of the experiment is to determine if the signal decreases over time due to

photobleaching, which is the depletion of the ground state population by the laser. This experiment was attempted for this nanocrystalline study but was not included with the spectroscopic data because the sample was not a single-phase sample. A reasonable method to correct for photobleaching would be to record a spectrum for site B, record a spectrum for site A, then record another spectrum for site B so that the average peak intensity for site B can be determined.

Although many questions regarding nanocrystalline Eu^{3+}:CaO remain, this study has revealed the following:

1. Nanocrystalline Eu^{3+}:CaO has been made by the laser-vaporization-gas-phase condensation method. Nanocrystalline Eu^{3+}:CaO has not been reported in the literature.

2. Nanocrystalline Eu^{3+}:CaO does exhibit luminescence when excited by the proper wavelength.

2. Although the increased surface area in the nanocrystals results in accelerated reactivity with CO_2 and H_2O, crystallinity can be maintained for several weeks by keeping the samples in a desiccator.

3. Site-selective spectra revealed that mixed phases can exist in these materials.

4. The metastable monoclinic Eu_2O_3 phase can be reduced by annealing at 800 ^{0}C for 30 minutes without particle growth.

5. A model to predict the particle size at which the defect chemistry will be affected has shown that the defect chemistry is affected when the particle size is approximately 60 nm and smaller. The model also revealed that the dopant distribution changes with concentration but not in the same manner as observed experimentally in the bulk materials.

Chapter 6. Significance of Results and Suggestions for Future Work

6. A. Significance of Results

The use of the Eu^{3+} ion to probe the structures of two nanocrystalline systems revealed interesting structural changes. The particle size dependency results of Eu^{3+}:Y_2O_3 show that systematically reducing the particle size revealed three distinct phases: (1) the sharp lines of monoclinic Y_2O_3 were dominant in the larger nanocrystals; (2) the C_2 site of the cubic phase, which appears in the smaller particles; and (3) the amorphous phase that increases in intensity as the particle size decreases. The observation of distinct spectral lines from the monoclinic phase confirms the presence of a crystalline phase for all of the particle sizes. The discovery of the emerging cubic phase with the reduction in particle size is significant since phase information is related to material properties.

Nanocrystalline Eu^{3+}:CaO has been successfully made by the laser-vaporization-gas-phase condensation method and the materials do fluorescence when excited by the proper wavelength. When prepared with 400 Torr of nitrogen, the broad-band spectrum revealed lines at the same wavelengths reported by Porter and Wright in the bulk material[70].

The formation of the monoclinic Eu_2O_3 phase in some of the nanocrystalline Eu^{3+}:CaO samples is likely due to selective vaporization of the Eu_2O_3 since the melting points of the two oxides differ by more than 10 %.

The site-selective results of the 13-nm samples (prepared with 10 Torr nitrogen), showed that annealing at 800 ^{0}C for 30 minutes results in a 96 % reduction in the monoclinic Eu_2O_3 phase. The TEM results show that the there was not significant

particle growth, which indicates that the nanocrystals are thermally stable under these annealing conditions.

The predicted change in the cubic/orthorhombic ratio of nanocrystalline Eu^{3+}:CaO suggests that the increased surface area plays a significant role in the dopant distribution in nanocrystalline materials. The defect chemistry of nanocrystalline systems has not been extensively studied. The difference in the dopant distribution in the nanocrystalline materials relative to bulk is attributed to lattice distortions that result from the increase in surface area. Scientists have attempted to model the structure of nanocrystals using powder XRD measurements but agree that the information that can obtained is limited with respect to aperiodic parts of the nanocrystal[31]. The preliminary spectroscopic results presented in this thesis indicate aperiodic behavior on the part of the nanocrystals which would render such models inconclusive.

The particle size dependence on the luminescence spectra of two lanthanide-doped materials, Eu^{3+}:Y_2O_3 and Eu^{3+}:CaO, revealed structural details that differ from the bulk. Although nanocrystalline Eu^{3+}:Y_2O_3 has been extensively studied, due to its use as a commercially important phosphor, the phase transformations that were observed as function of the reduced particle size, give new insight into the phase transformations that occur in nanostructured ceramics. Since nanocrystalline Eu^{3+}:CaO has not been reported in the literature, the site-selective spectra and annealing results serve as the first report on the relationship between the optical spectra and structure of this system.

6. B. Suggestions for Future Work

Conceptually, there are two ways that nanostructures can be characterized. One way is to think about the structure in terms of the confinement of electrons due to the reduced

boundary conditions[58]. The other view is to consider the nanostructure as a model system for studying surfaces since a larger percentage of atoms are at the surface. The work presented in the preceding chapters has contributed to both views since the changes in the luminescence spectra, i.e., electron transitions, have been studied. In addition, the effect of the increased surface area on dopant distribution was studied. There is much to be done since the traditional theories that are used for bulk materials do not adequately address the fact that nanocrystals have intrinsic properties that differ from bulk.

An interesting experiment regarding nanocrystalline Eu^{3+}:CaO would be a particle size study similar to the one performed with the Eu^{3+}:Y_2O_3. Since several nanocrystalline systems have been shown to undergo phase changes with reduced particle size, the preparation of nanocrystalline Eu^{3+}:CaO with 1 Torr of nitrogen should produce particles smaller than the 13-nm samples that were studied. The resulting nanocrystals could be studied by site-selective laser spectroscopy to gain insight into the structural changes that occur at smaller particle diameters.

All of the materials that were prepared for this study were prepared by vaporizing the doped bulk materials. By utilizing a different type of vaporization chamber, one that allows for the simultaneous vaporization of two oxide pellets by two lasers, may allow for nanocrystalline materials to be prepared by the simultaneous vaporization of bulk materials that will eliminate the doping step. These types of materials have been made by various methods and are attractive because the chemically different atoms (molecules) are combined in the interfaces as nearest neighbors irrespective of bulk miscibility [43]. A chamber that will allow simultaneous vaporization of bulk materials has been designed by the author and partially built by a custom vacuum company (Kurt Lesker). The

chamber has been designed so that two CO_2 lasers can vaporize materials simultaneously. Materials prepared with this system may show interesting properties due to the high density of boundaries.

References

(1) Bihari, B.; Eilers, H.; Tissue, B. M. *J. Lumin.* **1997**, *75*, 1.

(2) Li, Z., Hahn, H., Siegel, R.W. *Mater. Lett.* **1988**, *6*, 342.

(3) Smyth, D. M. *The Defect Chemistry of Metal Oxides*; Oxford University Press: New York, 2000.

(4) Tissue, B. *Chem. Mater.* **1998**, *10*, 2837.

(5) Zhang, G., Lui, M.L. *Sensors and Actuators B-Chemical* **2000**, *69*, 144.

(6) VaBen, D.; Stover, D.; de Haart, L. G. J.; Cappadonia, M. *Br. Ceram. Proc.* **1996**, *56*, 35.

(7) Maier, J. *Nature* **2000**, *408*, 946.

(8) Tschope, A.; Sommer, E.; Birringer, R. *Sol. State. Ionics* **2001**, *139*, 255.

(9) Andres, R. P., Averback, R. S., Brown, W. L., Brus, L. E. , Goddard, W. A., Kaldor, A., Louie, S. G., Moscovits, M., Peercy, P. S., Riley, S. J., Siegel, R. W., Spaepen, F., Wang, Y. *J. Mater. Res.* **1989**, *4*, 704.

(10) Bourell, D. L., Kaysser, W. *J. Am. Ceram. Soc.* **1993**, *76*, 705.

(11) Powers, D. E., Guesic, S.G., Pulu, A.C., Hopkins, J.B., Dietz, J.B., Duncan, M.A., Langride-Smith, P.R.R., Smalley, R.E. *J. Phys. Chem* **1982**, *86*, 2556.

(12) Vogt, G. *Proc. Electrochem. Soc.* **1988**, *5*, 572.

(13) Tsuzuki, T., Ding, J., McCormick, P.G. *Physica B* **1997**, *239*, 378.

(14) Carrot, G., Valmalette, J.C., Plummer, C.J.G., Scholz, S.M., Dutta, J., Hofmann, H., Hilborn, J.G. *Colloid Polm Sci* **1998**, *276*, 853.

(15) Shea, L. E., McKittrick, J., Lopez, O. A. *J. Am. Ceram. Soc.* **1996**, *79*, 3257.

(16) Fagherazzi, G.; Polizzi, S. *J. Mater. Res.* **2000**, *15*, 586.

(17) Hahn, H., Averback, R. S. *J. Appl. Phys.* **1990**, *67*, 1113.

(18) Beecroft, L. L.; Ober, C. K. *Chem. Mater.* **1997**, *9*, 1302.

(19) Scandan, G.; Hahn, H.; Parker, J. C. *Scripta Metallurgica et Materialia* **1991**, *25*, 2389.

(20) Gunther, B.; Kumpmann, A. *Nanostruct. Mater.* **1992**, *1*, 27.

(21) Eilers, H.; Tissue, B. *Mater. Lett.* **1995**, *24*, 261.

(22) Sordelet, D., Akinc, M. *J. Coll. Interface Sci.* **1988**, *122*, 47.

(23) Hours, T., Bergez, P., Charpin, J., Guizard, C.,. *Ceram. Bull.* **1992**, *71*, 200.

(24) Ravindranathan, P., Komarneni, S., Roy, R. *J. Mater. Sci. Lett.*, *12*, 369.

(25) Venkatachair, K. R., Huang, D., Ostrander, S. P., Schulze, W. A., Stangle, G. C. *J. Mater. Res.* **1994**, *10*, 748.

(26) Capobianco, J. A., Vetrone, F., D'Alesio, T., Speghini, A., Bettinelli, M. *Phys. Chem. Chem. Phys.* **2000**, *2*, 3203.

(27) Martinez-Rubio, M. I., Ireland, T. G., Silver, J., Fern, G., Gibbons, C., Vecht, A. *Electrochem. and Sol. State Lett.* **2000**, *3*, 446.

(28) Kim, M. J., Matijevic, J. *J. Mater. Res.* **1991**, *9*, 436.

(29) Siegel, R. W. *J. Phys. Chem. Solids* **1994**, *55*, 1087.

(30) Ciullity, B. D. *Elements of X-ray Diffraction*; Addison-Wesley: Boston, 1978.

(31) Hamad, K. S., Roth, R., Rockenberger, J., van Vuuren, T., Alivisatos, A. P. *Phys. Rev. Lett.* **1999**, *83*, 3474.

(32) Li, D. X., Ping, D. H., Ye, H. Q., Qin, X. Y., Wu, X. J. *Mater. Lett.* **1993**, *18*, 29.

(33) Tissue, B. M., Bihari, B. *J. Fluores.* **1998**, *8*, 289.

(34) Park, N. G., Schlichthorl. G., van de Lagemaat, J., Cheomg, H. M., Mascarenhas, A., Frank, A. J. *J. Phys. Chem. B* **1999**, *1999*, 3308.

(35) Bowen Katari, J. E., Colvin, V. L., Alivisatos, A. P. *J. Phys. Chem.* **1994**, *98*, 4109.

(36) Siegel, R. W., Ramasamy, S., Hahn, H., Li, Z., Lu, T., Gronsky, R. *J. Mater. Res.* **1988**, *3*, 1367.

(37) Wu, Z. Y., Zhang, K., Ibrahim, D. C., Xian, Li, G., Tao, Y., Hu, T. D., Bellucci, S., Marcelli, A., Zhang, Q. H., Gao, L., Chen, Z. Z. *Appl. Phys. Lett.* **2002**, *80*, 2973.

(38) Li, H. D., Zhang, S. L., Yang, H. B., Zou, G. T., Yang, Y. Y., Yue, K. T. , Wu, X. H. , Yan, Y. *J. Appl. Phys.* **2002**, *91*, 4562.

(39) Siegel, R. W. *Mater. Sci. and Eng.* **1993**, *A168*, 189.

(40) Feng Z., Z., J., Huggins, F. E. , Huffman, G. P. *J Catal.* **1993**, *143*, 510.

(41) Brus, L. E.; Siegel, R. W. *J. Mater. Res.* **1989**, *4*, 704.

(42) Wickham, J. N., Herhold, A. B., Alivisatos, A. P. *Phys. Rev. Lett.* **2000**, *84*, 923.

(43) Birringer, R., Gleiter, H. *Advances in Materials Science, Encyclopedia of Mat. Sci. and Eng.*; Pergamon Press: Oxford, 1988.

(44) Goldstein, A. N., Echer, C.M., Alivisatos, A.P. *Science* **1992**, *256*, 1425.

(45) Tolbert, S. H., Alivisatos, A.P. *Ann. Rev. Phys. Chem.* **1995**, *46*, 595.

(46) Karch, J., Birringer, R., Gleiter, H. *Nature* **1987**, *330*, 556.

(47) Muller, E., Oestreich. C., Opoo, U., Michel, G., Rendtel, A. *J. Anal. Chem* **1998**, *361*, 594.

(48) Shang, C., Cammarata, R. C., Weihs, T. P. *J. Mater. Res.* **2000**, *15*, 835.

(49) Gleiter, H. *Prog. Mater. Sci.* **1989**, *33*, 223.

(50) Matijevic, E. *Chemtech* **1991**, 176.

(51) Xu, X. N., Wolfus, Y., Shaulov, A., Yeshurun, Y., Felner, I., Nowik, I., Koltypin, Y., Gedanken, A. *J. Appl. Phys.* **2002**, *91*, 4611.

(52) Sarkas, H. W., Arnold, S.T., Hendricks, J.H., Kidder, L.H., Jones, C.A., Bowen, K.H. *Z. Phys. D* **1993**, *26*, 46.

(53) Labeau, M., Gautheron, B., Cellier, F., Vallet-Regi, M., Garcia, E., Calbet, J.M.,. *J. Sold. State Chem.* **1993**, *102*, 434.

(54) Khaleel, A., Kapoor, P. N., Klabunde, K. J. *Nanostruct. Mater.* **1999**, *11*, 459.

(55) Tuller, H. L. *Sol. State. Ionics* **2000**, *131*, 143.

(56) Puin, W., Rodewald, S., Ramlau, R., Heitjans, P., Maier, J. *Sol. State. Ionics* **2000**, *131*, 159.

(57) Brus, L. E. *J. Chem. Phys.* **1983**, *79*, 5566.

(58) Kruis, F. E., Fissan, H., Peled, A. *J. Aerosol Sci.* **1997**, *29*, 511.

(59) Colvin, V. L., Schlamp, M.C., Alivisatos, A.P. *Nature* **1994**, *370*, 354.

(60) Goldburt, E. T., Kulkarni, B., Bhargava, R.N., Taylor, J., Libera, M. *Mat. Res. Soc. Symp. Proc.* **1997**, *424*, 441.

(61) Bhargava, R. N., Gallagher, D. *Phys. Rev. Lett.* **1994**, *72*, 416.

(62) Bhargava, R. N. *J. Lumin.* **1996**, *70*, 85.

(63) Dieke *Spectra and Energy Levels of Rare Earth Ions in Crystals*; Interscience Publishers: New York, 1969.

(64) Brundage, R. T., Yen, W. M.,. *Phys Rev.B* **1986**, *34*.

(65) Ramponi, A. J., Wright, J. C. *Phys Rev. B* **1987**, *35*, 3965.

(66) Wright, J. C. *Cryst. Latt. Def. Amorph. Mater.* **1985**, *12*, 505.

(67) Cho, K. G., Kumar, D., Lee, D.G., Jones, S.L., Holloway, P.H., Singh, R.K. *Appl. Phys. Lett.* **1997**, *71*, 3335.

(68) Kital, A. H. *Solid State Luminescence*; Chapman-Hall: Cambridge, 1993.

(69) Forest, H.; Ban, G. *J. Electrochem. Soc.* **1969**, *116*, 474.

(70) Porter, L. C., Wright, J.C. *J. Chem. Phys.* **1982**, *77*, 2322.

(71) Hoekstra, H. R. *Inorg. Chem.* **1966**, *5*, 754.

(72) Eyring, L. *Handbook on the Physics and Chemistry of Rare Earths*; North-Holland: Amsterdam, 1979; Vol. 3.

(73) Chen, G., Stump, N.A., Haire, R.G., Peterson, J.R. *J. Alloys Compd.* **1992**, 503.

(74) Hintzen, H. T., van Noort, H.M. *J. Phys. Chem. Solids* **1988**, *49*, 873.

(75) Dexpert-Ghys, J.; Faucher, M.; Caro, P. *Phys. Rev. B* **1981**, *23*, 607.

(76) Scandan, G., Foster, C.M., Frase, H., Ali, M.N., Parker, J.C., Hahn, H. *Nanostruct. Mater.* **1992**, *1*, 313.

(77) Sheng, K. C.; Korenowski, G. M. *J. Phys. Chem.* **1988**, *92*, 50.

(78) Rice, D. K.; DeShazer, L. G. *J. Chem. Phys.* **1970**, *52*, 172.

(79) Vink, A. P., Reijme, M. A., Meijerink, A. *J. Lum.* **2000**, *92*, 189.

(80) Dexpert-Ghys, J.; Charreire, Y.; Leskela, M.; Niinisto, L. *J. Electrochem. Soc* **1985**, *132*, 711.

(81) Eilers, H., Tissue, B. *Mater. Lett.* **1995**, *24*, 261.

(82) Bihari, B., Eilers, H.,Tissue, B. M. *J. Lumin.* **1997**, *75*, 1.

(83) Empedocles, S. A., Neuhauser, R., Shimizu, K., Bawendi, M. G. *Adv. Mater.* **1999**, *11*, 1243.

(84) Shao, Y. Z.; Shek, C. H.; Lai, J. K. L. *J. Mater. Res.* **1998**, *13*, 2969.

(85) Eastman, J. A.; Liao, Y. X.; Siegel, R. W. *Mat. Res. Soc. Symp. Proc.* **1989**, *155*, 255.

(86) Meltzer, R. S., Feofilov, S. P.,Tissue, B.,Yuan, H.B. *Phys. Rev. B* **1999**, *60*, R14 012.

(87) Granqvist, D. G.; Buhrman, R. A. *J. Applied Phys.* **1975**, *47*, 2200.

(88) Zhao, J.; Huggins, F. E.; Z., F.; Lu, F.; Shah, N.; Huffman, G. P. *J Catal.* **1993**, *143*, 499.

(89) Maier, J. *Angewandte Chemie* **1993**, *32*, 313.

(90) Phillips, R. *Crystals, Defects, and Microstructures: Modeling Across Scales*; Cambridge University Press: Cambridge, 2001.

(91) Gosele, U. M., Tan, T.Y. *MRS Bulletin* **1991**, 42.

(92) Stoneham, A. M. *MRS Bulletin* **1991**, 22.

(93) Nowick, A. S. *MRS Bulletin* **1991**, 38.

(94) McGeehin, P., Henderson, B. *J. Phys.* **1974**, *7*, 3988.

(95) Tallant, D. R.; Wright, J. C. *J. Chem. Phys.* **1975**, *63*, 2074.

(96) Long, G. L., Personal Communication.

(97) Kenner, C. T., Busch, K. W. *Quantitative Analysis*, First ed.; Macmillian Publishing Co.: New York, 1979.

(98) Linke, W. F. *Solubilities*, Fourth ed.; D. Van Nostrand, Inc.: Princeton, 1958.

(99) Williams, D. K.; Bihari, b.; Tissue, B. M. *J. Phys. Chem.* **1998**, *92*, 916.

(100) Cho, S. H., Yoo, J. S., Lee, J. D. *J. Electrochem. Soc* **1998**, *145*, 1017.

(101) Jiang, Y. D., Wang, Z. L. *J. Mater. Res.* **1998**, *13*, 2950.

(102) Ye, T., Guiwen, Z., Weiping, Z., Shangda, X. *Mat. Res. Bulletin* **1997**, *32*, 501.

(103) Averback, R. S.; Hahn, H.; Hofler, H. J.; Logas, J. L.; Shen, T. C. *Mat. Res. Soc. Symp. Proc.* **1989**, *153*, 3.

(104) Bhargava, R. N.; Chhabra, V.; Kulkarni, B.; Veliadis, J. V. *Phys. Sol. Stat. B* **1998**, *210*, 621.

(105) Henrich, V. E., Cox, P. A. *The Surface Science of Metal Oxides*; Cambridge University Press: Cambridge, 1994.

(106) Di Cosimo, J. I., Diez, V. K., Xu, M., Iglesia, E., Apesteguia, C. R. *J Catal.* **1998**, *178*, 499.

(107) Rodriguez, J. A., Jirsak, T., Gonzalez, L., Evans, J., Perez, M., Maiti, A. *J. Chem. Phys.* **2001**, *115*, 10914.

(108) Aguado, A. *Phys. Stat. Sol. B* **2002**, *229*, 1335.

(109) Smyth, D. M. *Sol. State. Ionics* **2000**, *129*, 5.

(110) Suyver, J. F., Meester, R., Kelly, J. J., Meijerink, A. *Phys Rev. B.* **2001**, *64*, 235408.

Curriculum Vita

Undergraduate Education 1992-1995

Hollins College, Roanoke, VA 24020
B. A. double major in Chemistry and Art History, *with honors*, 1995

Honors and Awards

Graduate Teaching Award for Teaching Excellence (two-time recipient), Dept. of Chemistry, Virginia Tech
Honors in Chemistry, Hollins College
James Lewis Howe Award in Chemistry, Hollins College
Margaret Markley Smith Award in Art, Hollins College
ACS Award in Organic Chemistry, Hollins College
Pinnacle National Honors Society, Hollins College
Honors Thesis, Hollins College; Research Advisors: Professor Daniel R. Derringer and Professor William L. Whitwell

Presentations

National American Chemical Society (ACS) Meeting; Dallas, Texas
Regional ACS Meetings; Roanoke, Virginia and Research Triangle Park, North Carolina
Graduate Research Seminar; Department of Chemistry, Virginia Tech.
Undergraduate Research Symposium; Department of Chemistry,Virginia Tech.
Undergraduate Research Seminar; Hollins University.
Honors Research Seminar; Hollins University.

Publications

Williams, D.K., Bihari, B., Tissue, B.M., Preparation and Fluorescence Spectroscopy of Bulk Monoclinic Eu^{3+}:Y_2O_3 and Comparison to Eu^{3+}:Y_2O_3 Nanocrystals, *J. Phys. Chem. B*, 1998, 102, 916-920.

Hong, K.S., Meltzer, R.S., Bihari, B., Williams, D.K., Tissue, B.M., Spectral hole-burning in crystalline Eu^{3+}:Y_2O_3 and Eu^{3+}:Y_2O_3 nanoparticles, *J. Lumin*. 76-77, 234-237, Feb 1998

Williams, D.K., Yuan H., Tissue, B.M., Size dependence of the luminescence spectra and dynamics of Eu^{3+}:Y_2O_3 nanocrystals, *J. Lumin.* 83-84 (1999) 297-300.

Yang H.S., Feofilov, S.P., Williams, D.K., Bihari, B., Tissue, B.M., One phonon relaxation processes in Eu^{3+}:Y_2O_3 nanocrystals, *Physica B* 263: 476-478 March 1999